A unique radiometric measurement station design incorporating spectral and image data collection

by

Menelaos Meli

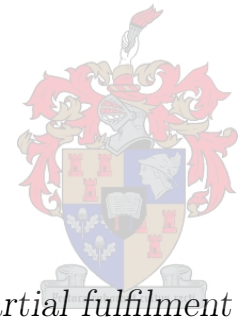

Thesis presented in partial fulfilment of the requirements for the degree of Master of Engineering (E&E) in the Faculty of Engineering at Stellenbosch University

Supervisor: Dr. Arnold J. Rix
Co-supervisor: Dr. Johannes M. Strauss

April 2022

Declaration

By submitting this thesis electronically, I declare that the entirety of the work contained therein is my own, original work, that I am the sole author thereof (save to the extent explicitly otherwise stated), that reproduction and publication thereof by Stellenbosch University will not infringe any third party rights and that I have not previously in its entirety or in part submitted it for obtaining any qualification.

Date: ..... April 2022 .....

Abstract

A unique radiometric measurement station design incorporating spectral and image data collection

M. Meli

Department of Electrical and Electronic Engineering,
University of Stellenbosch,
Private Bag X1, Matieland 7602, South Africa.

Thesis: MEng (E&E)

April 2022

The performance of photovoltaic (PV) panels is determined under standard test conditions (STC). However, in practical PV installations, it is rare for PV panels to operate under the STC at which they are rated. The variation in spectral irradiance under different atmospheric conditions significantly impacts the performance of PV panels. The output of a PV power plant is also significantly affected as a large cloud bank travels across the sky above. The passing clouds attenuate the received solar spectral irradiance and reduce the output power. Sudden changes in output power of a grid connected plant, as a result of clouds, may lead to voltage and frequency oscillations and result in system instability. Accurate short-term irradiance prediction models are important tools used to manage these power fluctuations. However, many irradiance prediction models and software tools used in the PV industry do not take these spectral impacts on PV performance into account. There is a lack of measurement stations dedicated to collecting the data necessary to improve these prediction models and software tools.

A unique radiometric measurement station is designed and built in this thesis for the collection of data required by researchers to improve upon irradiance forecasting models and PV software tools. The instruments on the measurement station include: a pyranometer, a pyrheliometer, a wide field-of-view (FOV) spectral irradiance meter, a narrow FOV spectral irradiance meter and a digital camera. The instruments are mounted on a pan/tilt unit that is able to accurately track the position of the sun in the sky throughout the day for solar elevation angles greater than 10°. The data collected by the station includes temperature, humidity, air pressure, broadband irradiance and spectral irradiance. Images of the sky correlating to the various irradiance measurements are captured by the onboard digital camera. The measurement station is designed to be solar powered, compact and weather-resistant, allowing it to be deployed in remote locations for data collection.

The station is configured to capture a measurement set of data once every 10 minutes in 4 distinct measurement positions: facing directly towards the sun, facing north with

optimal tilt, facing north with a fixed 30° tilt, and facing north with a 0° tilt. The measurement frequency and measurement positions can be configured by the user as necessary.

The broadband irradiance measurements are validated by comparison to data collected by an independent measurement station nearby. The correlation between the spectral irradiance measurements and the AM1.5 reference spectrum is shown, as well as the variation of the solar spectrum during different seasons, different times of day and different cloud conditions.

The measurement station is found to fulfil all requirements and successfully collects the data required to improve irradiance prediction models and PV software tools. This station has the potential to help optimize PV power stations as well as domestic PV installations.

Uittreksel

'n Unieke radiometriese meetstasie ontwerp wat spektrale en beelddata-insameling inkorporeer

("A unique radiometric measurement station design incorporating spectral and image data collection")

M. Meli

Departement Elektriese en Elektroniese Ingenieurswese,
Universiteit van Stellenbosch,
Privaatsak X1, Matieland 7602, Suid Afrika.

Tesis: MIng (E&E)

April 2022

Die werkverrigting van fotovoltaïese (FV) panele word by standaard toets toestande bepaal. In praktiese toepassings is dit selde dat daar aan standaard toets toestande voldoen word. Die variasie in spektrale bestraling onder verskillende atmosferiese toestande beïnvloed die werkverrigting van FV-panele aansienlik. Die uitset van 'n FV-kragstasie word aansienlik geaffekteer soos groot wolkbanke deur die lug beweeg. Die verbygaande wolke verswak die sonbestraling wat ontvang word en verminder die totale FV uittree drywing. Skielike veranderinge in uittree drywing as gevolg van wolke kan lei tot spanning en frekwensie ossillasies, wat lei tot stelsel onstabiliteit. Akkurate korttermyn bestraling voorspellingsmodelle is belangrike gereedskap wat gebruik word om hierdie krag fluktuasies te bestuur. Baie bestraling voorspellingsmodelle en sagteware wat in die FV-industrie gebruik word, neem egter nie hierdie spektrale impakte op FV-prestasie in ag nie. Daar is 'n tekort aan meetstasies wat toegewy is om die data in te samel wat nodig is om hierdie voorspellings modelle en sagteware te verbeter.

'n Unieke radiometriese meetstasie is in hierdie tesis ontwerp en gebou. Die meetstasie is verantwoordelik vir die insameling van data wat deur navorsers benodig word om die huidige bestraling voorspellingsmodelle en FV sagteware te verbeter. Die instrumente op die meetstasie sluit in 'n pyranometer, 'n pirheliometer, 'n wye gesigsveld spektrale bestralingsmeter, 'n nou gesigsveld spektrale bestralingsmeter en 'n digitale kamera. Die instrumente is op 'n sonvolgeenheid gemonteer wat die posisie van die son regdeur die dag akkuraat kan volg vir sonhoogte hoeke groter as 10 grade. Die data wat die meetstasie insamel sluit temperatuur, humiditeit, lugdruk, breëband bestraling en spektrale bestraling in. Beelde van die lug wat verband hou met die verskillende bestralingsmetings word deur die digitale kamera aan boord gestoor. Die meetstasie is ontwerp om sonkrag-aangedrewe, kompak en weerbestand te wees, sodat dit in afgeleë plekke vir data-insameling ontplooi kan word.

Die meetstasie is opgestel om een keer elke 10 minute data op te neem in 4 verkillende metingsposisies. Dit sluit in 'n meting wat direk na die son kyk, 'n meting wat noord kyk met optimale kanteling, 'n meting wat noord kyk met 'n vaste 30 grade kantel, en 'n meeting wat noord kyk met 'n 0 grade kantel. Die metingsfrekwensie en metingsposisies kan deur die gebruiker verander word soos nodig.

Die breëband-bestralingsmetings word geverifieer deur dit te vergelyk met data wat deur 'n nabye onafhanklike meetstasie ingesamel is. Die korrelasie tussen die spektrale bestralingsmetings en die AM1.5-verwysingspektrum word getoon, sowel as die variasie van die sonspektrum gedurende verskillende seisoene, verskillende tye van die dag, en verskillende wolktoestande.

Daar word gevind dat die meetstasie aan alle vereistes voldoen. Die nodige data om die bestraling voorspellings modelle en FV-sagteware te verbeter word suksesvol versamel deur die gebruik van die meetstasie. Hierdie stasie het die potensiaal om FV-kragstasies sowel as huishoudelike FV-installasies te help optimeer.

Acknowledgements

I would like to express my sincere gratitude to the following people:

- My supervisor Dr. A.J. Rix, and my co-supervisor Dr. J.M. Strauss, for providing me with the opportunity to complete this project. Thank you for all the guidance and support throughout the duration of the project.
- Mr. P.H. Petzer, Mr. A. Swart and Mr. H. Koopman, for their assistance with the fabrication and assembly of the measurement station. Thank you for the many hours of work that was put into this project.
- Mr. M. Lecholo, for his assistance with 3D printing, and Ms. J. Martin, for her assistance in ordering the required components.
- My friends and colleagues at the engineering faculty, for their support and for sharing their knowledge with me.
- My parents, for their support and encouragement.

Contents

Declaration i

Abstract ii

Uittreksel iv

Acknowledgements vi

Contents vii

List of Figures ix

List of Tables xii

Nomenclature xiii

1 Introduction 1
- 1.1 Background . . . 1
- 1.2 Problem Statement . . . 2
- 1.3 Overview of Thesis . . . 3

2 Literature Review 5
- 2.1 Introduction . . . 5
- 2.2 Solar Position . . . 5
- 2.3 Solar Radiation . . . 10
- 2.4 Measurement Devices . . . 15
- 2.5 Irradiance Prediction . . . 18
- 2.6 PV Modules . . . 20
- 2.7 Chapter Review . . . 23

3 Device Selection and System Design 24
- 3.1 Introduction . . . 24
- 3.2 System Design Objectives . . . 24
- 3.3 Device Selection and Description . . . 25
- 3.4 Power Supply . . . 34
- 3.5 Hardware Integration . . . 39
- 3.6 Measurement Station Design . . . 41
- 3.7 Torque Balancing . . . 44
- 3.8 Chapter Review . . . 47

4 Software **48**
4.1 Introduction . . . 48
4.2 Modbus Protocol . . . 49
4.3 Pelco-D Protocol . . . 53
4.4 RS-485 ASCII Protocol . . . 56
4.5 Camera . . . 60
4.6 Solar Tracking . . . 64
4.7 Measurement Sequence . . . 67
4.8 Chapter Review . . . 67

5 Station Set Up and Data Collection **69**
5.1 Introduction . . . 69
5.2 Test Site . . . 69
5.3 Set-Up of Measurement Station . . . 70
5.4 Data Collection . . . 76
5.5 Chapter Review . . . 79

6 Station Evaluation and Data Analysis **80**
6.1 Introduction . . . 80
6.2 Evaluation of Measurement Station . . . 80
6.3 Data Analysis . . . 87
6.4 Chapter Review . . . 100

7 Conclusion and Recommendations **102**
7.1 Conclusion . . . 102
7.2 Problems and Recommendations . . . 103

Appendices **104**

A Power Supply **105**
A.1 5 V Supply . . . 105
A.2 12 V Supply . . . 108

B Technical Drawings **111**

List of References **118**

List of Figures

1.1 Increase in PV installed capacity as outlined in the IRP2019. 2

2.1 The tilt angle of the rotational axis of the earth and its movement along the ecliptic plane. 6
2.2 Solar declination angle through the year. 7
2.3 Solar azimuth and altitude angles are used to describe the position of the sun in the sky. 9
2.4 Spectral irradiance of an ideal 5800 K blackbody. 11
2.5 Spectral irradiance of an ideal 5800 K blackbody compared with the AM0 solar spectrum. 11
2.6 Air mass ratio is the ratio of h_2 to h_1. The air mass ratio is 1 when the sun directly overhead. 12
2.7 Spectral irradiance shown at AM0, AM1.5 Global and AM1.5 Direct under the ASTM G-173-03 standard. 13
2.8 Direct, diffuse and reflected components of solar radiation striking a collector. 14
2.9 Construction of a Pyrheliometer. 15
2.10 Construction of a Pyranometer. 16
2.11 Czerny-Turner Spectrometer. 17
2.12 Illustration of the photovoltaic effect. 21
2.13 Energy bands for semiconductors. 22

3.1 High-Level System Diagram. 26
3.2 Kipp & Zonen SHP1 Pyrheliometer. 27
3.3 Kipp & Zonen SMP10 Pyrheliometer. 27
3.4 Spectrafy SolarSIM-D2 Spectral Irradiance Meter. 28
3.5 Spectrafy SolarSIM-G Spectral Irradiance Meter. 28
3.6 Spectrafy Combox. 29
3.7 Sony RX0 Digital Camera. 30
3.8 Servo Motor and Linear Actuator. 30
3.9 Pan/Tilt Unit. 31
3.10 Raspberry Pi Model 3B. 32
3.11 DS1302 RTC. 32
3.12 D-Link Router. 33
3.13 Microcare MPPT. 37
3.14 Electrical Enclosure. 38
3.15 Suggested LT8610 circuit layout as per datasheet 38
3.16 Suggested LTC3115 circuit layout as per datasheet 39
3.17 Device Integration - Communication. 40
3.18 Device Integration - Power Connections. 41

3.19 Enclosure Assembly. 42
3.20 Enclosure Design. 42
3.21 Servo Motor and Camera Mounting Bracket. 43
3.22 Assembly of Mounting Bracket. 44
3.23 Measurement Station Force Diagram. 44
3.24 Torque as a function of Tilt Angle. 45
3.25 Torque Curve at Different Spring Stiffness. 46
3.26 Spring used to create counter-torque. 47

4.1 Modbus Message Frame 49
4.2 Calculation of CRC16. 50
4.3 Kipp & Zonen Data Request. 52
4.4 Format of .csv file. 53
4.5 Pelco-D Command Message Frame. 54
4.6 Pelco-D Angle Query Response Format. 55
4.7 Pan/Tilt Unit Operation. 55
4.8 Spectrafy Data Request. 58
4.9 SolarSIM-D2 .csv file. 59
4.10 SolarSIM-G .csv file. 59
4.11 Servo control using PWM. 61
4.12 Capture Image Function. 62
4.13 Power Camera On. 63
4.14 Toggle Servo. 63
4.15 Solar Position Overview. 65
4.16 Positional Calibration. 66
4.17 Measurement Sequence. 67

5.1 Sun Path Above Test Site. 69
5.2 Obstruction of Sun by Buildings. 70
5.3 Measurement Station Overview. 71
5.4 Power and Communications Pass-through on Pan/Tilt Unit. 71
5.5 Implementation of 20° Wedge and Spring Apparatus on Station. 72
5.6 Instruments on Measurement Station. 73
5.7 Leveled Domes of Kipp & Zonen SMP10 and Spectrafy SolarSIM-G. 74
5.8 Camera and Servo Motor Mounted Inside Enclosure. 74
5.9 Device Connections. 75
5.10 Connections inside of IP65 Electrical Enclosure. 76
5.11 Currently Configured Measurement Positions. 77
5.12 Potential Future Measurement Configuration. 78

6.1 Comparison of Measured DNI with SAURAN DNI. 81
6.2 Comparison of Measured GHI with SAURAN GHI. 81
6.3 Evaluation of Positional Calibration Sequence. 82
6.4 Measured Direct Circumsolar Spectrum Compared to ASTM-G-173-03 AM1.5 Direct Spectrum. 83
6.5 Measured Gloabal Tilted Spectrum Compared to ASTM-G-173-03 AM1.5 Global Tilted Spectrum. 84
6.6 Measured DNI as Sun Moves Across Pyrheliometer FOV. 85
6.7 Sun Moving Across Pyrheliometer Field of View. 85

6.8 Merged Images of Sun at Maximum DNI Readings. 86
6.9 Dew on Camera Lens on a Cold Morning. 86
6.10 Global Irradiance in Different Measurement Positions. 87
6.11 Movement of Clouds Past the Sun Causing Dip in Irradiance 88
6.12 Direct Circumsolar Spectral Irradiance at Different Times. 89
6.13 Global Tilted Spectral Irradiance at Different Times. 89
6.14 Direct Spectral Irradiance in Different Seasons. 90
6.15 Normalised Direct Spectral Irradiance in Different Seasons. 91
6.16 Global Spectral Irradiance in Different Seasons. 91
6.17 Normalised Global Spectral Irradiance in Different Seasons. 92
6.18 Percent Decrease in Spectral Irradiance from Summer to Winter. 92
6.19 Percent Decrease in Normalised Spectral Irradiance from Summer to Winter. 93
6.20 Image of Sun in the Sky in Different Seasons. 93
6.21 Movement of Clouds Past the Sun. 94
6.22 Direct Spectral Irradiance under Clear and Cloudy Conditions. 94
6.23 Normalised Direct Spectral Irradiance under Clear and Cloudy Conditions. . 95
6.24 Global Tilted Spectral Irradiance under Clear and Cloudy Conditions. 95
6.25 Normalised Global Spectral Irradiance under Clear and Cloudy Conditions. . 96
6.26 Percent Decrease in Spectral Irradiance Caused by Moving Clouds. 96
6.27 Percent Decrease in Normalised Spectral Irradiance Caused by Moving Clouds. 97
6.28 Images of Sky on Clear and Overcast Days 98
6.29 Global Tilted Spectrum on Clear and on Overcast Days. 98
6.30 Normalised Global Tilted Spectrum on Clear and on Overcast Days. 99
6.31 Percent Decrease in Spectral Irradiance from Clear to Overcast Conditions. . 99
6.32 Percent Decrease in Normalised Spectral Irradiance from Clear to Overcast Conditions. 100

A.1 PCB Layout of 5 V Supply. 106
A.2 PCB Layout of 12 V Supply. 109

List of Tables

3.1 Functions of Devices. . . . 33
3.2 Device Overview 34
3.3 Power Requirements per Device. . . . 34
3.4 Requirements as per Supply Voltage. . . . 34
3.5 Average Power and Energy Requirements During the Day. . . . 35
3.6 Average Power and Energy Requirements During the Night. . . . 36
3.7 Enclosure Overview. . . . 43

4.1 Modbus Commands 50
4.2 Kipp & Zonen Communication Configuration. . . . 50
4.3 Modbus Request - Sent Bytes. . . . 51
4.4 Kipp & Zonen Input Registers. . . . 51
4.5 Description of Received Bytes. . . . 51
4.6 Description of Data in Registers. . . . 52
4.7 Notable Pelco-D Command Bytes. . . . 54
4.8 Pan/Tilt Unit Communication Configuration. . . . 55
4.9 Spectrafy Communication Configuration. . . . 58
4.10 Specified pulse duration and corresponding servo angles. . . . 60
4.11 Parameters for PWM setup. . . . 63

5.1 Details of Measured Parameters. . . . 78
5.2 Details for SSH. . . . 79

6.1 Atmospheric Conditions. . . . 88
6.2 Atmospheric Conditions. . . . 90

A.1 Component Values Used. . . . 105
A.2 Component Values Used. . . . 108

Nomenclature

Constants

c = 3×10^{8} m/s
h = 6.63×10^{-34} W/s^2
k = 1.38×10^{-23} J/K
SC = 1370 W/m^2
σ = 5.67×10^{-8} W/m^2/K^4

Abbreviations

AM Air Mass
ANN Artificial Neural Network
API Application Programming Interface
ASCII American Standard Code of Information Interchange
ASHRAE American Society of Heating, Refrigeration and Air-Conditioning Engineers
ASTM American Society for Testing and Materials
CAD Computer-Aided Design
CCTV Closed-Circuit Television
CdTe Cadmium Telluride
CIGS Copper Indium Gallium Diselenide
CRC Cyclic Redundancy Check
CSP Concentrated Solar Power
CSV Comma-Separated Values
CT Civil Time / Clock Time
DC Direct Current
DNI Direct Normal Irradiance
FOV Field of View
GHI Global Horizontal Irradiance
GPIO General-Purpose Input/Output
HDPE High Density Polyethylene
LSB Least Significant Byte
MAPE Mean Absolute Percentage Error
ML Machine Learning
MPPT Maximum Power Point Tracker

MSB Most Significant Byte
MTBF Mean Time Between Failure
NWP Numerical Weather Prediction
PCB Printed Circuit Board
PTZ Pan Tilt Zoom
PV Photovoltaic
PWM Pulse Width Modulation
RTC Real Time Clock
SMA Sub-Miniature Version A
SPI Serial Peripheral Interface
SSH Secure Shell
ST Solar Time
STC Standard Test Conditions
SVM Support Vector Machine
TSI Total Sky Imager
UART Universal Asynchronous Receiver/Transmitter
USB Universal Serial Bus
WSI Whole Sky Imager

Variables

E_g	Band Gap Energy	[eV]
E_λ	Photon Energy	[eV]
H	Hour Angle	[°]
L	Latitude Angle	[°]
β	Solar Altitude Angle	[°]
δ	Solar Declination Angle	[°]
ϕ_S	Solar Azimuth Angle	[°]
λ	Wavelength	[nm]

Chapter 1

Introduction

1.1 Background

Many nations are adopting renewable energy sources at increasing rates in an attempt to combat climate change. The Paris Agreement is a legally binding treaty that requires all 196 signatory countries to take steps to reduce their carbon emissions. The agreement aims to achieve a carbon neutral world by the year 2050. [1]

Currently, most power plants generate electricity using fossil fuels such as coal and natural gas as sources of energy. These energy sources are neither clean nor sustainable. Using coal as an energy source emits 0.6 kg - 1.6 kg of carbon dioxide equivalent per kilowatt hour (CO_2e/kWh), while natural gas is slightly cleaner at 0.27 kg - 0.9 kg CO_2e/kWh. In contrast, renewable energy sources such as solar photovoltaics (PV) release 0.03 kg - 0.09 kg CO_2e/kWh over their lifetime. Solar energy is both clean and sustainable and is, therefore, useful in the attempt to reach global carbon neutrality. [2]

South Africa is one of the 196 signatories of the Paris Agreement, and has committed to reducing its carbon emissions. Solar energy is ideal for electricity generation in South Africa, as an average of more than 2500 hours of sunshine is received annually with a 24-hour average solar irradiance of 220 W/m^2 [3]. The South African Department of Mineral Resources and Energy has pledged to increase PV installed capacity by 814 MW by the end of 2022 and intends on adding a further 5670 MW by 2030 [4]. The planned increases in PV installed capacity, as outlined in the Integrated Resource Plan (IRP2019) by the South African Department of Mineral Resources and Energy, is shown in Figure 1.1.

Despite all the advantages to using solar PV energy, there are drawbacks. Solar energy is intermittent, and the output of PV power plants is not as stable as the output of traditional coal-fired plants. Environmental factors, such as changes in weather conditions and changes in cloud cover, are responsible for variations in PV plant output. The accurate prediction of the variation in PV plant output caused by environmental factors is an important tool used to manage and reduce the effects of sudden power fluctuations on the grid.

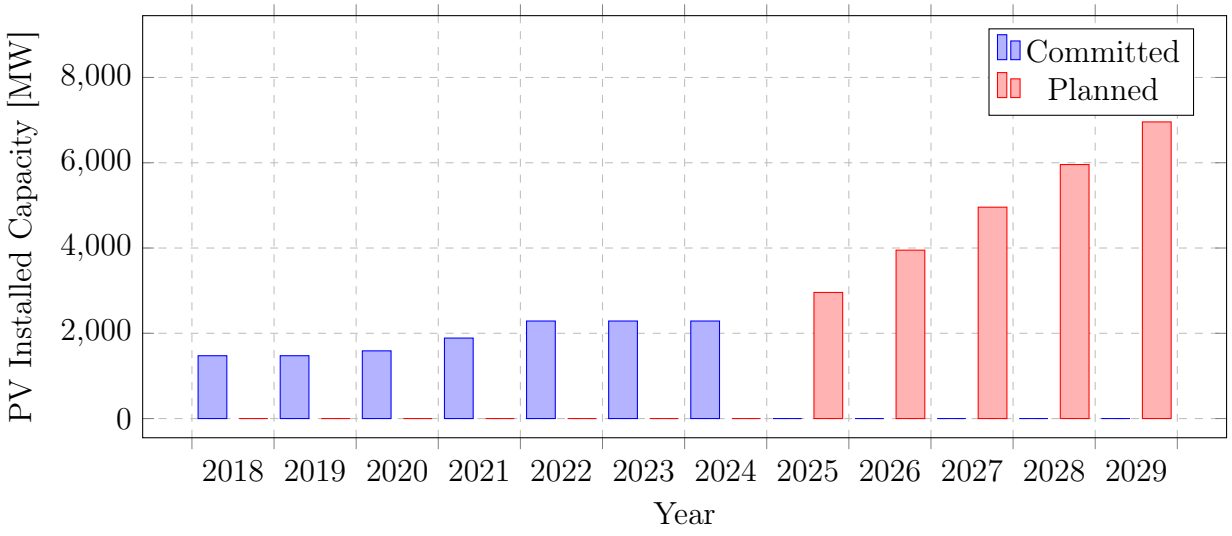

Figure 1.1: Increase in PV installed capacity as outlined in the IRP2019.

1.2 Problem Statement

The performance of PV panels is determined under IEC 60904-3 standard test conditions (STC). These conditions define the irradiance, the spectral distribution and the temperature at which the panels are evaluated. In practical applications, STCs are rarely met, as the solar spectrum varies under different atmospheric conditions. These spectral variations may impact PV performance noticeably, especially in areas where the spectrum is significantly different from the reference spectrum. Some PV technologies are more sensitive to spectral changes than others. Therefore, it is important to consider how the spectrum affects PV module output when selecting panels in order to maximise efficiency. However, many software tools used in the PV industry do not take these spectral impacts into account, especially the spectral effects caused by precipitable water vapor and air mass. [5]

The output of PV power plants is also severely reduced as large cloud banks sweep across the area [6]. These sudden changes in output may cause voltage and frequency oscillations and system instability [7]. If this decrease in PV plant output coincides with a spike in load demand, a power outage could occur. Energy storage systems can be implemented to minimise the effects of these fluctuations, however, this is costly [7]. Alternatively, short-term irradiance prediction methods can be implemented to smoothly ramp down the output of the PV plant while allowing alternative power sources, such as diesel generators, to be connected to the grid.

There is a need to develop a system to collect the data required by researchers to improve upon PV software tools and irradiance prediction models. The system could gather spectral data to improve PV software tools to make more accurate yield forecasts. This would also allow for PV panels that are optimized for the spectrum at a specific location to be selected for use. Visual data and spectral data that is collected could be used to train machine learning algorithms to achieve accurate short-term irradiance predictions using low cost equipment. Such a system has the potential to help optimize PV power stations as well as domestic PV installations.

1.2.1 Aims

This thesis aims to develop a measurement station which collects data that can be used to improve upon irradiance prediction models and PV software tools.

The station must achieve the following to be considered a success:

- Collect new data that is currently not used in irradiance forecasting models, as well as data that is currently used
- Perform tasks and measurements automatically
- Have the ability to operate in isolated areas
- Be portable

1.2.2 Objectives

The following objectives are set in order to develop the required system:

- Investigate existing irradiance forecasting methods
- Determine the types data used in the forecasting models
- Investigate existing data collection methods
- Investigate the factors affecting the efficiency of PV
- Design and build a system capable of capturing and logging the required data
- Analyse captured data to evaluate the performance of the system and validate its operation

The improvement/development of irradiance forecasting models and PV software tools is beyond the scope of this thesis.

1.3 Overview of Thesis

This thesis has the following structure:

- **Chapter 2:** This chapter begins by investigating the movement of the sun in the sky throughout the day. This is important as accurate solar tracking is essential for the system designed in this thesis. The solar spectrum is then discussed and the concept of air mass is introduced. Different irradiance prediction methods are investigated along with the data they depend on. Existing data collection methods are then identified. The operation of PV modules is discussed and the factors that influence their efficiency are investigated to determine what additional data must be collected.

- **Chapter 3:** This chapter discusses the design of the system. The chapter begins by presenting the system design objectives. The devices used in the system are described and their selection is motivated. The power and energy requirements for the system are determined. The planned device integration is shown. The enclosure design and assembly is presented.

- **Chapter 4:** This chapter discusses the software design of the system. An overview of the used communication protocols is provided and the software used to communicate with each device is discussed. The software used to track the position of the sun and to operate the system as a whole is explained. Flow diagrams and function descriptions are provided.

- **Chapter 5:** This chapter discusses system set up and data collection. The test site is described and the set up of the entire system is described in detail. Considerations made in the actual assembly of the system are noted. The data collection configuration is discussed.

- **Chapter 6:** This chapter presents and analyses the collected data to evaluate the performance of different aspects of the system. The solar spectrum is analysed under different conditions to determine how it changes.

- **Chapter 7:** This chapter summarises the results obtained in this thesis. Conclusions regarding the designed system are drawn and recommendations are made for future improvements.

Chapter 2

Literature Review

2.1 Introduction

This chapter provides an insight into the most important concepts needed for this thesis. The movement of the earth relative to the sun must be investigated, as tracking the position of the sun in the sky is essential for this project. The solar spectrum and the effects of air mass on the spectrum must also be explored, as the collection of spectral data is a key component of the designed system. Existing irradiance forecasting methods must be researched to determine what data is required for prediction models, and the instruments and methods currently used to collect the data must be identified. Finally, the factors affecting the output power and efficiency of PV modules must be investigated to determine what additional data is important to collect so that the output of PV panels can be more accurately predicted.

2.2 Solar Position

Having a thorough understanding of how the sun moves across the sky is essential in order to design and build the measurement station. The measurement station must be able to accurately predict the position of the sun in the sky in order to take accurate and relevant measurements. The angles used in the expressions that follow are measured in degrees except where otherwise specified.

2.2.1 The Orbit of the Earth

The earth periodically orbits the sun along an elliptical path once every 365.25 days. The earth reaches a point closest to the sun on January 2^{nd} at a distance of approximately 147 million kilometers. This point is called the perihelion. The aphelion is the point at which the earth is furthest from the sun at a distance approximately 152 million kilometers. The aphelion occurs on July 3^{rd}. [8]

The distance between the sun and the earth is described by equation (2.1) as presented by Masters [8, p.190].

$$d = 1.5 \times 10^8 \left\{ 1 + 0.017 \sin \left[\frac{360(n-93)}{365} \right] \right\} \quad km \tag{2.1}$$

In equation (2.1), d represents the distance between the earth and the sun in kilometers and n represents the day number with January 1^{st} being day 1 and December 31^{st} being day 365.

The characteristics of the movement of the earth around the sun are assumed to be constant for most solar energy applications, since its orbit has only small variations [9]. However, its orbit changes from elliptical to almost circular with a period of 100 000 years, the tilt angle changes from 21.5° to 24.5° with a period of 41 000 years and the precession of its rotational axis has a period of 23 000 years [8].

2.2.2 Solar Declination

The polar axis of the earth is tilted at an angle of 23.45° to the ecliptic plane [9], as shown in Figure 2.1. This tilt is responsible for the sun appearing to be higher in the sky during the summer and lower during the winter. In the Southern Hemisphere, the sun is directly above the Tropic of Capricorn on the first day of summer and it is directly above the Tropic of Cancer on the first day of winter. The sun lies directly above the equator on the first days of both spring and autumn [9].

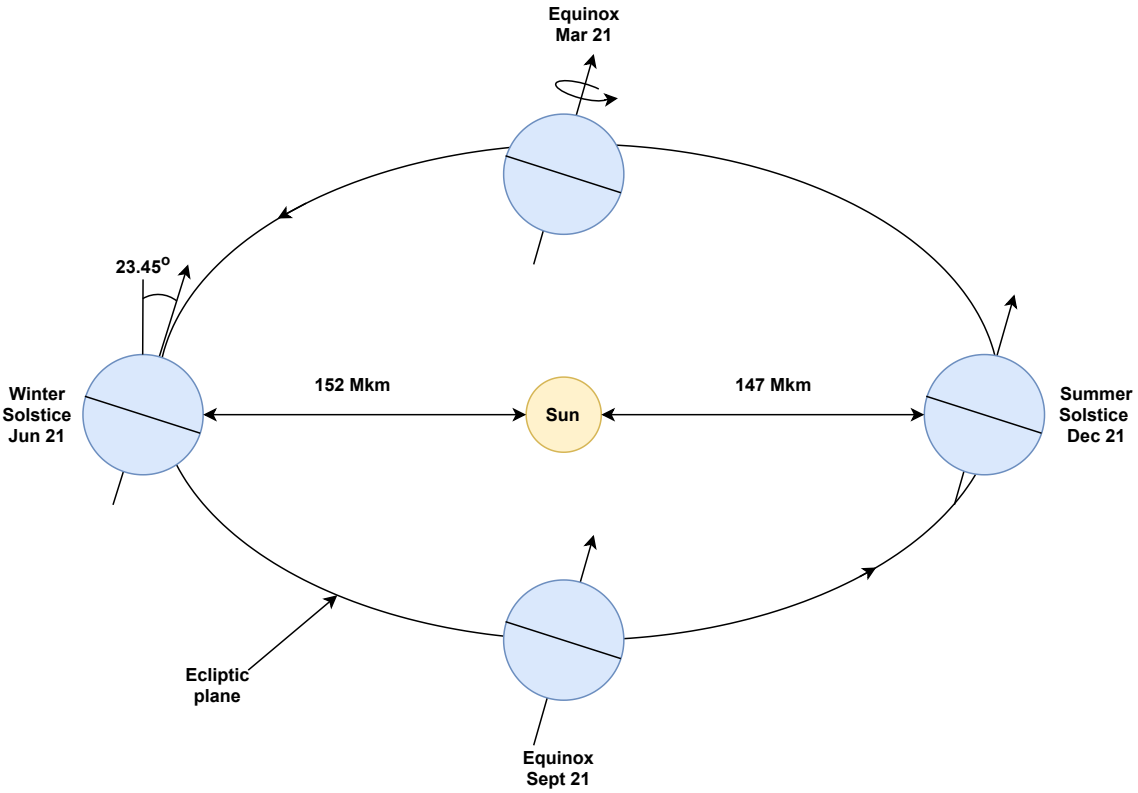

Figure 2.1: The tilt angle of the rotational axis of the earth and its movement along the ecliptic plane. *Source:* Redrawn Figure as shown in [8, p.192].

The angle formed between the centre of the sun and the equator is called the solar declination angle, denoted δ. The solar declination angle varies between $\pm 23.45°$ throughout the year, and can be approximated using equation (2.2) as presented by Masters [8, p.194]. The convention for equation (2.2) is that angles are positive in the North and negative in the South.

$$\delta = 23.45 \sin\left[\frac{360}{365}(n - 81)\right], \tag{2.2}$$

where n represents the day number, with January 1^{st} as day 1.

The variation in the solar declination angle throughout the year is shown in Figure 2.2. The solar declination reaches its maximum on June 21^{st} at $23.45°$ and its minimum on December 21^{st} at -$23.45°$.

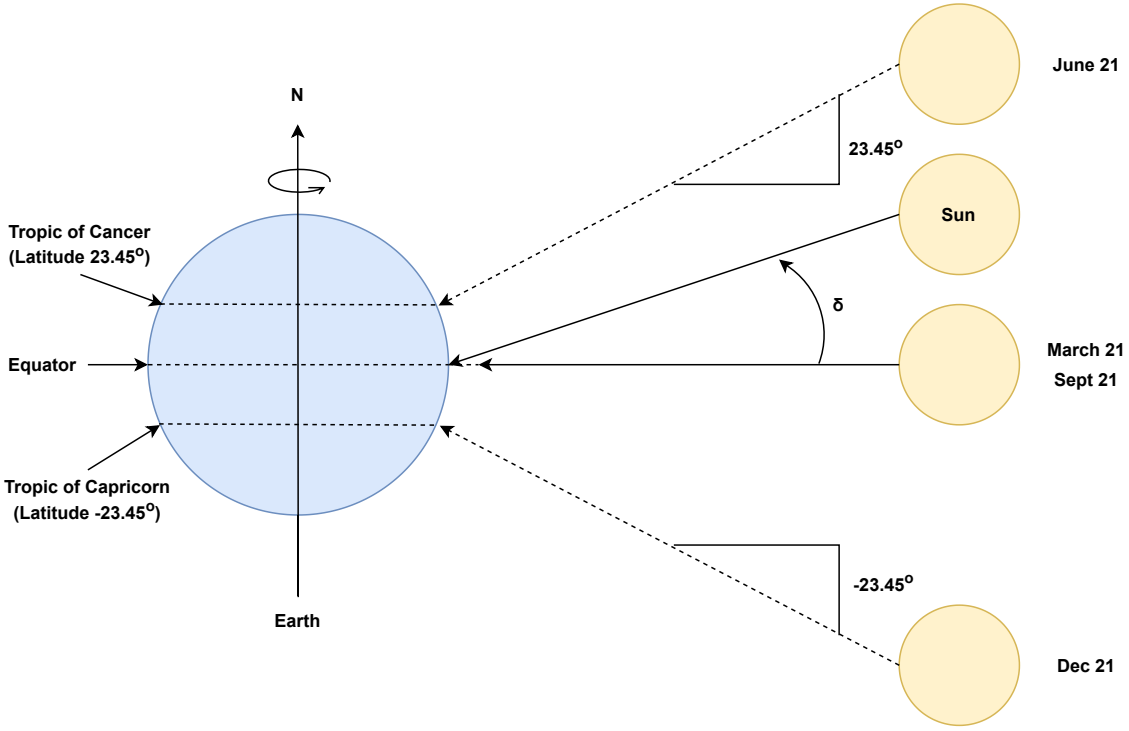

Figure 2.2: Solar declination angle through the year. *Source:* Redrawn Figure as shown in [8, p.193].

2.2.3 Solar Time

Most solar applications require the use of Solar Time (ST), where solar noon is used as the reference. However, there are situations where Civil Time (CT) (also known as local time) is required. In order to convert between CT and ST, two factors must be accounted for. [8]

Firstly, a correction factor is made to account for the effects of the elliptical orbit of the earth around the sun which causes variation in the length of a solar day throughout the year. The length between a 24 hour day and a solar day varies through the year. This variation is determined using equation (2.3), known as the Equation of Time. [8, p.207]

$$E = 9.87 \sin 2B - 7.53 \cos B - 1.5 \sin B \ \ (minutes) \tag{2.3}$$

where,

$$B = \frac{360}{364}(n - 81) \ \ (degrees) \tag{2.4}$$

In equation (2.4), n represents the day number as previously stated.

The second factor is a longitude adjustment made to account for the different time zones around the world. The earth can be divided into 24 time zones, with each zone being 15° of longitude and 1 hour apart from the next. The local time meridian is the line of longitude which, ideally, passes through the centre of any given time zone. The longitude adjustment is related to the length of time taken for the sun to travel from the local time meridian to the line of longitude of the observer. It takes the sun 4 minutes to travel 1° west, since each 1 hour time zone spans 15°. [8]

After both these adjustments are made, the relationship between ST and CT is determined using equation (2.5) [8, p.207].

$$ST = CT + \frac{4 \ \ minutes}{1^\circ}(Local \ \ Time \ \ Meridian - Local \ \ Longitude)^\circ + E \tag{2.5}$$

2.2.4 Solar Azimuth and Altitude

Three coordinates are required in order to describe the position of the sun at any given time of day. However, if the distance between the earth and the sun is assumed to be constant, then only two angles are needed to express its position in the sky [9]. The first of these angles is called the solar azimuth angle ϕ_S, and the second angle is called the solar altitude angle β [8].

The position of the sun, expressed in its altitude and azimuth angles, is shown in Figure 2.3. The convention for the use of azimuth angles in the Southern Hemisphere is that they are measured relative to North. The azimuth angle is positive before solar noon when the sun is in the east, 0° at solar noon and negative after solar noon when the sun is in the west.

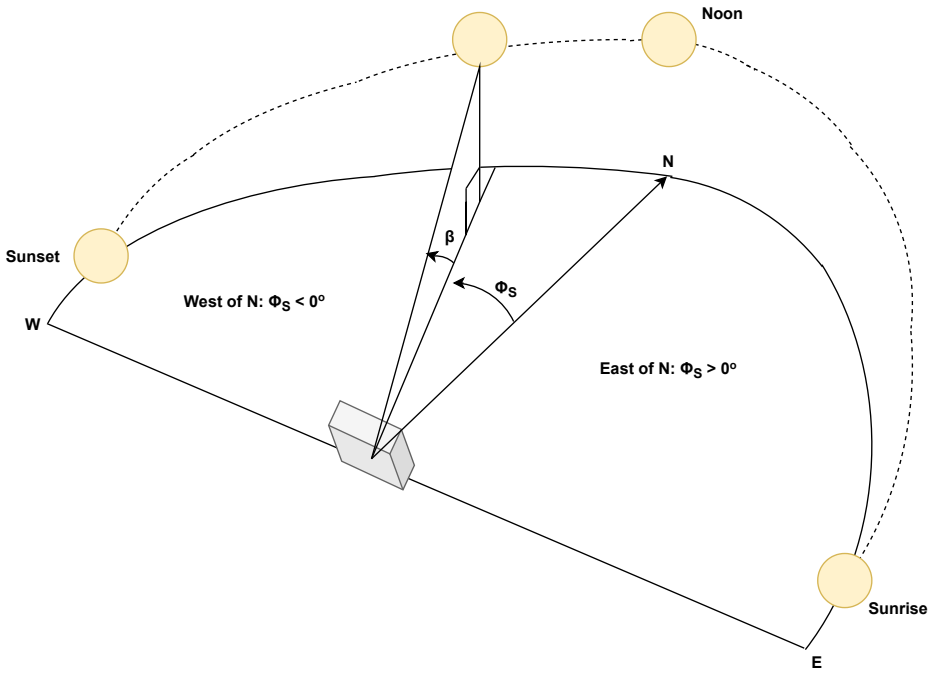

Figure 2.3: Solar azimuth and altitude angles are used to describe the position of the sun in the sky. *Source:* Redrawn Figure as shown in [8, p.197].

The solar altitude and azimuth angles are dependent on geography, time of day and day number. The solar altitude angle is described using equation (2.6) and the solar azimuth angle is determined using equation (2.7). [8, p.197]

$$\beta = \arcsin(\cos L \cos\delta \cos H + \sin L \sin\delta) \tag{2.6}$$

$$\phi_S = \arcsin\left(\frac{\cos\delta \sin H}{\cos\beta}\right) \tag{2.7}$$

In these equations: L is latitude, δ is solar declination angle and H is the Hour angle. All these variables are expressed in degrees. The Hour angle H is described by equation (2.8). [8, p.198]

$$H = \left(\frac{15^\circ}{hour}\right) \times (hours \;\; before \;\; solar \;\; noon) \tag{2.8}$$

It is possible for ϕ_S to have a magnitude of more than 90° from North. In order to determine whether the magnitude of ϕ_S is greater than or less than 90°, equation (2.9) is used. [8, p.198]

$$if \quad \cos H \geq \frac{\tan\delta}{\tan L}, \quad |\phi_S| \leq 90^\circ \;\; else, \;\; |\phi_S| > 90^\circ \tag{2.9}$$

2.3 Solar Radiation

2.3.1 Spectrum

Every object emits energy in the form of electromagnetic radiation. The emitted energy is determined by the temperature of the object. These objects are compared to a blackbody in order to describe the radiation which they emit. A blackbody is a theoretical object defined as being both a perfect absorber and perfect radiator of all electromagnetic radiation. A blackbody does not reflect any energy, nor does it allow any energy to pass through it. [8]

Planck's law, shown in equation (2.10), as presented in [9, p.22], is used to describe the radiation emitted by a blackbody as a function of wavelength and temperature.

$$E_\lambda = \frac{2\pi hc^2\lambda^{-5}}{e^{\frac{hc}{\lambda kT}} - 1} \ (W/m^2/unit\ \ wavelength\ \ in\ \ meters), \tag{2.10}$$

where:
E_λ is the energy density per unit area,
h is Planck's constant,
c is the speed of light in a vacuum,
k is Boltzmann's constant,
λ is wavelength,
T is the temperature of the blackbody in degrees Kelvin.

The power emitted in between a pair of wavelengths is determined by integration of equation (2.10) and setting the two wavelengths as the limits of integration. Therefore, the total power that is radiated is obtained by determining the total area under Planck's curve. The total area under Planck's curve is described by Stefan-Boltzmann's law of radiation [8, p.187]:

$$E = \sigma AT^4 \ \ (Watts), \tag{2.11}$$

where:
E is the total emitted power in watts,
σ is the Stefan-Boltzmann constant,
T is the temperature of the blackbody in degrees Kelvin,
A is the surface area of the blackbody in square meters.

Wien's displacement rule can be applied to a blackbody radiation curve in order to determine the wavelength at which the spectrum will be at its maximum value. Wien's displacement rule is described by equation (2.12). [8, p.187]

$$\lambda_{max}(\mu m) = \frac{2898}{T(K)}, \tag{2.12}$$

where λ_{max} is the wavelength in micrometers and T is the temperature in Kelvin.

The spectrum of light which originates from the sun is called solar irradiance [10]. The sun can be approximated to be a blackbody with a surface temperature of 5800 K.

The Planck curve of a 5800 K blackbody is shown in Figure 2.4. It can be seen that approximately 7% of the emitted power is in the ultraviolet spectrum, 47% is in the visible spectrum and 46% is in the infrared spectrum [8].

The comparison between the actual solar radiation received outside the atmosphere and an ideal 5800 K blackbody is shown in Figure 2.5 using data obtained from NREL [11]. It is apparent that there is a close correlation between the two spectra. The area underneath the Planck curve of the 5800 K blackbody is scaled to approximately 1.37 kW/m^2 - the same as the solar irradiance measured in space outside the atmosphere.

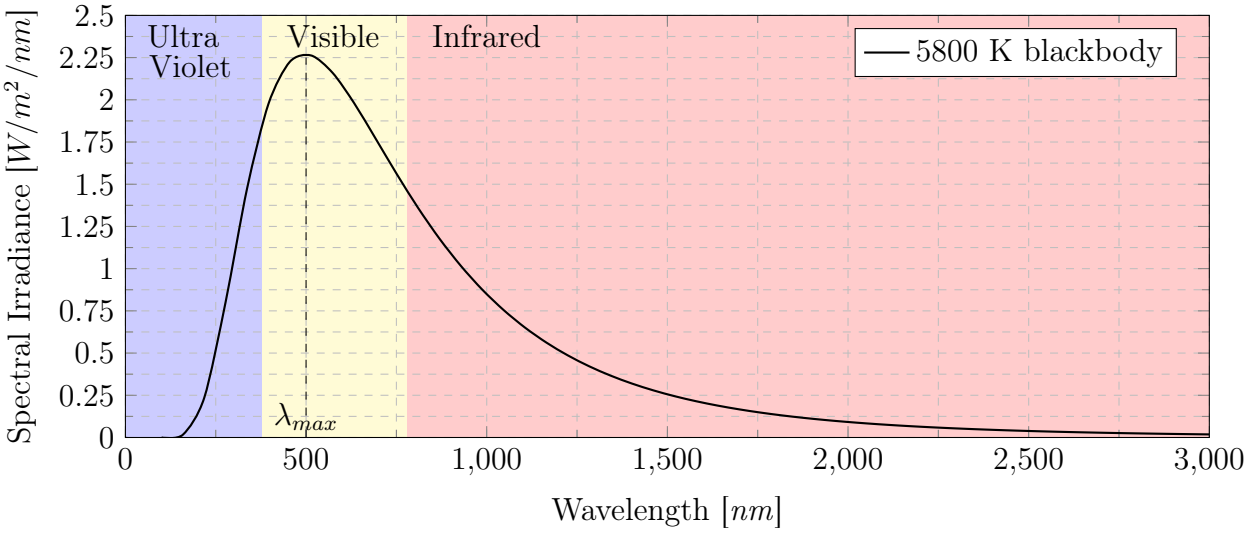

Figure 2.4: Spectral irradiance of an ideal 5800 K blackbody.

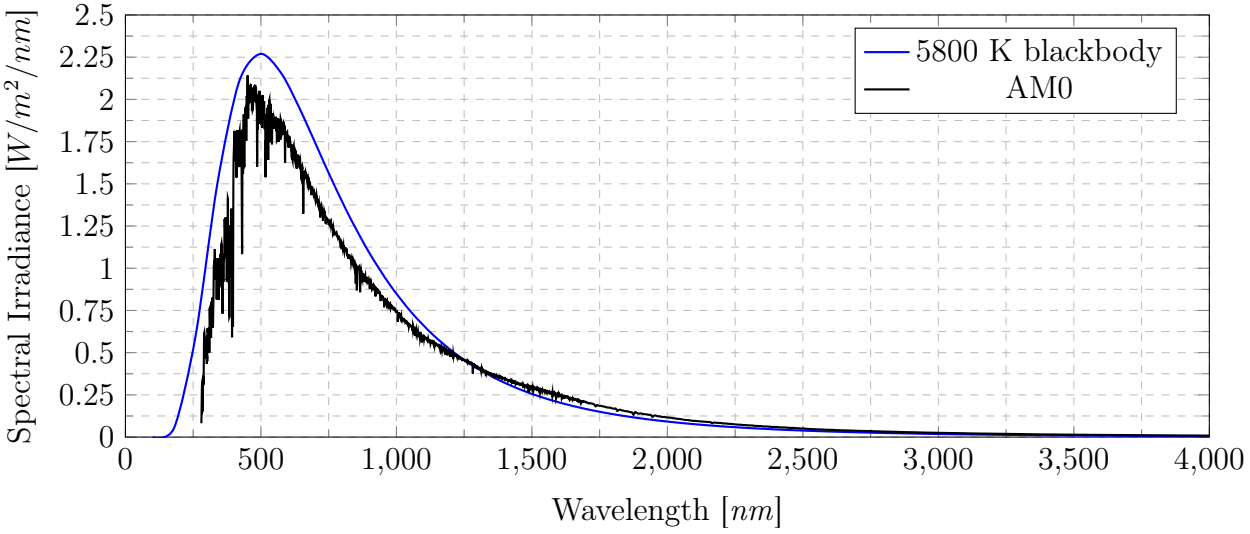

Figure 2.5: Spectral irradiance of an ideal 5800 K blackbody compared with the AM0 solar spectrum.

2.3.2 Air Mass

The atmosphere is responsible for the attenuation of solar radiation from outer space to the surface of the earth. The attenuation is directly affected by the distance of the atmosphere through which the radiation must travel. Outside the atmosphere, the intensity of the received solar irradiance is approximately 1367 W/m^2. This value of solar irradiance is known as the solar constant [12]. The spectrum at the interface of the atmosphere and outer space is know as the AM0 spectrum. The AM0 reference spectrum was introduced in 2000 by the American Society for Testing and Materials (ASTM) [10].

Air mass is the ratio of the length of the path actually travelled by the rays of the sun through the atmosphere to the length of the shortest possible path that could be travelled. This is illustrated in Figure 2.6. As the air mass ratio increases, attenuation on the solar spectrum is greater. [8]

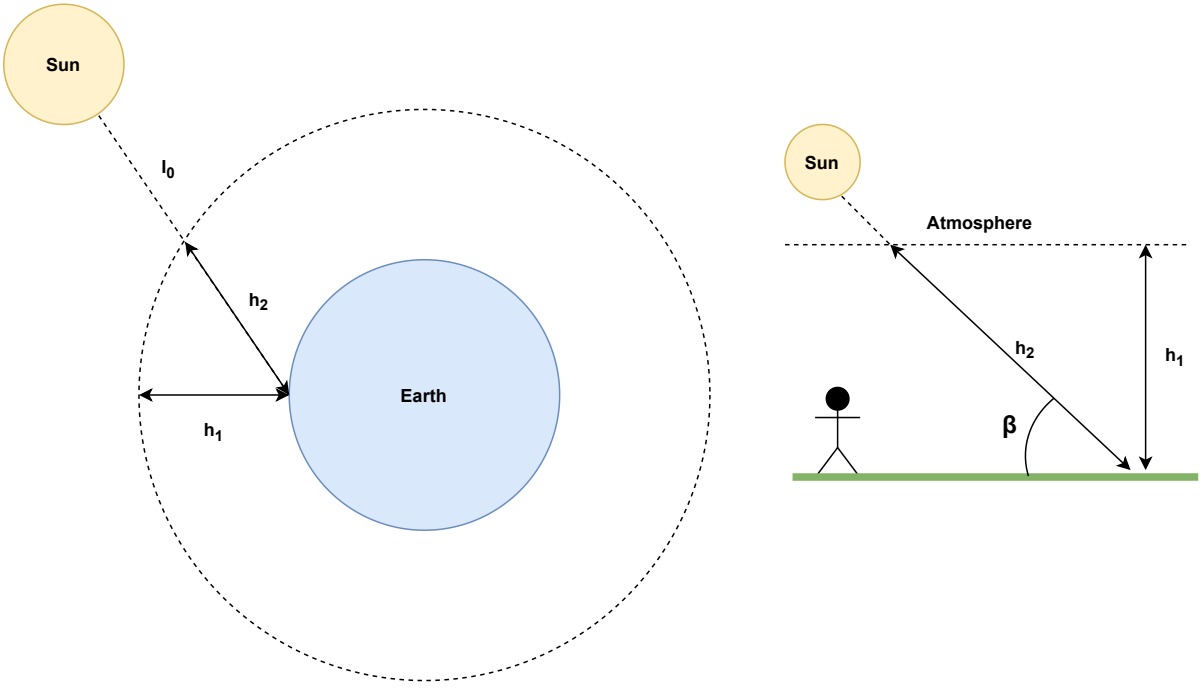

Figure 2.6: Air mass ratio is the ratio of h_2 to h_1. The air mass ratio is 1 when the sun directly overhead. *Source:* Redrawn Figure as shown in [8, p.190].

If the earth is assumed to be flat, the air mass ratio is described by equation (2.13) [8, p.189].

$$m = \frac{h_2}{h_1} = \frac{1}{\sin\beta}, \tag{2.13}$$

where h_1 is the path length through the atmosphere when the sun is directly above the terrestrial surface, h_2 is the path length through the atmosphere that the rays of the sun actually travel and β is the solar altitude angle.

If a flat earth assumption is not made, the air mass ratio is determined using equation (2.14). This accounts for the fact that the atmosphere is spherical. [8, p.214]

$$m = \sqrt{(708 \sin \beta)^2 + 1417} - 708 \sin \beta, \tag{2.14}$$

where β is the solar altitude angle.

When the air mass ratio is 1 (i.e. AM1), it means the sun is directly overhead and its rays travel the shortest possible path through the atmosphere down to the surface of the earth. By definition, AM0 is when there is no atmosphere. This is the extraterrestrial solar spectrum just outside the atmosphere. [8]

In most terrestrial photovoltaic (PV) applications, the ASTM G-173-03 standard is used. It contains spectra at AM1.5 [10]. The solar spectrum at AM1.5 has been normalised so that is has a power density of 1000 W/m^2 [13]. At AM1.5, 2 % of the emitted solar radiation is in the ultraviolet spectrum, 54 % is in the visible spectrum and 44 % is in the infrared spectrum [8].

A comparison between the AM0 and the AM1.5 spectra is shown in Figure 2.7. The AM1.5 Direct-Circumsolar spectrum accounts for the direct beam radiation, as well as the radiation that is scattered within a 2.5° angle of the sun. The AM1.5 Global-Tilted spectrum accounts for all hemispherical radiation received by a collector that is facing the sun and tilted at an angle of 37°.

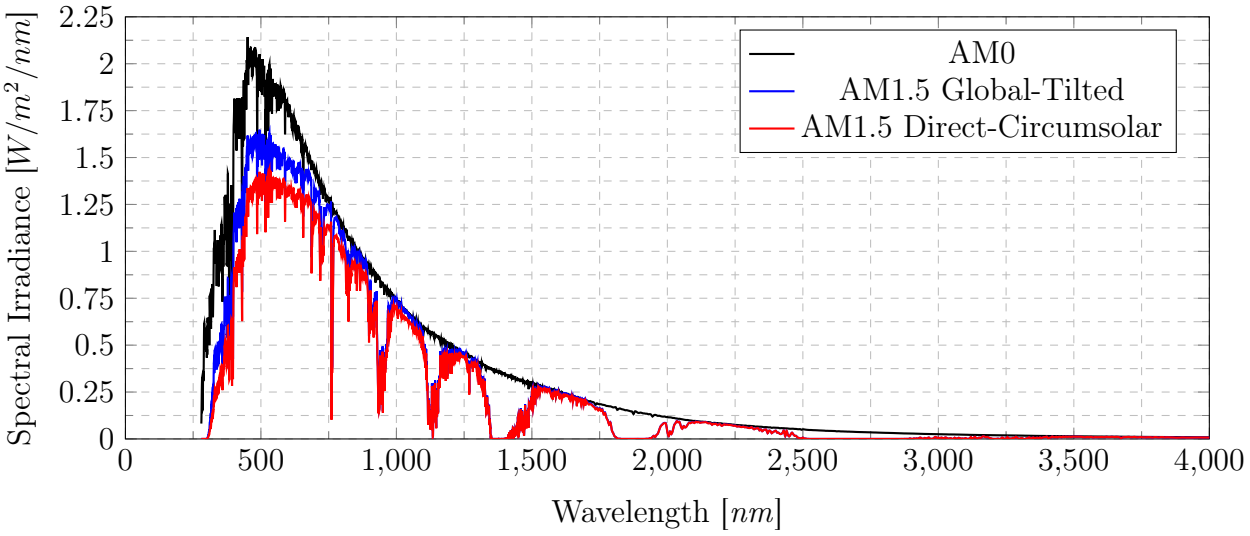

Figure 2.7: Spectral irradiance shown at AM0, AM1.5 Global and AM1.5 Direct under the ASTM G-173-03 standard. *Source:* Redrawn Figure as presented by [11].

2.3.3 Direct and Diffuse Radiation

The extraterrestrial solar insolation received on the surface of the earth is broken down into three components: direct beam radiation, diffuse radiation and reflected radiation. Direct radiation passes through the atmosphere in a straight line, diffuse radiation is scattered by particles in the atmosphere and reflected radiation is reflected off of the

earth and other surrounding surfaces [8]. Direct, diffuse and reflected radiation are shown striking a collector in Figure 2.8.

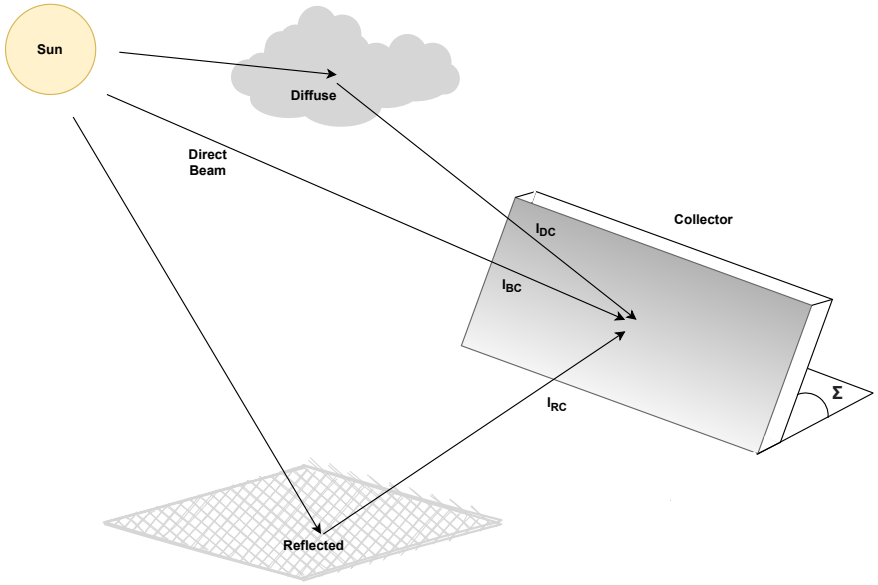

Figure 2.8: Direct, diffuse and reflected components of solar radiation striking a collector. *Source:* Redrawn Figure as shown in [8, p.212].

The amount extraterrestrial solar insolation received is dependent on the distance between the sun and the earth as well as the varying intensity of the sun. The daily variation in extraterrestrial solar insolation can be described by equation (2.15) [8, p.213].

$$I_0 = SC \cdot \left[1 + 0.034 \cos\left(\frac{360n}{365}\right)\right] \quad (W/m^2), \tag{2.15}$$

where I_0 is the extraterrestrial solar insolation, SC is the solar constant (1370 W/m^2) and n is the day number.

On average, less than 50 % of extraterrestrial irradiance is received on the surface of the earth as direct beam radiation over the course of a year. However, on clear days it is possible for over 70 % of extraterrestrial irradiance to be received as be direct beam radiation. The received solar radiation is attenuated by air mass, as well as atmospheric factors such as atmospheric water vapor, atmospheric ozone, dust, clouds and turbidity. [8]

Direct beam radiation is described by equation (2.16), where attenuation is treated as an exponential decay function [8, p.213].

$$I_B = Ae^{-km}, \tag{2.16}$$

where I_B is the direct beam radiation at the surface of the earth, A is the apparent extraterrestrial radiation, k is the optical depth and m is the air mass. The values for A and k are determined using equations (2.17) and (2.18) respectively for the Clear Day Solar Flux Model. [8, p.214]

$$A = 1160 + 75 \sin\left[\frac{360}{365}(n - 275)\right] \quad (W/m^2) \tag{2.17}$$

$$k = 0.174 + 0.035 \sin\left[\frac{360}{365}(n - 100)\right] \tag{2.18}$$

According to the Clear Day Solar Flux Model developed by the American Society of Heating, Refrigerating and Air-Conditioning Engineers (ASHRAE), the diffuse irradiance on a horizontal surface is proportional to the direct beam irradiance regardless of the position of the sun in the sky. The diffuse irradiance on a horizontal surface is described by equation (2.19). [8, p.218]

$$I_{DH} = I_B \left(0.095 + 0.04 \sin\left[\frac{360}{365}(n - 100)\right]\right) \tag{2.19}$$

2.4 Measurement Devices

2.4.1 Irradiance Measurements

2.4.1.1 Pyrheliometers

A pyrheliometer is an instrument used to measure the irradiance received directly from the sun - direct normal irradiance (DNI). All pyrheliometers are required, by the World Meteorological Organisation (WMO), to possess a 5° field-of-view with an opening half-angle of 2.5°. Pyrheliometers are mounted on solar trackers to ensure that they are pointed towards the sun throughout the day. [14]

The basic construction of a pyrheliometer is shown in Figure 2.9.

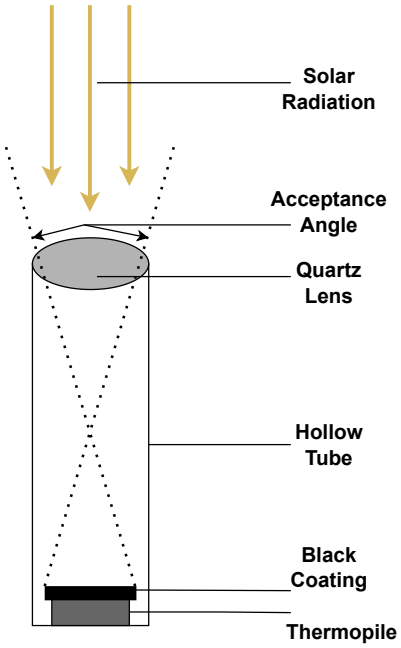

Figure 2.9: Construction of a Pyrheliometer.

A pyrheliometer consists of a hollow tube with a quartz lens on one end and a thermopile with a black coating on the other end. The solar radiation enters the hollow tube through the quartz lens. This lens is designed such that it allows wavelengths from 200 nm - 4000 nm to pass through, but blocks thermal radiation with wavelengths greater than 4000 nm. The light that enters the tube heats the black thermopile, causing it to output a voltage proportional to the temperature difference across it due to the Seebeck effect. If the pyrheliometer has no onboard electronics to convert the voltage to a digital signal, its output signal is the output voltage of the thermopile. If onboard electronics are included, the output signal could be digital, such as Modbus RTU. The voltage at the output of the thermopile is calculated using equation (2.20). [14]

$$U = \sum_{i=0}^{N} u_i = N \cdot \varsigma \cdot \Delta T \tag{2.20}$$

where:

U is the output voltage,

N is the number of thermocouples that make up the thermopile,

ς is the Seebeck coefficient of the type of thermocouple,

ΔT is the temperature difference between the black surface of the thermopile and the body of the instrument.

2.4.1.2 Pyranometers

A pyranometer is an instrument used to measure the received irradiance from a hemispherical field-of-view. Unlike pyrheliometers which measure only direct irradiance, pyranometers measure global irradiance - which includes both direct and diffuse irradiance. Pyranometers can be mounted on a horizontal surfaces to measure global horizontal irradiance (GHI) or they can be mounted on tilted surfaces which correspond to the plane of array of PV panels to measure global tilted irradiance (GTI). [15]

The basic construction of a pyranometer is shown in Figure 2.10.

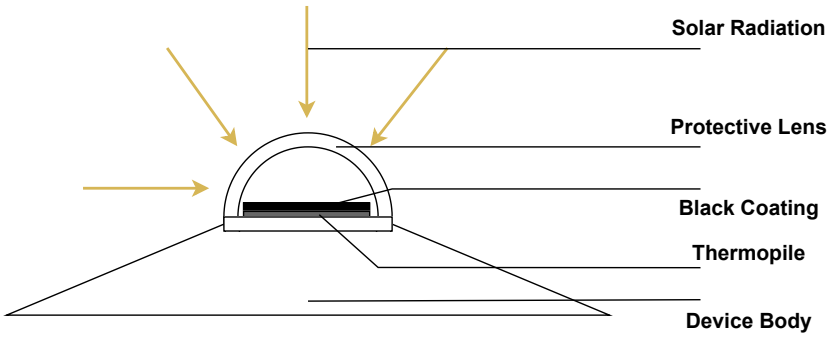

Figure 2.10: Construction of a Pyranometer.

A pyranometer consists of either one or two concentric domes placed over a thermopile with a black, heat-absorbent coating. Like the quartz lens on a pyrheliometer, the domes on a pyranometer act as filters to allow radiation in the wavelengths from 300 nm - 3000 nm to pass through, while blocking thermal radiation with wavelengths longer than 3000

nm. The radiation that is allowed to pass through the domes causes the temperature of the thermopile to rise. This results in an output voltage proportional to the temperature difference across the thermopile to be generated due to the Seebeck effect. The output signal of a pyranometer can either be the output voltage of the thermopile, or a digital signal such as Modbus RTU. As with a pyrheliometer, the voltage at the output of the thermopile is calculated using equation (2.20). [15]

2.4.2 Spectral Irradiance Measurements

2.4.2.1 Spectral Measurement

An optical spectrometer is a device that is used to measure the intensity of light in various distinct wavelengths. The most common configuration used in optical spectrometers is the Czerny-Turner configuration. The basic construction of a Czerny-Turner spectrometer is shown in Figure 2.11. [16]

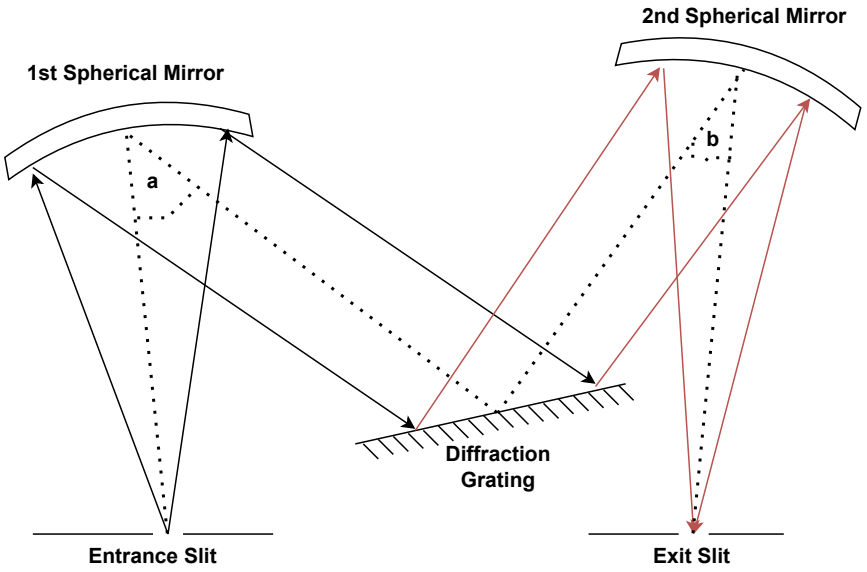

Figure 2.11: Czerny-Turner Spectrometer.

Light enters the spectrometer through the entrance slit. The light strikes a curved mirror, routing it on to the diffraction grating or prism. The function of the diffraction grating is to separate the light into its constituent wavelengths. These separated wavelengths are then reflected to a second curved mirror, routing the light to the exit slit. An optical detector then records the intensity of light which strikes its pixels. Each pixel corresponds to a specific frequency of light, and outputs a signal proportional to the intensity of light of that specific frequency. [16]

2.4.2.2 Spectral Reconstruction

The prohibitive costs involved in acquiring a field spectroradiometer (FSR) to perform spectral measurements at a specific location led Tatsiankou et al. [17] to develop an algorithm to be used with a multi-channel filter radiometer (MFCR) to accurately reconstruct

the solar spectrum at a low cost. An MCFR is a device used to measure irradiance is several narrow wavelength bands using photodiodes and interference filters.

The optimal wavelength bands in which measurements are made were found to be 420 nm, 500 nm, 780 nm and 1050 nm to determine the effects of atmospheric aerosols, 610 nm to determine the effects of ozone and 940 nm to determine the effects of water vapor. The measurements made in these wavelength bands are fed into the developed algorithm and used to accurately reconstruct the solar spectrum with an RMS error of under 1.5% over 96% of the 350 nm - 1830 nm range. [17]

This method of spectral reconstruction is used by Spectrafy in their SolarSIM spectral irradiance meters.

2.5 Irradiance Prediction

Various irradiance forecasting methods exist. Each method is better suited to certain applications over others. The implemented forecasting method for a specific application is dependent primarily on the tools and data available to forecaster. Typically, the required data includes temperature measurements, irradiance measurements and geographic location. [18]

Most irradiance forecasting work is related to the prediction of Global Horizontal Irradiance (GHI), as it is important for photovoltaic applications. However, Direct Normal Irradiance (DNI) prediction is important for applications such as Concentrated Solar Power (CSP). [19]

Irradiance forecasting methods are generally categorised as either physical methods, which make predictions using solar and PV models, or statistical methods, which make predictions by using historical data to train models. [18]

2.5.1 Numerical Weather Prediction

Numerical Weather Predication (NWP) models are widely used in irradiance forecasting. They simulate atmospheric conditions at a certain location by dividing the relevant area into a grid. The atmosphere above this area is assembled by stacking these grids on top of one another such that the full atmospheric depth is accounted for [20]. Meteorological data is used to determine the initial conditions needed to solve equations to predict the atmospheric characteristics at the center of each grid block [20]. NWP models are found to predict irradiance most accurately for forecasts from 6 hours ahead, up to a few days ahead [21]. NWP models are found to over predict irradiance and under predict cloud cover. This is because they usually have a spatial resolution of more than 10 km which inhibits their ability to resolve smaller cloud details or larger convective clouds [22].

2.5.2 Machine Learning

Machine Learning (ML) algorithms aim to predict irradiance by using historical weather data and irradiance data as inputs. The most popular machine learning algorithms used for irradiance forecasting include Artificial Neural Networks (ANN) and Support Vector

Machines (SVM). [23]

Artificial neural networks consist of an input layer, hidden layers and an output layer of neurons. The ANN is trained to adjust the weights between the neuron connections in these layers such that the error at the output is minimized [23]. Ozgoren et al. [24] developed an ANN model based on the multi-nonlinear regression (MNLR) method to estimate global irradiance. Data collected over a 6 year period from 27 different measurement stations was used to train the model. The data used to train the model includes location data, atmospheric temperature, soil temperature, humidity, wind speed, rainfall, atmospheric pressure, and sunshine duration. The model accurately predicts irradiance, with mean absolute percentage error (MAPE) of 5.34 %. Theocharides et al. [25] successfully implemented an ANN model using weather parameters, solar elevation and solar azimuth angles as inputs. The model accurately predicts irradiance from 1 to 6 hours ahead with MAPE from 4.10 % to 8.19 % respectively. The MAPE from the ANN model developed by Rezrazi et al. [26] is found to reach 1.17 %, surpassing many other models. The input data used to train the ANN includes air temperature, humidity, number of days and local time.

SVM is a supervised machine learning algorithm first developed in 1992 [23]. Belaid and Mellit [27] make use of SVM to predict daily and average monthly GHI. It is found that only a few input parameters such as ambient temperature, sunshine duration and received irradiance are needed for accurate prediction. Chong et al. [28] developed an SVM to predict irradiance 1 hour ahead using historical data regarding solar irradiance, wind speed, humidity, air pressure and rainfall. It is found that the developed SVM is less accurate when wind speed data is considered. VanDeventer et al. [29] improve on the conventional SVM model by introducing a genetic algorithm to optimize the SVM. This model uses irradiance, temperature and the output power of a PV system as inputs.

2.5.3 Cloud Movement

The short-term variation in cloud cover throughout the day is difficult to predict using the traditional forecasting methods mentioned above. For accurate short-term predictions, the clouds in the sky must be observed using a camera. The images captured by these cameras allows for the velocity of the clouds to be determined. The images can be captured either by satellite, or by ground based stations. [30]

Satellite images were used by Hammer et al. [31] to determine the development of clouds to improve on irradiance forecasting. This method is found to predict solar irradiance on time scales between 30 minutes to 2 hours with less than 5 % error for hourly forecasts. Ground based cameras with a wide field of view have been proposed to capture images of the sky [32], [33]. These images are processed to determine the velocity vector of clouds using an optical flow algorithm. Dev et al. [33] find that prediction accuracy is high for very short term predictions, and decreases for longer term forecasts. It is proposed that meteorological data such as wind speed is used to improve forecasting.

2.5.4 Existing Data Collection Methods

Most data used in irradiance prediction models is retrieved from existing databases of meteorological data. As a result, very few measurement stations exist which are dedicated to data collection with the purpose of irradiance forecasting.

Traditional weather stations consist of a variety of instruments used to record meteorological data. These instruments include thermometers and thermographs for temperature measurements, hygrometers and dew point probes for humidity measurements and barometers for air pressure measurements. Direct and global solar irradiance measurements are made using pyrheliometers and pyranometers respectively. Reflected radiation is recorded using albedometers and sunshine duration is recorded using a Cambell-Stokes recorder. Other meteorological parameters such as wind speed and rainfall are also recorded. [34]

Long et al. [35] developed a ground based sky imaging system which is used to predict cloud movement and, as a result, improve irradiance predictions. The total sky imager (TSI) consists of a digital camera facing down on a hemispherical mirror. This configuration provides a horizon-to-horizon view of the sky. Images are captured at a maximum rate of once every 10 seconds at a 352 $\times$ 288 pixel resolution in a 24-bit colour JPEG format. The TSI captures images in a 160° field of view. This TSI is now a commercially available product. Due to the high cost and limited resolution of the aforementioned TSI, researchers such as Dev et al. [36], developed a whole sky imager (WSI). The proposed WSI uses mostly off-the-shelf components and costs $2500, compared to the cost of $30 000 for the TSI. It uses a digital camera with a fish-eye lens to capture images with a 180° field of view of the sky at a resolution of 5184 $\times$ 3456 pixels. A sun-blocker is used to obstruct direct sunlight to reduce glare in the image. It is controlled using a built-in laptop. All devices are placed in a hermetically-sealed enclosure. Several other similar systems have been developed [37], [38].

It is interesting to note that no solar spectral irradiance data has been used in any of the aforementioned irradiance forecasting methods.

2.6 PV Modules

2.6.1 Background

All solar cells use the photovoltaic effect as their basis of operation. The photovoltaic effect was first observed in 1839 by a French physicist named Edmund Becquerel [39]. The photovoltaic effect is the process in which an electrical voltage is generated in a material when it is struck by light [40].

The photovoltaic effect is illustrated in Figure 2.12. Solar radiation strikes a p-n junction and causes electrons to flow towards the n-type semiconductor and holes to flow towards the p-type semiconductor. This results in current flow.

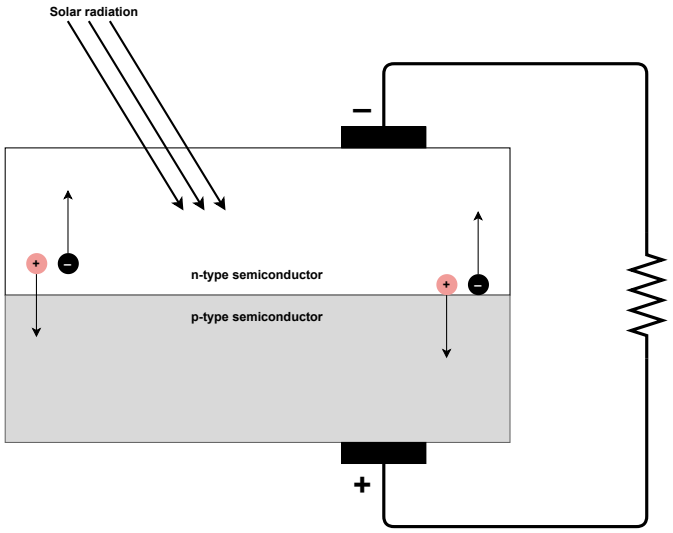

Figure 2.12: Illustration of the photovoltaic effect.

Various semiconductor materials are used to manufacture PV cells. Silicon is the most popular material used, with silicon PV panels accounting for up to 95% of all panels in existence [41]. A PV module consists of an array of PV cells which are connected together in order to increase voltage and current output.

PV modules are rated under standard test conditions (STC). These conditions include a solar cell temperature of 25°C, solar irradiance of 1000 W/m^2 and an air mass factor of 1.5 under the AM1.5 spectrum. These conditions allow for accurate comparisons of different PV modules against each other under the same conditions. Standard test conditions are rarely met in practical applications. [42]

2.6.2 Operation of PV Modules

An electron in a covalent bond must have an energy level that allows it to fit within certain energy bands, such as those shown in Figure 2.13. The upper energy band is the conduction band, and the electrons found in this band are responsible for current flow. In order for an electron to to enter the conduction band from the valence band, it must acquire the band-gap energy E_g. An electron must acquire 1.12 eV to travel from the valence band to the conduction band in a silicon semiconductor. This energy, in the case of a PV cell, is acquired through solar radiation. An electron may move into the conduction band every time a photon with an energy of E_g is absorbed by a PV cell. Photons striking a solar cell with less energy than E_g will have their energy wasted as heat, since they can not dislodge an electron into the conduction band. A single photon can only dislodge one electron, therefore, photons with greater energy than E_g will have all their excess energy above E_g wasted as heat. [8]

The relationship between the energy of a photon and its wavelength is described by equation 2.21 [8, p.259].

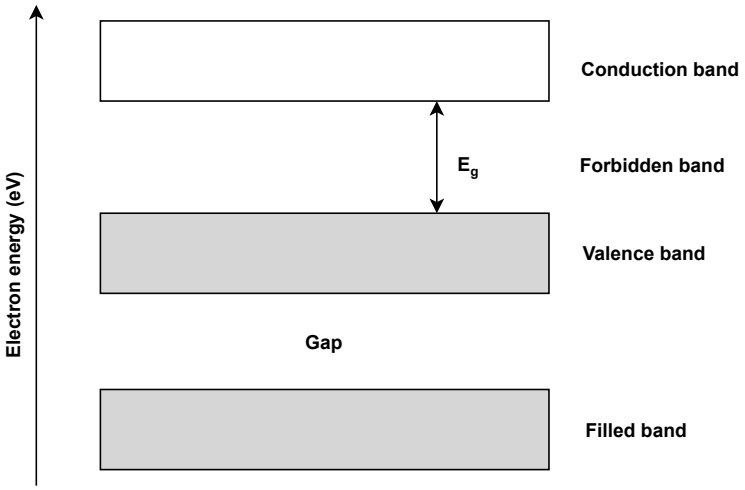

Figure 2.13: Energy bands for semiconductors. *Source:* Redrawn Figure as shown in [8, p.257].

$$E = \frac{hc}{\lambda}, \tag{2.21}$$

where E is the photon's energy in J, h is Planck's constant and c is the speed of light in a vacuum.

2.6.3 Efficiency of Different PV Technologies

Many different types of PV modules are available. The PV technology used in the modules is broadly grouped into 3 categories: Crystalline, Thin Film and Emerging technologies. Crystalline modules are typically made from either monocrystalline or polycrystalline silicon and can reach conversion efficiencies of between 20.4 % and 24.4 %. Thin film panels are less efficient, with conversion efficiencies of approximately 19 %. These panels are usually made of cadmium telluride (CdTe) or copper indium gallium diselenide (CIGS). Emerging technologies include perovskite and organic panels, with efficiencies of 17.9 % and 11.7 % respectively. Newer technologies, such as multi-junction gallium arsenide (GaAs) panels have reached efficiencies of almost 40 %. The above mentioned efficiencies of each of these PV technologies are reached under controlled lab conditions. Commercially available PV panels are less efficient in practice. [43]

The solar spectrum is blue-shifted during the summer months and red-shifted during the winter months [44]. Schweiger and Hermann [44] analysed the effects of spectral variations on the solar spectrum on 8 different PV technologies. The spectral response of the panels is measured in the wavelength range from 300 nm to 1600 nm. It is seen that different PV technologies reach peak efficiencies at different wavelengths. This is expected as different PV materials have different quantum efficiencies. The peak efficiency for the CdTe panel is reached at a wavelength of approximately 800 nm, compared to 950 nm for polycrystalline silicon and 1030 nm for monocrystalline silicon. The spectral response range for each panel is also unique. Some panels, such as monocrystalline silicon have a much wider response than CdTe. It is found that certain panels are less sensitive to

spectral variations than other panels.

Atmospheric ozone, water vapor and aerosol optical depth attenuate the solar spectrum at different wavelengths. Consequently, the effects of this attenuation on PV performance is dependent of the spectral response of the PV technology under consideration [45]. Marion [46] analysed the impact of spectral variations caused by the aforementioned factors on 4 different PV technologies. It is found that copper indium gallium selenide (CIGS) PV modules are the least sensitive to spectral variations due to their wider spectral response range. Cadmium telluride panels and amorphous silicon panels are found to be more sensitive to the effects of atmospheric water vapor.

Other, more well known, factors affecting the efficiency of PV modules include received irradiance and PV cell temperature. Islam et al. [47] demonstrate the increase in PV module output with the increase in incident irradiance. It is also shown that the efficiency of the module is improved with increased irradiance. This due to a decrease in the internal series resistance of the PV module at higher irradiance levels. The efficiency of the tested panel increases from 7.7 % at an irradiance of 105 W/m^2 to 13.6 % at an irradiance of 602 W/m^2, with internal series resistance decreasing from 128.15 ohms to 14.35 ohms. Zaini et al. [48] demonstrate both experimentally and through simulation that the output and the efficiency of a PV module decrease as the temperature of the module is increased. The output power of the tested PV module decreases by 8.35 % as its temperature increases from 25.7° to 60.7°. Temperature is the only variable in the experiment, all other parameters are kept constant.

Therefore, it is seen that the efficiency of a PV panel is affected by many factors, such as the quantum efficiency of the PV material used, variations in temperature, variations in incident irradiance, and variations in the solar spectrum caused by air mass, aerosol optical depth, precipitable water vapor and atmospheric ozone.

2.7 Chapter Review

The orbit of the earth around the sun was investigated in this chapter. This provided an understanding of how the sun moves across the sky throughout the day, and how the position of the sun is described using various solar angles. Accurate estimation of these angles is important, as the system designed in this thesis must accurately point instruments towards the sun for measurements. The solar spectrum and its attenuation due to air mass is then discussed, as this influences the performance of PV devices. Various irradiance prediction models were investigated to determine what data is currently used in these models and how this data is obtained. This is useful as a reference of what data must be collected by the designed system. Parameters affecting the performance of PV modules are then investigated. The factors that are not accounted for in existing models, such as spectral irradiance, are identified. This information is used in Chapter 3 to determine the system requirements.

Chapter 3

Device Selection and System Design

3.1 Introduction

This chapter discusses and motivates the decisions made in the design of the system. It begins by identifying and motivating the system requirements and presenting a high-level system diagram. The reasoning behind the selection of each device is then provided, along with a summary of all important device characteristics. The power and energy requirements of the system are determined, and the power supply is designed. Finally, the design of the mechanical aspects of the system is presented.

3.2 System Design Objectives

Irradiance forecasting is an important tool used to manage the output of PV power plants. It is seen in Chapter 2.5 that most irradiance prediction models use meteorological data obtained from the databases of weather stations. The data used in most models include temperature, humidity, air pressure and broadband irradiance measurements. In some cases, visual data in the form of sky images is used to predict irradiance by determining the motion of the clouds in front of the sun. From Chapter 2.6, it is determined that various factors affect the performance of PV modules, including temperature, broadband irradiance and, notably, spectral irradiance. However, software tools used in the PV industry and irradiance prediction models do not consider the effects of spectral irradiance, despite its impact on the performance of PV modules.

The primary objective of the measurement station designed in this thesis is to gather data that can be used to improve upon irradiance prediction models and PV software tools. In order to improve upon these models, spectral data and atmospheric data is collected in addition to the data used in current models, as mentioned above.

Consequently, the measurement station is designed to perform the following tasks:

- measure global solar irradiance
- measure direct solar irradiance
- measure the direct solar spectral irradiance
- measure the wide field of view solar spectral irradiance

- measure atmospheric parameters
- measure meteorological parameters
- capture photographs of the sun, clouds and other points of interest in the sky
- point instruments in any direction
- accurately track the movement of the sun across the sky
- successfully log and store all captured data
- interface with other devices for data transfer and debugging

Additionally, the measurement station is designed with the following considerations taken into account:

- it should be as compact as possible
- it should be lightweight
- it should be reasonably weather resistant
- it should be solar powered
- it should automatically perform pre-programmed tasks

The collection of the data listed above is essential. The measured parameters all affect the output of PV modules either directly (such as irradiance) or indirectly (such as atmospheric water vapour, which influences the solar spectrum). Some of the data is already used in PV software and irradiance models, but data on atmospheric parameters and spectral irradiance is not used. The advantage of this station is that all the data is collected from one source instead of relying on multiple sources. All the collected data is referenced to images of the sky in the direction in which measurements are made. This could be used to train machine learning algorithms to predict how spectral irradiance varies using photos as inputs. It is essential that the instruments can be pointed in any direction so that measurements can be taken at any point in the sky. The ability of the station to point the instruments accurately towards the sun is especially important. All the data must be logged and stored until the user can retrieve it. Data retrieval may occur once every few days or even weeks, especially if the station is deployed in a remote location. The station must be compact, lightweight, weather-resistant and solar powered so that it can easily be transported and used in various locations. It should perform its tasks automatically so that it can be deployed in isolated areas without the need for an operator.

3.3 Device Selection and Description

A high-level diagram of the system is presented in Figure 3.1 to provide an overview of the design. Each component in the system is discussed in detail further along in this chapter. More detailed diagrams highlighting the communication and power integration of the components are available in Chapter 3.5.

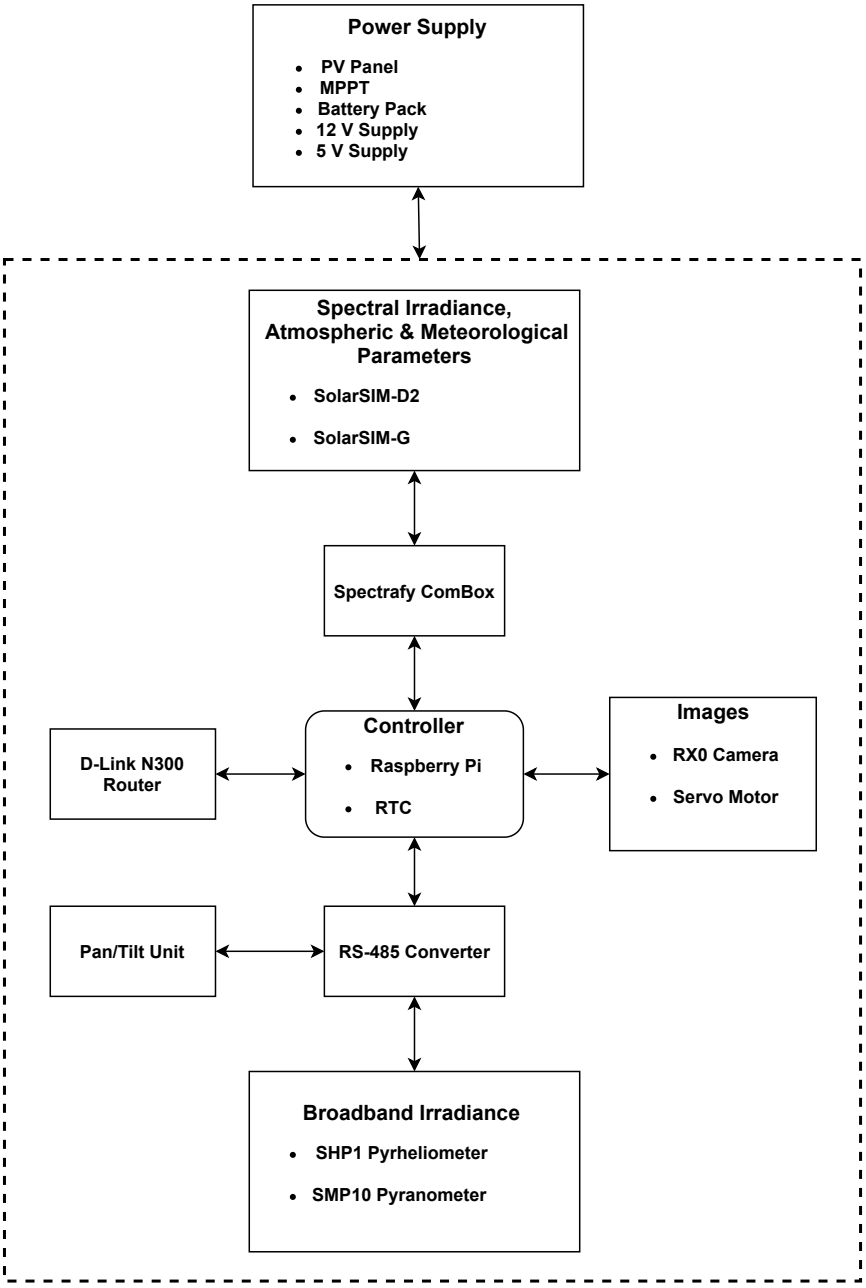

Figure 3.1: High-Level System Diagram.

3.3.1 Solar Irradiance Measurements

3.3.1.1 Pyrheliometer

The Kipp & Zonen SHP1 pyrheliometer [49], pictured in Figure 3.2, is selected to capture direct irradiance measurements. It uses a thermopile detector behind a quartz window to measure irradiance in the spectral range of 200 nm to 4000 nm within a 5° viewing angle. It has a 95% response time of fewer than 2 seconds, making it ideal for use in cases where consecutive measurements are taken quickly. It is a Spectrally Flat Class A pyrheliometer as per ISO 9060:2018 classification. Corrections are made to the measurements to compensate for the temperature dependence of the thermopile. Communication

is established via RS-485 with the Modbus RTU protocol. The SHP1 has an IP67 rating which makes it ideal for use without the need for a special enclosure to protect it from the elements. The SHP1 should be mounted on a sun tracker with a tracking accuracy of 0.5°, as specified in the Kipp & Zonen SHP1 Smart Pyrheliometer Instruction Manual [49].

Figure 3.2: Kipp & Zonen SHP1 Pyrheliometer.

3.3.1.2 Pyranometer

The Kipp & Zonen SMP10 pyranometer [50], shown in Figure 3.3, is used for wide FOV solar irradiance measurements, such as GHI measurements. It uses a 32-junction thermopile detector under a glass dome to measure irradiance in the spectral range of 285 nm to 2800 nm within a 180° field of view. Like the SHP1, it has temperature compensation, a 95% response time of under 2 seconds, IP67 rating and Spectrally Flat Class A ISO 9060:2018 classification. Communication is also established via RS-485 with the Modbus RTU protocol.

Figure 3.3: Kipp & Zonen SMP10 Pyrheliometer.

3.3.2 Spectral Irradiance Measurements

3.3.2.1 Narrow FOV Spectral Irradiance Meter

The Spectrafy SolarSIM-D2 [51], pictured in Figure 3.4, is used for narrow FOV spectral irradiance measurements. It employs multiple filtered photodiodes to take spectral measurements in certain narrow wavelength bands. These measurements are used in software to reconstruct the solar spectral irradiance. All measurements are made within a 5° viewing angle. Spectral irradiance is resolved in the range of 280 nm to 4000 nm with an RMS error of under 1.5% over 96% of the 350 nm - 1830 nm range. It is able to resolve atmospheric parameters such as aerosol optical depth with ± 0.005 AM to ±0.01 AM accuracy, atmospheric ozone with ±3% uncertainty and precipitable water vapor with uncertainty of less than 1 nm. In addition, it is able to determine broadband solar

irradiance with a response time of less than 0.5 seconds and is classified as Spectrally Flat Class A as per IS0 9060:2018. Communication is established via RS-485 ASCII using the included Spectrafy Combox shown in Figure 3.6. No official ingress protection rating is provided. However, this device is designed for outdoor use and no additional protection is required.

Figure 3.4: Spectrafy SolarSIM-D2 Spectral Irradiance Meter.

3.3.2.2 Wide FOV Spectral Irradiance Meter

The Spectrafy SolarSIM-G [52], shown in Figure 3.5, is used for wide FOV spectral irradiance measurements. Filtered photodiodes are used to take spectral measurements at multiple narrow wavelength bands. Software uses these measurements to reconstruct the spectral irradiance in the range of 280 nm to 4000 nm. Measurements are captured within a 180° FOV. The resolved spectrum has an RMS error of under 1.5% over 96% of the 350 nm - 1830 nm range. It also measures meteorological parameters such as ambient temperature, relative humidity and atmospheric pressure. Additionally, it is classified as Spectrally Flat Class A per IS0 9060:2018 and it can determine broadband solar irradiance within a response time of less than 0.7 seconds. This device communicates using RS-485 ASCII using the supplied Spectrafy Combox shown in Figure 3.6. It does not have an official ingress protection rating. However, it can be used without any protective equipment as it is designed for outdoor use.

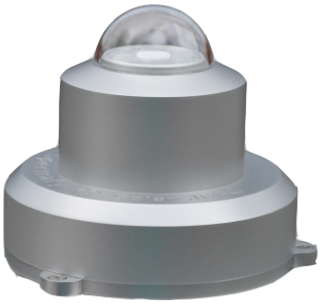

Figure 3.5: Spectrafy SolarSIM-G Spectral Irradiance Meter.

3.3.2.3 Spectrafy Combox

The Spectrafy Combox, shown in Figure 3.6, is supplied with each Spectrafy spectral irradiance meter. It acts as both a power converter and a communications converter enabling the user to power and connect the spectral irradiance meters to a device such as a PC.

Figure 3.6: Spectrafy Combox.

3.3.3 Image Capture

3.3.3.1 Camera

It is vital that the camera used to capture images of the sky has a sufficient ingress protection rating, as it will be used outdoors and exposed to the elements.

The first camera that is considered is the GoPro Hero7 Black [53] due to its reputation for being tough and durable. However, there are some significant drawbacks to using this camera. The GoPro Hero7 has a wide angle lens, allowing for a 122° viewing angle. This seems advantageous as a larger area of the sky can be covered with a single image. The trade-off to having this wide viewing angle is that the resultant image is often distorted. Many users, in the official GoPro support forum [54], report excessive lens flare when capturing images in bright sunlight. This is because it has a flat lens cover over its curved lens, making it more susceptible to lens flare. Another, more significant, drawback is the lack of USB camera control. Remote control and operation of the camera is necessary for this application.

The Sony RX0 [55], pictured in Figure 3.7, is another candidate camera as it has an IPX8 equivalent rating. It has a viewing angle of 84°, making it less susceptible to distortion while still being wide enough to capture an adequate view of the sky. It makes use of a ZEISS Tessar T* Lens to reduce distortion even further. It has a smaller f/4 aperture compared to the more common f/2.8 apertures usually found in cameras of this class. This is beneficial as it allows the image to have a higher depth of field, and the drawbacks of allowing less light onto the camera sensor are negligible as the camera will be pointed directly into the sun. The camera has an electronic shutter which is suitable, as a traditional shutter would wear out over time if a high number of photos are taken daily. Images can be captured at a maximum resolution of 15.36 megapixels in either RAW or JPEG format for highly detailed photographs. Notably, this camera can be controlled remotely via USB using Sony's Remote Camera Control software. Wireless control is available using the Sony Camera Remote API software development kit. Wired control via USB is available with the use of open-source libraries. This camera is selected as it meets the requirements for this project.

Figure 3.7: Sony RX0 Digital Camera.

3.3.3.2 Servo Motor

Although USB can be used to control the Sony RX0 remotely, it cannot be used to toggle the camera on or off. The ability to toggle the camera power remotely is necessary, because if the camera were to power off for any reason, the user would have to manually power it back on again. This would be impractical if the station is deployed in a remote area. The camera power could be toggled either using Bluetooth control, or by mechanically pressing the power button. The latter method is preferred, as it is not prone to connection or pairing issues that could arise while using Bluetooth.

The power button could be pressed by a device such as the Crouzet Miniature Electric Linear Actuator [56]. It is relatively small and light, weighing only 90 g, and operates at a 5.6 V input voltage. The displacement of the actuator can be very precisely controlled. The drawback of using this device is the high cost, and since the precision that is offered is not required, the cost cannot be justified.

An alternative method to press the power button on the camera is to use a low-cost servo motor. A suitable servo motor is the Pololu Power HD mini [57]. This servo offers maximum travel of approximately 180°. It is also small and light, weighing only 18 g. Its rated torque of 2.7 kg·cm is able to provide an actuation force of 8.8 N over its 3 cm long arm, which exceeds the 5 N of force required to press an average button. The servo position is controlled using Pulse Width Modulation (PWM).

The Pololu Power HD mini servo motor is pictured next to the Crouzet miniature electric linear actuator in Figure 3.8. The servo motor is the preferred device to toggle the camera power due to its low cost. Consequently, a mounting bracket is required to be designed and manufactured to place the servo motor in the correct position relative to the power button.

Figure 3.8: Servo Motor and Linear Actuator.

3.3.4 Solar Tracking Unit

The Kipp & Zonen SOLYS2 [58] is a popular choice as a sun tracker. It tracks the sun to within less than 0.1° and supports a maximum payload of 20 kg. The primary deterrent in using this tracker is the high cost.

An alternative is to use a heavy-duty pan/tilt unit, such as the HAINA MG-1022 [59] shown in Figure 3.9. These units are primarily used in CCTV surveillance systems but are suitable for this application if controlled appropriately. This unit claims to support a payload of up to 22 kg and have a positional accuracy of ±0.2°, which meets the requirements of the SHP1 pyrheliometer. Its IP66 rating makes it suitable for use outdoors where it is exposed to the elements. It communicates via RS-485 with the Pelco-P or Pelco-D protocol. The Mean Time Between Failure (MTBF) for this unit is listed at over 5000 hours, making this ideal for long term use. The unit is able to pan 360° continuously at a speed of up to 9° per second and has a tilt range of between -20° to 60° at a speed of up to 4° per second.

The tilt angle can be offset by 20° with a bracket. This will enable the tilt angle to range between 0° and 80° which is far more useful for this project as the unit will be able to go from perfectly horizontal (facing directly upwards) to almost entirely vertical (almost perpendicular to the floor) to see as much of the horizon as possible. The reduced tilt angle in comparison to the SOLYS2 is considered acceptable when the differences in cost and accessibility are accounted for.

Figure 3.9: Pan/Tilt Unit.

3.3.5 Controller

3.3.5.1 Raspberry Pi

The Raspberry Pi Model 3B [60], shown in Figure 3.10, is selected as the master device responsible for controlling all the devices in the system. It is also responsible for processing and storing all the captured data until it is transferred. The Raspberry Pi is the ideal controller for this application, owing mainly to its vast feature set. Its 64-bit quad-core processor is capable of easily executing any task that is required. A variety of connectivity options, including Ethernet, WiFi, Bluetooth, and USB, are available. A 40-pin GPIO header with access to dedicated Serial Peripheral Interface (SPI) and PWM

pins is also available. A notable feature that is not included is an onboard Real Time Clock (RTC).

The Raspberry Pi stores the captured data on its Micro SD memory card in cases where data is downloaded frequently and storage capacity is not a concern. In addition, the Raspberry Pi supports the use of external solid-state drives in instances where data cannot be downloaded as frequently, and large amounts of data must be stored.

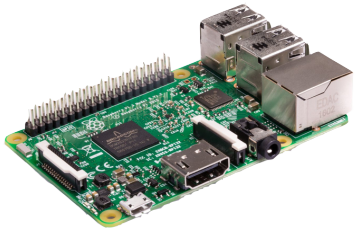

Figure 3.10: Raspberry Pi Model 3B.

3.3.5.2 Real-Time Clock

The RTC DS1302 SPI Module [61], pictured in Figure 3.11, is selected to maintain the correct time on the Raspberry Pi in the case of system reboots or power loss. The module easily interfaces with the Pi using SPI. It is small, affordable and power-efficient. Proper timekeeping is vital if the position of the sun in the sky is to be accurately calculated and the captured data is to be timestamped.

Figure 3.11: DS1302 RTC.

3.3.6 Network Router

The Raspberry Pi is placed in an aluminium enclosure which shields it from all external wireless signals. Therefore, a cable connection to a router is required to connect the Pi to the network. The D-Link DSL-G225 [62], shown in Figure 3.12, is used to connect the Raspberry Pi to the local network (or to the internet if required). Network connectivity is necessary if devices are to gain remote access to the Raspberry Pi to download the stored measurement data or debug the measurement station. This router includes a USB port with support for a 3G modem. This is useful if the station is deployed in a remote location with no wired internet available. The USB port can also be used for a shared storage

drive. This allows the Pi to save measurements on the shared storage drive instead if it is more convenient. The router features 2 SMA connectors on the back where removable WiFi antennas are attached. The SMA connectors allow for the antennas to be placed in any convenient location with the use of antenna extension cables.

Figure 3.12: D-Link Router.

3.3.7 Device Summary

The main functions performed by each device employed in the system are summarised in Table 3.1. Table 3.2 provides an overview of the physical characteristics of each device, as well as its interface and voltage requirements.

Table 3.1: Functions of Devices.

Device	**Function**
Kipp & Zonen SHP1	Measure Narrow FOV Irradiance
Kipp & Zonen SMP10	Measure Wide FOV Irradiance
Spectrafy SolarSIM-D2	Measure Narrow FOV Spectrum Measure Atmospheric Ozone Measure Aerosol Optical Depth Measure Precipitable Water Vapor
Spectrafy SolarSIM-G	Measure Wide FOV Spectrum Measure Humidity Measure Air Pressure Measure Temperature
Sony RX0	Capture Images Of Sky
Servo Motor	Toggle Camera On/Off
Pan/Tilt Unit	Orientate Instruments In Desired Direction
Raspberry Pi Model 3B	Control All Devices Log And Store Captured Data
DS1302 RTC	Update Time On Raspberry Pi
D-Link N300 Router	Connect Raspberry Pi To Network For Data Transfer And Debugging

Table 3.2: Device Overview

Device	Interface	Voltage	Weight	Dimensions (mm)
Raspberry Pi 3B	USB, Ethernet, WiFi, Bluetooth, GPIO, UART	5 V	45 g	56.5 × 85.6 × 17
DS1302 RTC	SPI	2 V - 5.5 V	4 g	15 × 31
Sony RX0	USB, WiFi	5 V	110 g	59 × 40.5 × 29.8
Servo Motor	PWM Input	4.5 V - 6 V	18 g	34.7 × 28 × 13.2
Kipp & Zonen SHP1	RS-485	5 V - 30 V	900 g	⌀ 76 × 322
Kipp & Zonen SMP10	RS-485	5 V - 30 V	600 g	⌀ 150 × 93
Spectrafy SolarSIM-G	RS-485	12 V	1.2 kg	⌀ 132 × 110
Spectrafy SolarSIM-D2	RS-485	12 V	1.2 kg	⌀ 132 × 108
Pan/Tilt Unit	RS-485	24 V - 28 V	10 kg	265 × 180 × 315
D-Link N300 Router	Ethernet, WiFi	12 V	294 g	255.9 × 168 × 41.2

3.4 Power Supply

3.4.1 Requirements

3.4.1.1 Power

The power requirements of each device are presented in Table 3.3. It is seen that power must be provided at 3 distinct voltage levels: 5 V, 12 V and 24 V. The required power requirements of each supply voltage are summarised in Table 3.4. It is seen that the vast majority of the required power is needed for the pan/tilt unit and the wireless router.

Table 3.3: Power Requirements per Device.

Device	Voltage	Current	Power
Raspberry Pi	5 V	500 mA	2.5 W
Sony RX0 Camera	5 V	260 mA	1.3 W
Servo Motor	5 V	200 mA (800 mA peak)	1 W (4 W peak)
Kipp & Zonen SHP1	12 V	4.5 mA	0.054 W
Kipp & Zonen SMP10	12 V	4.5 mA	0.054 W
Spectrafy SolarSIM-G	12 V	<83 mA	<1 W
Spectrafy SolarSIM-D2	12 V	<83 mA	<1 W
D-Link N300 Router	12 V	1000 mA	12 W
Pan/Tilt Unit	24 V	1667 mA	40 W

Table 3.4: Requirements as per Supply Voltage.

Supply Voltage	Required Current	Required Power
5 V	1.560 A	7.8 W
12 V	1.175 A	14.1 W
24 V	1.667 A	40 W
		62.4 W

3.4.1.2 Energy

The daily energy requirements are separated into 2 parts of 12 hours each - daytime requirements when the system operates and collects data, and nighttime requirements when the system is inactive. The daytime and nighttime requirements are added together to determine the total energy required by the system per day.

Day time requirements:

Most of the power required by the system is used to operate the pan/tilt unit. It is seen from Table 3.3 that the unit requires 40 W of power during operation at maximum speed and at full payload. The unit does not operate continuously in this application. The plan is for it to only work for 3 minutes of a 10-minute measurement sequence. The result is that the unit operates at an effective duty cycle of 30% during planned operation. The duty cycle is assumed to be 50% as a conservative estimate, resulting in an average power requirement of 20 W for the pan/tilt unit. The energy required by the servo motor is neglected as it is planned to only operate once in the morning for a few seconds to power the camera on. All other devices are assumed to operate at maximum power.
The average power and the energy required by the system during daytime operation is shown in Table 3.5 with the aforementioned assumptions accounted for.

Table 3.5: Average Power and Energy Requirements During the Day.

Power Supply	**Average Power**	**Energy Over 12 Hours**
5 V	3.8 W	45.6 Wh
12 V	14.1 W	169.2 Wh
24 V	20 W	240 Wh
	37.9 W	**454.8 Wh**

Night time requirements:

The energy requirements of the servo motor are neglected as it only operates once in the night for a few seconds to power the camera off. The pan/tilt unit and camera do not operate at night and are assumed to draw no power. All other devices are assumed to operate with maximum power consumption for a conservative estimate. In reality, the Raspberry Pi draws very little power as it is idling, and the router does not draw full power as very little data transfer occurs. The Raspberry Pi cannot be switched off overnight as it is the master device and must always be available on the network. The router is always powered on to maintain network connectivity. The average power and the energy required by the system during nighttime operation is shown in Table 3.6 as per the assumptions made.

Table 3.6: Average Power and Energy Requirements During the Night.

Power Supply	Average Power	Energy Over 12 Hours
5 V	2.5 W	30 Wh
12 V	14.1 W	169.2 Wh
24 V	0 W	0 Wh
	16.6 W	**199.2 Wh**

With all of the above information taken into account, the total energy required by the system over a 24 hour period is determined to be **654 Wh**.

3.4.2 Part Selection

3.4.2.1 Solar Panel

The Western Cape province receives a daily average of between 4.7 - 6.0 peak sun hours [63].

As per the requirements outlined in Chapter 3.2, the system is to be solar-powered. This enables the system to be deployed in remote locations where alternative power sources are not readily available. As determined in the previous section, the energy requirement of the system is 654 Wh per day. The minimum power that the solar panel must provide to the system is determined as follows:

$$\begin{aligned} PV\ wattage &= \frac{daily\ energy\ required}{daily\ sun\ hours \times 75\%} \\ &= \frac{654\ Wh}{4.7\ h \times 75\%} = 185.5\ W \end{aligned} \tag{3.1}$$

The factor of 75% is included in equation (3.1) to account for any losses in the system for a more conservative estimate. It is determined that a PV panel with at least a 185.5 W rating is required to supply the system with power.

3.4.2.2 Batteries

To meet the power requirements as outlined in section 3.4.1, it is decided that 2 series-connected 12 V batteries will power the station as a whole. These batteries will directly power the pan/tilt unit and act as a power source for the required 5 V and 12 V supplies that power the remaining devices. The maximum current drawn from these batteries is 2.6 A if the system operates at its full power of 62.4 W.

In the event that the solar panel cannot provide power to the system, the batteries are required to be able to provide power for at least 24 hours with a maximum depth of discharge of 30%. The battery capacity needed to meet this requirement is determined as follows:

$$Capacity = \frac{energy\ required}{depth\ of\ discharge \times voltage} \times derating\ factor$$
$$= \frac{654\ Wh}{30\% \times 24\ V} \times 1.13 = 102.64\ Ah \tag{3.2}$$

The derating factor is included in equation (3.2) to account for the decrease of the capacity of a battery with a reduction in temperature. The lowest average monthly temperature in Stellenbosch is 10.9°C [64]. The derating factor is selected as 1.13 to account for the effect of temperature on the battery capacity [65]. The 24 V battery pack for the system will consist of 2 series-connected 12 V batteries, each with a capacity of 102 Ah.

3.4.2.3 MPPT Charge Controller

A Maximum Power Point Tracker (MPPT) Charge Controller is used to charge the batteries from the solar panel at maximum available power. The Microcare 40 Amp MPPT Charge Controller [66], shown in Figure 3.13, is available for use in this project. It is able to charge battery sets at voltages from 12 V to 48 V at a current of up to 40 A with over 96% efficiency. The float voltage is specified at 13.8 V per battery. For the required 24 V mode, the batteries are charged at 27.6 V. It is suitable for continuous 24-hour operation and supports PV arrays with a maximum open-circuit voltage of 150 V. This MPPT is well within the requirements of this project.

Figure 3.13: Microcare MPPT.

3.4.2.4 Electrical Enclosure

An IP65 electrical enclosure, pictured in Figure 3.14, is used to house the Microcare MPPT Charge Controller, batteries, D-Link Router and external 12 V power supply. It will protect the equipment from the elements. This enclosure is made from metal and, as a result, blocks the signal from the wireless router. Consequently, antennas are connected to the router and mounted externally on the enclosure to overcome this issue.

Figure 3.14: Electrical Enclosure.

3.4.2.5 5 V Supply

It is seen in Table 3.3 that the servo motor operates at 5 V, with an average current of 200 mA. However, during startup, the servo motor may draw up to 800 mA. This sudden spike in current demand could lead to a temporary voltage drop at the output of the power supply. This may affect the operation of essential devices - such as the Raspberry Pi. The voltage ripple may be reduced by adding sufficient capacitance at the output of the power supply. However, it is decided that the alternative approach of adding a second 5 V power supply is preferable. In this approach, all essential devices with a relatively steady current draw are connected to one 5 V supply, and non-essential devices such as servo motor and potential future devices are connected to a second 5 V supply. The advantage of this approach is that each power supply will operate at a reduced load. The power supply for the essential devices would only need to provide 760 mA of current, and the second power supply would be required to provide the remaining 800 mA. This allows future devices to be added as necessary and provides a stable output voltage for the essential devices.

The LT8610 synchronous step-down regulator [67] is used to design a 5 V step-down converter shown in Figure 3.15. The PCB design and layout was done by Dr J.M. Strauss. The full schematic, PCB layout and component values used are shown in Appendix A.1.

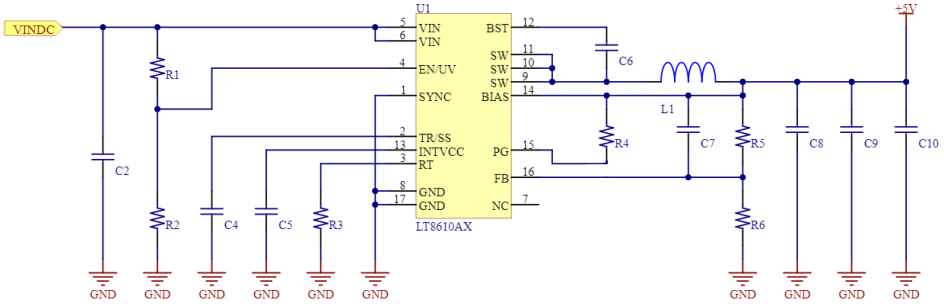

Figure 3.15: Suggested LT8610 circuit layout as per datasheet [67]

The circuit is designed to supply an output voltage of 5 V from an input voltage in the range of 11 V to 24 V. The output voltage is set according to equation (3.3), as per the datasheet [67, p.12].

$$V_{out} = (0.97)\left(\frac{R5}{R6} + 1\right) = (0.97)\left(\frac{1M}{191k} + 1\right) = 5.08\ V \tag{3.3}$$

The minimum input voltage of 11 V is set according to equation (3.4) [67, p.15].

$$V_{IN(EN)} = (1\ V)\left(\frac{R1}{R2} + 1\right) = (1\ V)\left(\frac{220k}{22k} + 1\right) = 11\ V \tag{3.4}$$

Resistor R3 is selected to be 68 kΩ which sets the switching frequency to 0.635 MHz. The values of all other components selected are shown in Appendix A.1.

The circuit was built and tested. The output current is measured to be 2.47 A when the circuit is under full load. This far exceeds the required 760 mA and 800 mA of each respective 5 V supply.

3.4.2.6 12 V Supply

Two 12 V power supplies are required in this project. One 12 V power supply providing 1 A is needed to power the D-Link Router in the IP65 electrical enclosure, and another providing 175 mA is required to supply power to the instruments on the measurement station.

The LTC3115 synchronous buck-boost DC/DC converter [68] is used in the design of a 12 V step-down converter shown in Figure 3.16. The PCB design and layout was done by Dr J.M. Strauss. The full schematic, PCB layout and component values used are shown in Appendix A.2.

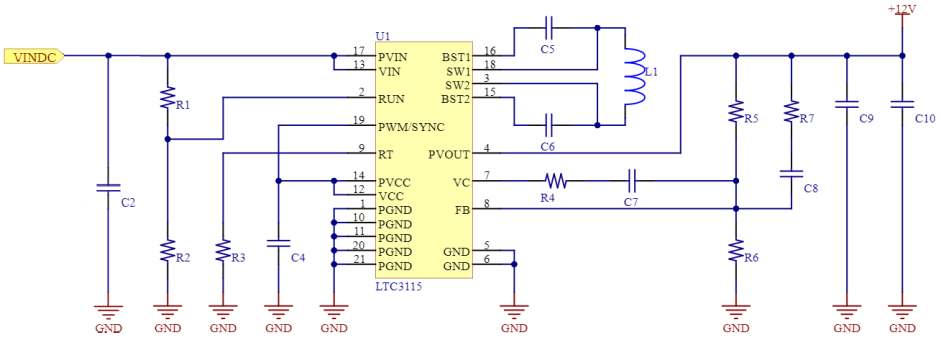

Figure 3.16: Suggested LTC3115 circuit layout as per datasheet [68]

The circuit was built and tested. The output current at maximum load was measured to be 1.4 A. This exceeds the requirement of 1 A and 175 mA of each of the two power supplies that are needed.

3.5 Hardware Integration

The diagram shown in Figure 3.17 provides an overview of how the devices in the system interface with each other regarding communication. The Raspberry Pi is the master device and must communicate with every other device in the system. The D-Link router enables external devices such as PCs that are not part of the system to communicate with the Raspberry Pi over the local network.

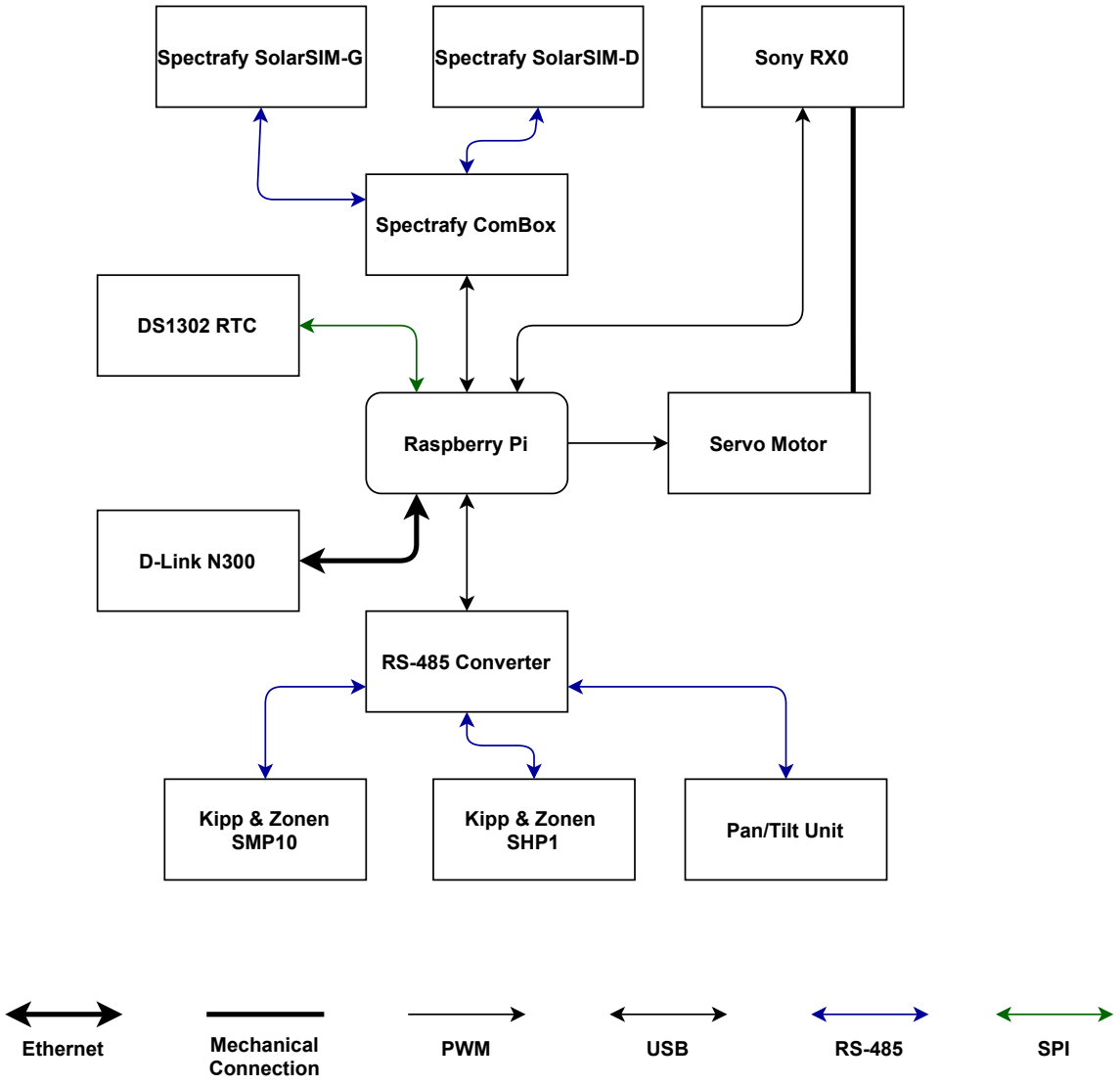

Figure 3.17: Device Integration - Communication.

Figure 3.18 provides an overview as to how power is distributed in the system. The solar panel provides power to the MPPT, which charges two series-connected 12 V batteries. These batteries directly power the pan/tilt unit and act as a source for both the 12 V and the 5 V supplies. These supplies then power all the relevant devices.

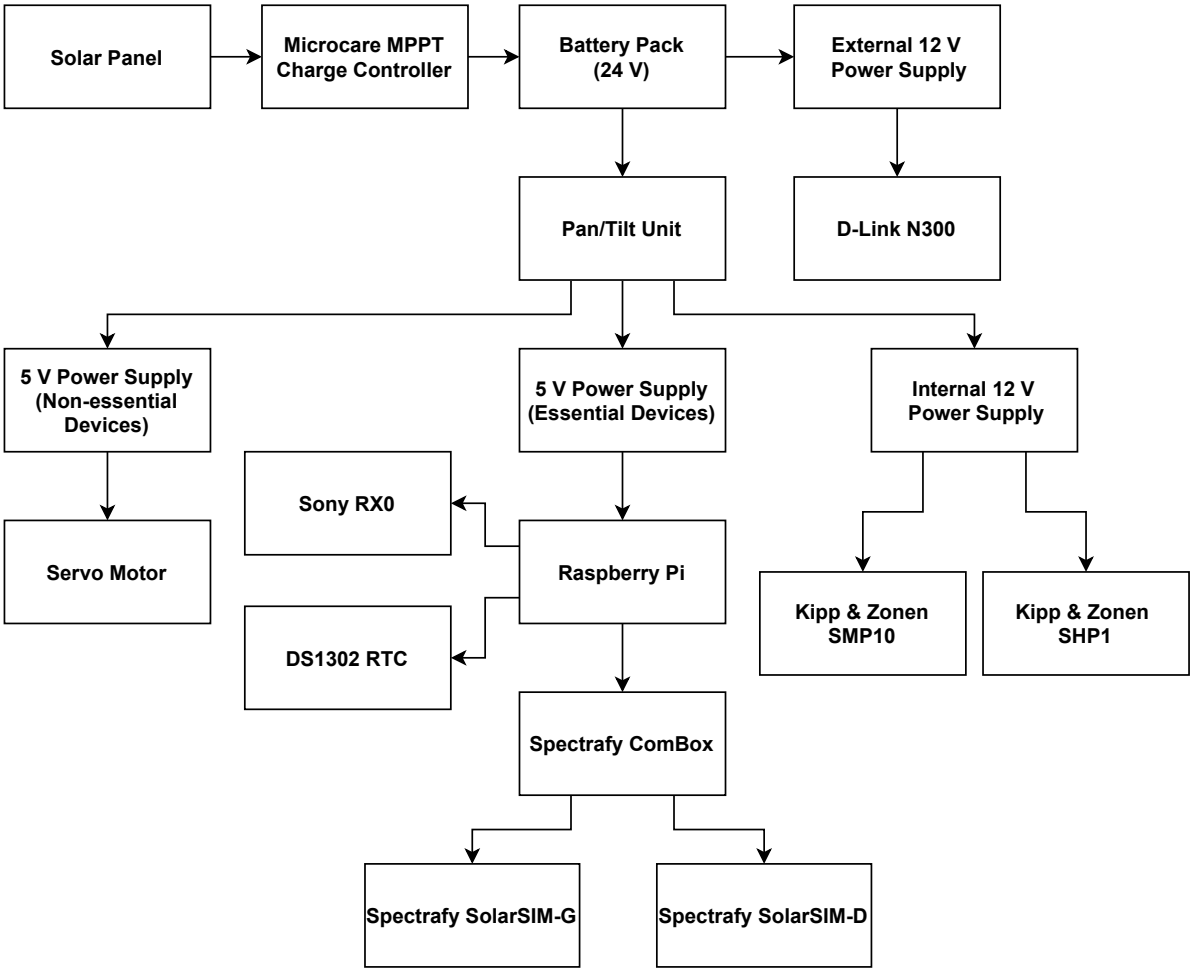

Figure 3.18: Device Integration - Power Connections.

3.6 Measurement Station Design

This section provides an overview of the design of important elements used in the assembly of the measurement station. The full CAD schematics of each element designed are shown in Appendix B.

3.6.1 Enclosure Assembly

The overall design of the enclosure and the layout of the mounted devices is shown in Figure 3.19. The devices are mounted on the enclosure in such a way that the weight is as evenly distributed as possible. Detailed schematics of the parts and brackets that are designed are available in Appendix B.

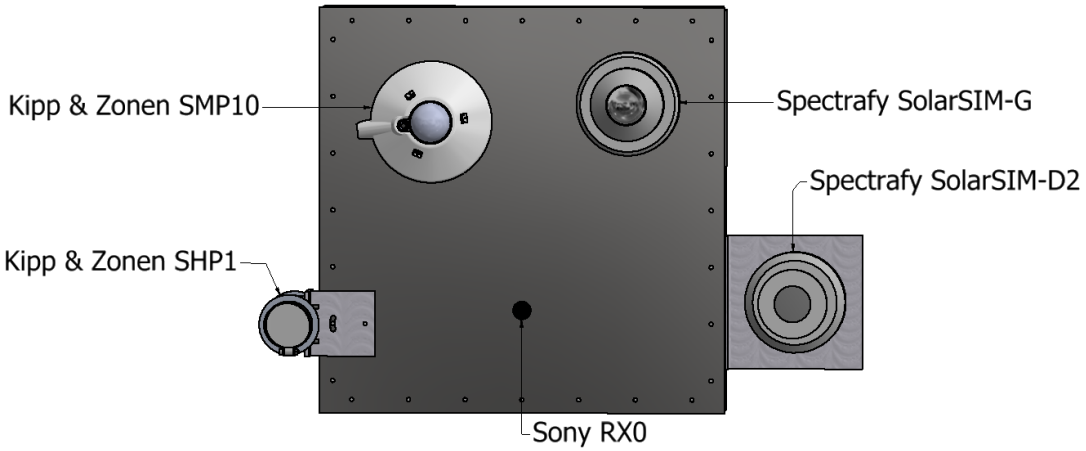

Figure 3.19: Enclosure Assembly.

3.6.2 Enclosure

An enclosure is designed to house and protect the power supplies, controller, and camera and provide a surface on which the instruments are mounted. The enclosure design is shown in Figure 3.20. The back cover is made using a 2 mm thick aluminium sheet, which is folded and welded. The front platform is made with a 3 mm thick aluminium sheet.

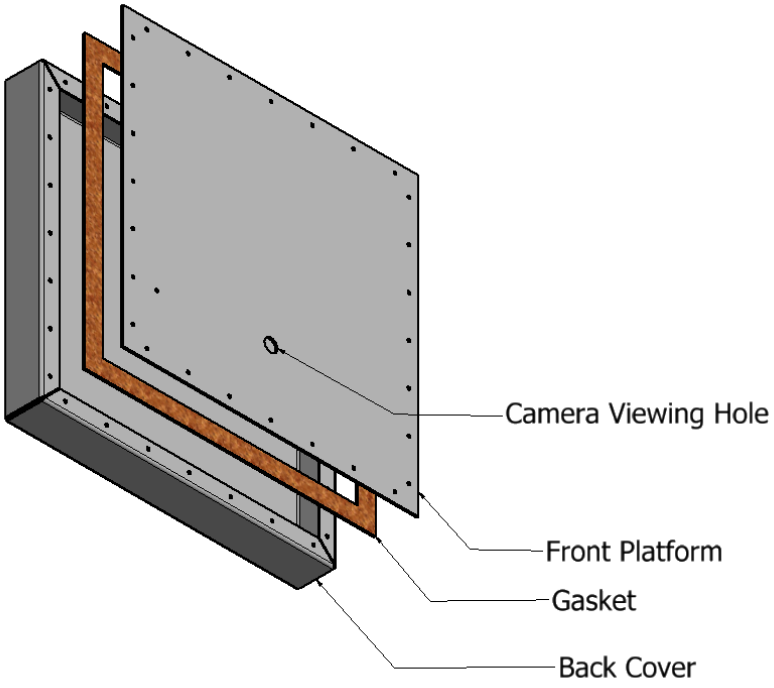

Figure 3.20: Enclosure Design.

Aluminium is used as it is light, corrosion-resistant and cost-effective. A gasket is placed between the back cover and the front platform for increased weather-resistance.

Cable glands are used for all cables going into the enclosure to maintain weather-resistance.

The enclosure measures 500 mm × 500mm × 64 mm. These dimensions are selected to be able to comfortably house all the required instruments and devices, while also allowing for enough room to add more equipment if it should be required in the future. It weighs approximately 4.5 kg, as shown in Table 3.7.

Table 3.7: Enclosure Overview.

	Aluminium		
	Thickness	**Surface Area**	**Weight**
Front Lid	3 mm	0.25 m^2	2.08 kg
Back Cover	2 mm	0.4331 m^2	2.4 kg
			4.48 kg

3.6.3 Servo Motor and Camera Mounting Bracket

The camera is to be used for long periods, and consequently, power must be constantly supplied by removing the back panel of the camera to plug in the power cable. Removing this back panel compromises the IPX8 rating of the camera. The camera should be housed inside an enclosure to protect it from the elements, with only the lens being left exposed and unobstructed to capture clear images. The camera lens is not covered by any transparent material so that the image quality is preserved.

Figure 3.21 shows the mounting bracket that is designed to hold the camera and servo motor in place inside the enclosure. The mounting bracket is 3D printed. Using 3D printing is suitable as it allows the bracket to be manufactured quickly and at a low cost. The material used to print the bracket is PLA, which has a glass transition temperature of between 50°C - 80°C depending on the quality. The expected temperature inside the enclosure is between 55°C - 60°C, therefore, using a high quality PLA filament for printing should be suitable. However, if any issues are detected with the PLA bracket, it can be easily reprinted using ABS which has a glass transition temperature of 105°C.

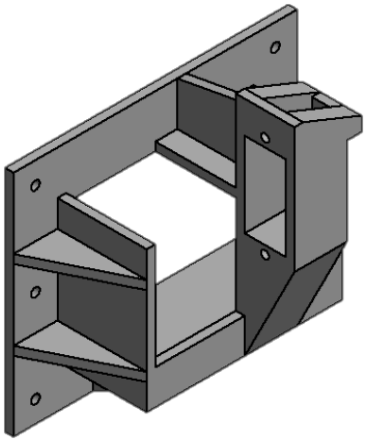

Figure 3.21: Servo Motor and Camera Mounting Bracket.

The assembly of the mounting bracket, camera, gasket and platform lid is shown in Figure 3.22.

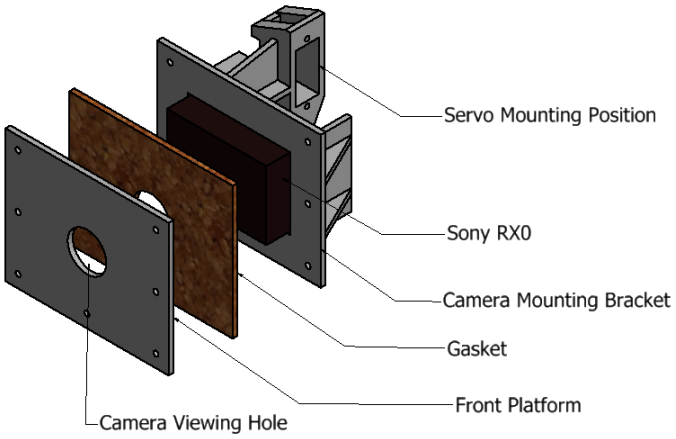

Figure 3.22: Assembly of Mounting Bracket.

3.7 Torque Balancing

The pan/tilt unit was observed to have difficulty in lifting the enclosure and all the instruments. This is despite the fact that the unit is specified to support a payload of up to 22 kg while the overall weight of the enclosure, with all fittings and instruments included, is measured to be 16.8 kg. This section discusses the calculations used to determine the requirements for a spring that can be used to reduce the overall torque on the pan/tilt unit to improve its performance.

The force diagram of the system, with all relevant information, is shown in Figure 3.23.

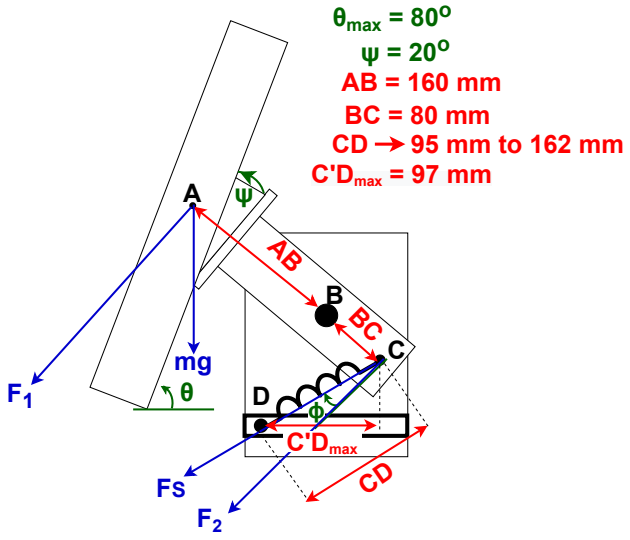

Figure 3.23: Measurement Station Force Diagram.

The information presented in Figure 3.23 is used to plot torque as a function of tilt angle shown in Figure 3.24. It is seen that the torque is at the highest value when the pan/tilt unit is at its most extreme tilt angle of 80°.

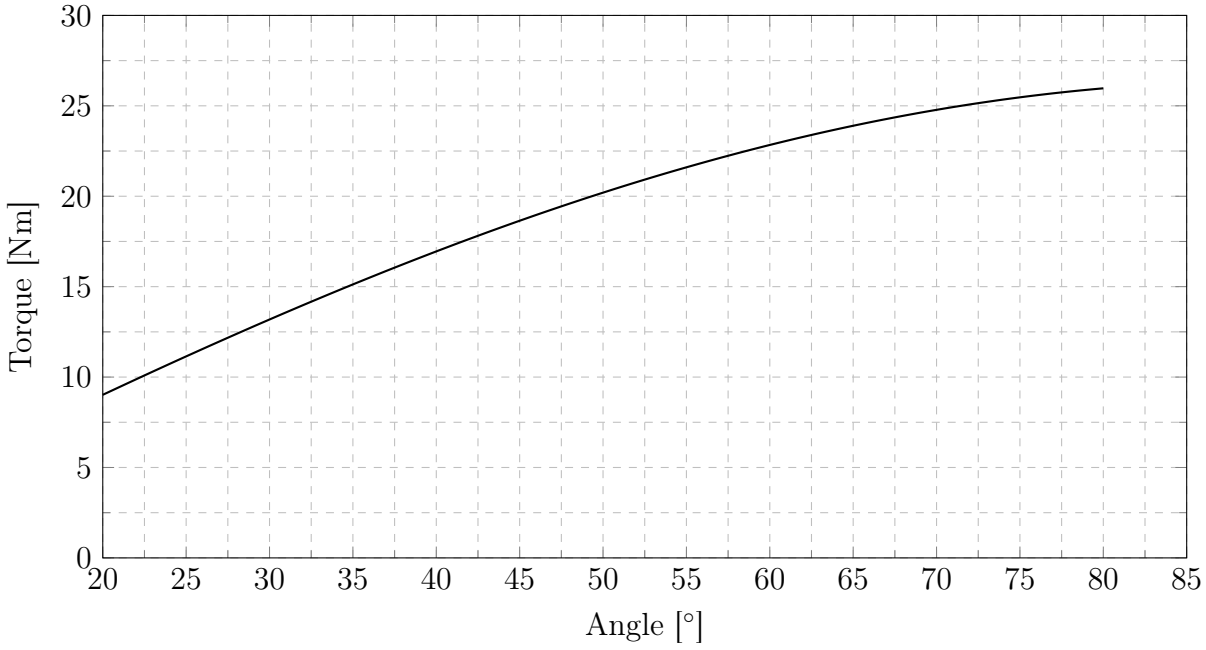

Figure 3.24: Torque as a function of Tilt Angle.

The spring stiffness coefficient of the spring needed to cancel out the torque in this position is determined, with reference to the force diagram shown in Figure 3.23, as follows:

The component of the force in the direction perpendicular to length AB is determined using equation (3.5), where m is the mass of 16.8 kg, g is the gravitational acceleration constant of 9.81 m/s^2, and Θ is the maximum tilt angle of 80°. This component is responsible for creating the torque around pivot point B.

$$F_1 = m \cdot g \cdot \sin\theta = (16.8)(9.81)\sin 80 = 162.3\ N \tag{3.5}$$

The resultant torque around pivot point B is determined using equation (3.6).

$$T_1 = F_1 \cdot AB = (162.3)(0.16) = 25.97\ N \cdot m \tag{3.6}$$

In order to cancel this resultant torque, a counter torque of the same magnitude is required.

$$T_1 = T_2 = 25.97\ N \cdot m \tag{3.7}$$

The force required to generate this counter-torque about pivot point B over a perpendicular distance BC is determined using equation (3.8).

$$F_2 = \frac{T_2}{BC} = \frac{25.97}{0.08} = 324.61\ N \tag{3.8}$$

The force exerted by the spring is not perfectly perpendicular to distance BC. Therefore, the offset angle from perpendicular is calculated using equation (3.9).

$$\phi = 60 - \arccos(\frac{97}{162}) = 6.8° \tag{3.9}$$

The force required to be generated from the spring in order to provide the required component of force perpendicular to BC is determined in equation (3.10).

$$F_S = \frac{F_2}{\cos\phi} = \frac{324.61}{\cos 6.8} = 326.91\ N \tag{3.10}$$

Equation (3.11), presented by Hibbeler and Yap [69, p.86], is used to determine that a spring stiffness coefficient of 4.88 N/mm is required to provide the necessary counter-torque.

$$k = \frac{F_S}{l - l_0} = \frac{326.91}{162 - 95} = 4.88\ N/mm \tag{3.11}$$

Figure 3.25 presents the resultant torque curves if springs with various stiffness coefficients are implemented. It is seen that the resultant torque is reduced over the entire range of tilt angles. Even the use of a spring that does not perfectly cancel out the applied torque greatly reduces the overall torque, and is better than using no spring at all.

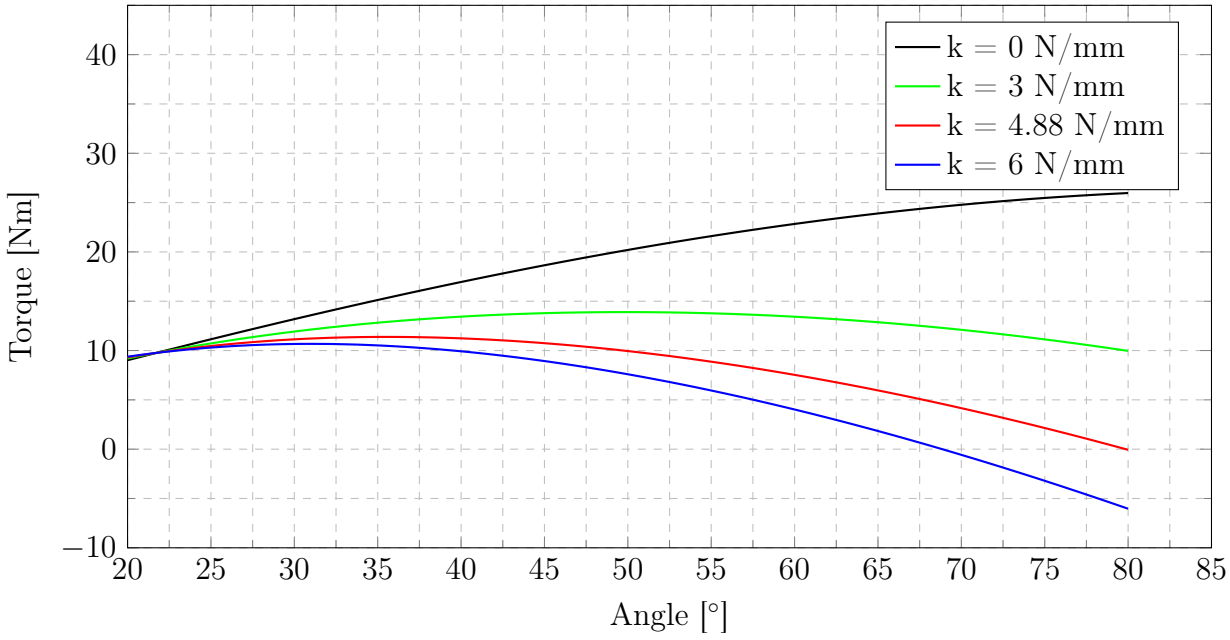

Figure 3.25: Torque Curve at Different Spring Stiffness.

A spring with the exact spring stiffness coefficient is not manufactured, as only a single spring is needed. The spring manufacturers require a bulk order to perform a production run for the required spring. The stiffness coefficient of the spring that is actually used is measured to be approximately 5.5 N/mm. The spring is implemented, as shown in Figure 3.26, to reduce the effective load applied to the pan/tilt unit by applying a counter-torque. This is suitable and significantly improves performance.

Figure 3.26: Spring used to create counter-torque.

3.8 Chapter Review

The design of the system and the integration of all its components was discussed in this chapter. The system requirements and design considerations were stated and motivated based on the information presented in Chapters 1.2, 2.5 and 2.6. The instruments used to gather data include a pyrheliometer, a pyranometer, a narrow FOV spectral irradiance meter, a wide FOV spectral irradiance meter and a digital camera. The instruments are controlled by a Raspberry Pi, which interfaces to external devices through a network connection provided by a router. The instruments are mounted on top of and inside an aluminium enclosure which is designed to be weather resistant. The enclosure is mounted on a pan/tilt unit to orientate the instruments in the desired direction. A spring is implemented to counter the torque caused by the weight of the enclosure and instruments on the pan/tilt unit to improve its performance. The system receives power from a 24 V battery pack charged using an MPPT connected to a PV panel. The software responsible for the control of the system is discussed in Chapter 4.

Chapter 4

Software

4.1 Introduction

This chapter explores the design of the control software of the measurement station. The protocols used are briefly discussed, and insight into the practical implementation and reasoning behind important decisions is provided. Several important functions that are used are listed at the end of each section.

A Raspberry Pi is used to control the operation of the various devices on the measurement station. The Raspberry Pi used in this project runs on the Linux based Raspbian operating system. This operating system is selected as it is the official operating system for the Raspberry Pi. Other operating systems, such as Ubuntu Mate, were considered. However, the lack of support available in comparison to Raspbian was the main deterrent. All the software in this project is written in Python as it runs natively on the Raspberry Pi. The instruments connected to the Raspberry Pi include a Kipp & Zonen SHP1 pyrheliometer, a Kipp & Zonen SMP10 pyranometer, a Spectrafy SolarSIM-D2 spectral irradiance meter, a Spectrafy SolarSIM-G spectral irradiance meter and a digital camera. The Kipp & Zonen SHP1 pyrheliometer and SMP10 pyranometer are used to gather narrow FOV and wide FOV broadband irradiance, respectively. A USB to RS-485 converter is used to connect these devices to the Raspberry Pi. The Modbus RTU protocol is used for communication. The Spectrafy spectral irradiance meters are used to gather atmospheric data and spectral irradiance measurements. They connect to the Raspberry Pi via USB through the supplied Spectrafy ComBox. The RS-485 ASCII protocol is used for communication. The digital camera is connected to the Raspberry Pi via USB. However, the camera can not be powered on or off using software commands. Therefore, a servo motor is used to physically toggle the power button on the camera. This servo motor is controlled using PWM and is connected to the PWM pin on the Raspberry Pi. A pan/tilt unit is used to orientate the instruments on the measurement station in the desired direction. It uses the same USB to RS-485 converter as the Kipp & Zonen instruments to connect to the Raspberry Pi. Since the pan/tilt unit is designed originally for use with camera surveillance systems, the Pelco-D protocol is used for communication. Pelco-D is an industry-standard protocol used to control PTZ (pan tilt zoom) cameras.

4.2 Modbus Protocol

The Kipp & Zonen SHP1 pyrheliometer and SMP10 pyranometer both transmit data over RS-485 using the Modbus RTU protocol.

4.2.1 Protocol Overview

Modbus is a master/slave serial communication protocol. A single master device is used to control multiple slave devices on the same serial bus, where each slave is assigned a unique address. The master requests to either read data from or write data to the registers of a specific slave. Only the slave with the specified address responds to the request. The master can control up to 247 slaves, with addresses ranging from 1 - 247. Address 0 is the broadcast address and addresses 248 - 255 are reserved. The slave devices on the serial bus do not communicate with each other, as only communication between the master and a slave is permitted. The master always initiates communication, and the slave may only respond. The master may communicate with only a single slave at any given time. [70]

The format and framing of a Modbus message is shown in Figure 4.1. The message frame begins and ends with a silent interval of at least 28 bits (3.5 chars) [70]. This dead time is in place to allow the receiving device to discern distinct Modbus messages. The value of N is in the range of 0 - 252.

	Modbus message				
Start	**Address**	**Function**	**Data**	**CRC**	**End**
$\geq$ 28 bits	8 bits	8 bits	N $\times$ 8 bits	16 bits	$\geq$ 28 bits

Figure 4.1: Modbus Message Frame

The Modbus message contains the unique slave address, the function command, the data and the CRC (Cyclic redundancy check).

As previously stated, all slave devices on the serial bus receive every request sent by the master. Therefore, the slave address is included to ensure that only the appropriate slave responds. The function byte in the Modbus message determines what command the slave device should execute. These commands include reading data from or writing data to specific registers. Table 4.1 lists a few commonly used commands and their description that are used for all Modbus RTU devices [71]. The two CRC bytes are included at the end of the message to ensure that the received data has not been corrupted. The CRC is initially calculated by the transmitting device using every byte in the message. The calculated CRC is added to the end of the message and the message transmitted. The receiving device receives the message, calculates the CRC and compares it to the received value [70]. If the received CRC does not match the calculated CRC, the message has been corrupted and is discarded.

Table 4.1: Modbus Commands [71].

Command	Description
0x01	Read Coil Status
0x02	Read Input Status
0x03	Read Holding Registers
0x04	Read Input Registers

The flow diagram used to determine the CRC is shown in Figure 4.2, as presented in the Modbus Specification and Implementation Guide [70].

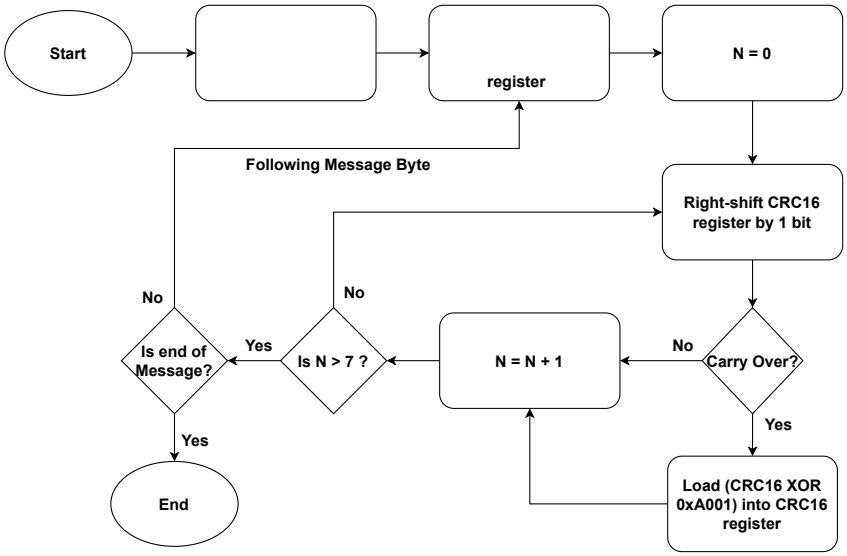

Figure 4.2: Calculation of CRC16, as Presented in the Modbus Specification and Implementation Guide [70].

4.2.2 Implementation

The UART of the Raspberry Pi is set up according to the information presented in Table 4.2 in order to communicate with the Kipp & Zonen devices. The Modbus addresses of the Kipp & Zonen devices are also shown.

Table 4.2: Kipp & Zonen Communication Configuration.

Parameter	Value
Baud rate	9600
Parity	None
Data bits	8
Stop bits	1
SMP10 address	0x02
SHP1 address	0x05

The implementation of a Modbus request to the Kipp & Zonen SHP1 and the description of the transmitted bytes is illustrated by the example in Table 4.3.

Table 4.3: Modbus Request - Sent Bytes.

Device Addr.	**Command**	**Start Reg.**		**No. of Reg.**		**CRC**	
byte 1	byte 2	byte 3	byte 4	byte 5	byte 6	byte 7	byte 8
0x05	0x04	0x00	0x00	0x00	0x0A	0x71	0x89
MSB	MSB	MSB	LSB	MSB	LSB	LSB	MSB

In this message, the address of the queried device is 0x05. It is seen in Table 4.2 that this address belongs to the SHP1 pyrheliometer. The command byte, 0x04, is a request to read the input registers of the device, as shown in Table 4.1. The first register from which data is to be read has the address 0x00. It is specified that the number of registers to be read is 0x0A. Consequently, 10 registers will be sequentially read starting at address 0x00 and ending at address 0x09. The least significant and most significant CRC bytes for this message are 0x71 and 0x89, respectively. It is important to note that the MSB is always transmitted first in this message, except in the case of the CRC bytes where the LSB is sent first.

A description of the information found at the address of each Kipp & Zonen input register is shown in Table 4.4 [50, p.41].

Table 4.4: Kipp & Zonen Input Registers.

Address	**Parameter**
0x00	Device Type
0x01	Data Model Version
0x02	Operational Mode
0x03	Status Flags
0x04	Scale Factor
0x05	Sensor 1 Data
0x06	Raw Sensor 1 Data
0x07	Standard Deviation of Sensor 1
0x08	Device Body Temperature
0x09	Device Voltage Sensor

The description of the received message bytes after a request, as described in Table 4.3, is shown in Table 4.5.

Table 4.5: Description of Received Bytes.

Modbus Addr.	Command	No. of Rec. Bytes	Data in Registers	CRC	
byte 1	byte 2	byte 3	byte 4 ... byte 23	byte 24	byte 25

In the Modbus protocol, the 1st and 2nd bytes are the address and command bytes, respectively. The 3rd byte describes how many data bytes are contained in the received message. The values contained in the input registers are included from byte 4 to byte 23, with the MSB transmitted before the LSB. A more detailed description of the type of data contained in each received data byte is shown in Table 4.6. The CRC is included in bytes 24 and 25, with the LSB being transmitted first.

Table 4.6: Description of Data in Registers.

Data in Registers										
byte 4	byte 5	byte 6	byte 7	byte 8	byte 9	byte 10	byte 11	byte 12	byte 13	byte 14
Device Type		Data Model Version		Operational Mode		Status Flags		Scale Factor		Sensor
byte 15	byte 16	byte 17	byte 18	byte 19	byte 20	byte 21		byte 22	byte 23	
1 Data	Raw Sensor 1 Data		σ Sensor 1 Data		Device Body Temperature			Device Input Voltage		

A flowchart describing the process by which data is retrieved from the Kipp & Zonen instruments is shown in Figure 4.3. Serial communication on the Raspberry Pi is set up and configured according to the information shown in Table 4.2 to enable communication with the Kipp & Zonen devices. A check to determine the connection status of the desired device is performed, and a connection error is raised if the device cannot be reached. If the device is connected, a message is constructed as described above. The CRC bytes for the message are calculated and appended to the message in little-endian format, and the message is transmitted. The contents of the message received in response to the request are processed. The data in the received message is in packed binary format, so the data is unpacked and formatted before it is used. The CRC of the message is calculated and compared to the received CRC. The desired data is written to a .csv file if the CRCs match. A CRC error is raised if the CRCs differ. A timeout error is raised if no response message is received.

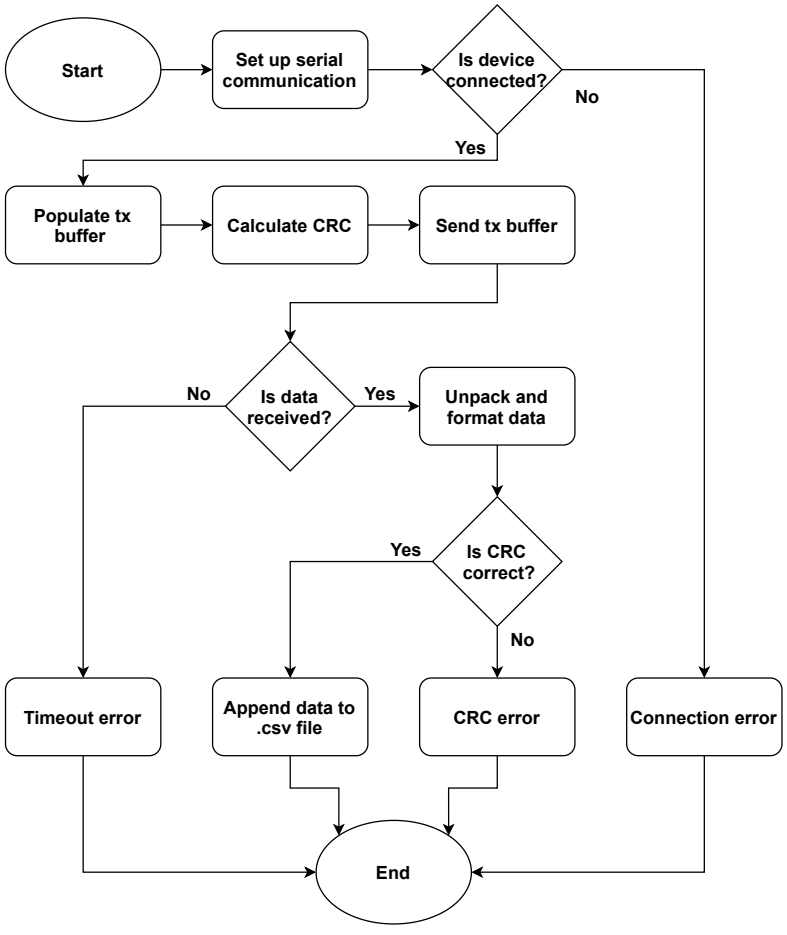

Figure 4.3: Kipp & Zonen Data Request.

4.2.3 Description of Functions

This section briefly describes a few of the important functions used to retrieve data from the Kipp & Zonen devices.

dev_connected(): Checks whether or not the specified Modbus device is connected. Returns **True** if the device is detected, or **False** if it is not.

crc16(): Calculates the CRC of the input Modbus message. Returns the calculated CRC.

checkCRC(): Compares the received CRC to the calculated CRC. Returns **True** if the CRCs match or **False** if they do not.

getSensorData(): Reads, unpacks and formats sensor data from a single Kipp & Zonen device. Returns the measured irradiance in W/m^2 in integer form.

getData(): Reads all available data from a single Kipp & Zonen device's registers. Unpacks, formats, timestamps, and appends all data to a .csv file in the specified directory.

getAllData(): Reads sensor data and temperature from both Kipp & Zonen devices. Unpacks, formats and timestamps data. Appends the data and corresponding solar azimuth and elevation angles to a .csv file in the specified directory. The format of the data written to the .csv file is shown in Figure 4.4.

Date	Time	GHI	DNI	Temperature	Azimuth	Elevation
02/08/2021	09:14:05	568	534	16.3	50.7	19
02/08/2021	09:23:52	586	574	17.55	48.9	20.6
02/08/2021	09:33:51	601	590	18.9	47.1	22.2

Figure 4.4: Format of .csv file.

The GHI, DNI and Temperature values populated in the .csv file are recorded by the Kipp & Zonen devices. The solar azimuth and elevation angles shown are calculated by the Raspberry Pi.

4.3 Pelco-D Protocol

The selected pan/tilt unit communicates over RS-485 using the Pelco-D protocol. It interfaces with the Raspberry Pi on the same serial bus as the Kipp & Zonen instruments. This is possible because each of these slave devices only respond to requests explicitly made to them. The communication protocols implemented eliminate the possibility of any miscommunication.

4.3.1 Protocol Overview

Pelco-D is a master/slave serial communication protocol used in the control of PTZ (pan tilt zoom) cameras. It allows one master to control up to 255 slaves connected on the same serial bus. Each slave is assigned a unique address ranging from 1 - 255. The

master always initiates communication, and only the slave with the appropriate address responds to the request. No communication between slave devices may occur. [72, p.8]

The format and framing of a Pelco-D command message is shown in Figure 4.5. The first byte of the command message is the synchronization byte. It indicates the start of the command message to the receiver. In the Pelco-D protocol, the value of the synchronization byte is always set to 0xFF [72, p.10]. The next byte contains the address of the device that the command is intended for. The instructions regarding which command must be executed are included in bytes 3 and 4, followed by additional information on how to execute the command in bytes 5 and 6. The last byte is the checksum. It is calculated by executing the 8-bit modulo 256 sum from byte 2 to byte 6 of the message [72, p.10]. The checksum is verified by the receiving device to ensure no data loss has occurred.

Pelco-D message						
Sync.	**Address**	**Command 1**	**Command 2**	**Data 1**	**Data 2**	**Checksum**
byte 1	byte 2	byte 3	byte 4	byte 5	byte 6	byte 7

Figure 4.5: Pelco-D Command Message Frame.

The command bytes of several notable Pelco-D instructions are shown in Table 4.7 [72, p.12-16]. The bytes which set the pan speed and tilt speed may have values ranging from 0x01 (minimum speed) to 0x40 (maximum speed). These values do not control the magnitude of the speed in degrees per second, as the capability of each pan/tilt unit is different. They simply instruct the unit on what proportion of its maximum speed should be used.

Table 4.7: Notable Pelco-D Command Bytes.

Instruction	**Command 1**	**Command 2**	**Data 1**	**Data 2**
Tilt Up	0x00	0x08	0x00	Speed
Tilt Down	0x00	0x10	0x00	Speed
Pan Clockwise	0x00	0x02	Speed	0x00
Pan Counter-Clockwise	0x00	0x04	Speed	0x00
Stop	0x00	0x00	0x00	0x00
Query Tilt Angle	0x00	0x53	0x00	0x00
Query Pan Angle	0x00	0x51	0x00	0x00

The format of the response to a Pelco-D angle query is shown in Figure 4.6. The information regarding the queried angle is contained in byte 5 and byte 6 as the MSB and LSB, respectively. After the message is received and the checksum is validated, bytes 5 and 6 must be unpacked and formatted appropriately as they are received in packed binary form. The end result is a value in the form of hundredths of a degree. This value is divided by 100 if the angle is required to be in degrees.

Sync	Address	Command 1	Command 2	Data 1	Data 2	Checksum
-	-	-	-	MSB	LSB	-
byte 1	byte 2	byte3	byte 4	byte 5	byte 6	byte 7

Figure 4.6: Pelco-D Angle Query Response Format.

4.3.2 Implementation

Table 4.8 displays the information needed to set up serial communication between the Raspberry Pi and the pan/tilt unit. The pan/tilt unit supports multiple baud rates ranging from as low as 2400 bps to as high as 19200 bps. The highest setting of 19200 bps is chosen as more queries can be made per unit time. This is beneficial as it allows the angles of the pan/tilt unit to be monitored and adjusted more frequently, resulting in less error in its positioning. At this setting, approximately 2.9 ms is needed to transmit the 7-byte message and 2.9 ms to receive the response. In theory, the angle could be determined once every 5.8 ms.

Table 4.8: Pan/Tilt Unit Communication Configuration.

Parameter	Value
Baud rate	19200
Parity	None
Data bits	8
Stop bits	1
Device address	0x01

The functions that control the pan and tilt operation of the unit are relatively similar. Therefore, only a single flowchart is shown in Figure 4.7 to provide an overview of how both functions operate.

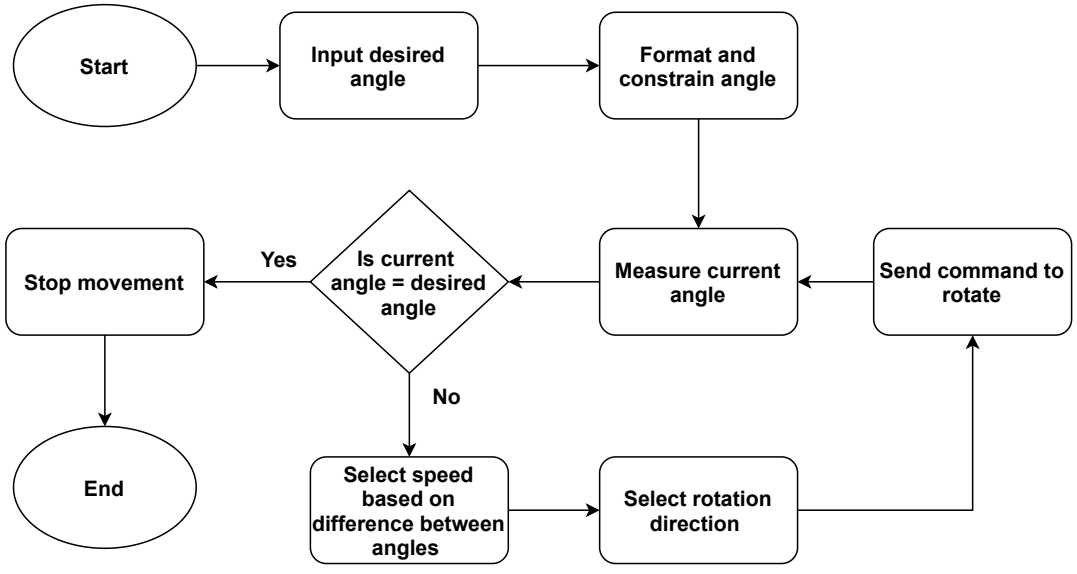

Figure 4.7: Pan/Tilt Unit Operation.

The desired input angle is inserted, and the angle is formatted. For pan operation, the input angle is formatted such that it lies between 0° and 360°. For tilt operation, the angle is constrained between -20° and 60° as per the mechanical capabilities of the unit. The current angle of the unit is measured and compared with the desired angle. If the angle does not match within a predetermined tolerance, the command to either pan or tilt the unit further is issued. The speed at which the unit pans or tilts is determined by how far away the desired angle is. The speed decreases as the current angle approaches the desired angle. This enables the unit to reach the desired angle with less error. During pan operation, the rotation direction (clockwise or counter-clockwise) is selected such that the desired angle is reached in the shortest time. In the case that the desired angle is exactly 180° from the actual angle, the unit is set to rotate clockwise by default.

4.3.3 Description of Functions

A few functions used to control the operation of the pan/tilt unit are briefly discussed below:

moveV(): This function controls the tilt angle of the pan/tilt unit as desired by the user.

moveH(): This function controls the pan angle of the pan/tilt unit as desired by the user.

selectSpeed(): This function sets the pan or tilt speed based on how far away the actual angle is from the desired angle. The closer the angles get, the slower the speed becomes to reduce positioning error.

direction(): This function determines the pan rotation direction such that the desired angle is reached as quickly as possible. If the desired angle is 180° from the current angle, clockwise rotation is selected by default.

checkSum(): This function calculates the 8-bit modulo 256 sum of the Pelco-D message. It does this using bytes 2 to 6 of a Pelco-D message described in section 4.3.1.

4.4 RS-485 ASCII Protocol

The Spectrafy devices both interface with the Raspberry Pi using the provided Spectrafy ComBoxes. The ComBox acts as both a power converter and communications converter. One ComBox is required for every device that is used, as it provides only a single output. This differs from the other RS-485 devices used as they were all connected on to the same serial bus.

4.4.1 Protocol Overview

The ASCII protocol is used in communications between the Raspberry Pi and the Spectrafy devices. As with Modbus and Pelco-D, RS-485 ASCII is also a master/slave serial communications protocol. The advantage of using this protocol is that the data is returned in a string format. As a result, the data is easy to read and process. It does not need to be unpacked from a packed binary format like the data returned in the other protocols. The drawbacks to using this protocol (as implemented by Spectrafy) include

no error checking, as no checksum or CRC is used, and large message sizes, as the data is returned in an ASCII string.

Data queries to the Spectrafy devices are simple to implement as only one command is used to retrieve data. The ASCII string that is sent is **N#_E**, where the # is replaced by the 3-digit or 4-digit serial number of the device that is queried [73, p.16]. The response to a data request differs depending on which device is queried.

According to Spectrafy [74, p.19], the format of the data in the string received from a SolarSIM-D2 device is:

$$N\text{"}serial\ number\text{"}\_\text{"}P_{out} \times 10\text{"},\text{"}(T_{out} + 50) \times 75\text{"},\text{"}(T_{in} + 50) \times 75\text{"},$$
$$\text{"}H_{in} \times 100\text{"},\text{"}V_1\text{"},\text{"}V_2\text{"},\text{"}V_3\text{"},\text{"}V_4\text{"},\text{"}V_5\text{"},\text{"}V_6\text{"},\text{"}termination\ character\text{"}$$

Similarly, Spectrafy [73, p.17] lists the format of the data in the received string from a SolarSIM-G device as:

$$N\text{"}serial\ number\text{"}\_\text{"}(T_{out} + 50) \times 75\text{"},\text{"}P_{out} \times 10\text{"},\text{"}H_{out} \times 100\text{"},\text{"}(T_{in} + 50) \times 75\text{"},$$
$$\text{"}H_{in} \times 100\text{"},\text{"}V_1\text{"},\text{"}V_2\text{"},\text{"}V_3\text{"},\text{"}V_4\text{"},\text{"}V_5\text{"},\text{"}V_6\text{"},\text{"}V_7\text{"},\text{"}V_8\text{"},\text{"}V_9\text{"},\text{"}termination\ character\text{"}$$

where P_{out} is ambient air pressure (kPa), T_{out} is ambient temperature ($^\circ C$), T_{in} is internal temperature ($^\circ C$), H_{out} is ambient humidity (%), H_{in} is internal humidity (%) and V_{1-9} are the voltages (mV) from the detectors on the devices. Each of these values is 8 bytes in size.

4.4.2 Implementation

The flowchart shown in Figure 4.8 illustrates the process by which information is retrieved from a Spectrafy device. Communication between the Raspberry Pi and the Spectrafy devices is configured as per the parameters listed in Table 4.9. A data request is made to the preferred device as described in section 4.4.1. The data is extracted from the received string and processed as necessary. The data is written to a .csv file that is formatted according to the specifications listed by Spectrafy [74, p.20], [73, p.18]. It is of utmost importance that this is done correctly, as the Spectrafy software used to process .csv files will only recognize files that meet the specification.

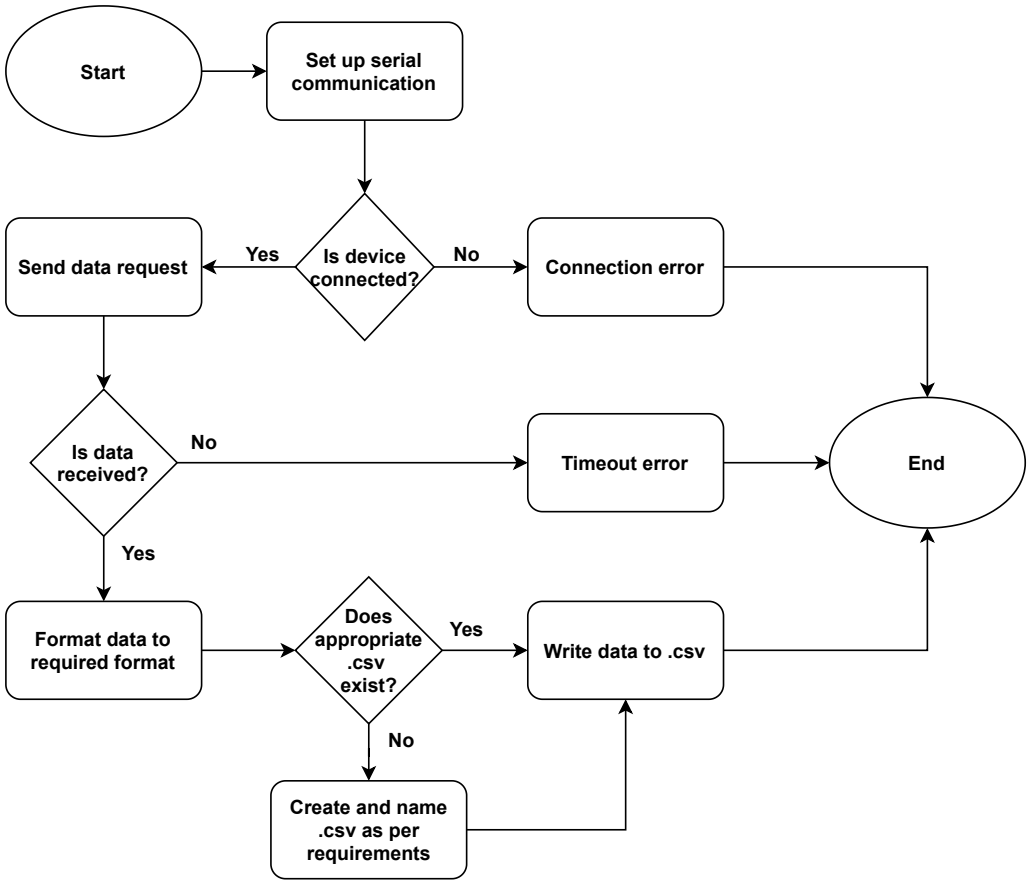

Figure 4.8: Spectrafy Data Request.

Table 4.9: Spectrafy Communication Configuration.

Parameter	**Value**
Baud rate	9600
Parity	None
Data bits	8
Stop bits	1
SolarSIM-G Serial No.	1048
SolarSIM-D2 Serial No.	162

The required formats of the .csv files are presented in Figure 4.9 and Figure 4.10. The files must be named as shown, beginning with the date during which the file is created. The headers must be named, and the data must be written in the same format as presented in the Figures.

2021-08-06_SSIM_Raw_Data_SN162

A	B	C	D
Time stamp	Time zone (hr)	Ambient temperature (C)	Ambient pressure (kPa)
2021-08-06 09:02:27	2	12.001	100.597
2021-08-06 09:12:14	2	13.341	100.606

E	F	G	H	I	J	K	L
Inside temperature (C)	Humidity (%)	V1 (mV)	V2 (mV)	V3 (mV)	V4 (mV)	V5 (mV)	V6 (mV)
12.805	25.546	87.023	360.546	626.981	533.521	599.93	128.455
14.086	25.633	133.686	578.265	754.247	721.049	740.855	169.277

Figure 4.9: SolarSIM-D2 .csv file.

2021-08-06_SSIM_Raw_Data_SN1048

A	B	C	D
Time stamp	Time zone (hr)	Ambient temperature (C)	Ambient pressure (kPa)
2021-08-06 09:02:23	2	14.188	100.702
2021-08-06 09:12:11	2	15.677	100.699

E	F	G	H
Ambient humidity (%)	Internal temperature (C)	Internal humidity (%)	V1 (mV)
83.841	14.117	21.202	653.443
78.882	15.641	21.264	735.288

I	J	K	L	M	N	O	P
V2 (mV)	V3 (mV)	V4 (mV)	V5 (mV)	V6 (mV)	V7 (mV)	V8 (mV)	V9 (mV)
863.421	1300.995	1684.215	2331.648	2176.488	1201.115	3568.47	978.804
963.068	1397.123	1758.814	2395.969	2173.536	1294.622	3475.327	973.344

Figure 4.10: SolarSIM-G .csv file.

4.4.3 Description of Functions

The functions used to retrieve and log the data captured by the Spectrafy spectral irradiance meters are briefly discussed below:

dev_connected(): Checks whether the intended device is connected. Returns **True** if the device is detected and **False** if it is not.

SSG_Data(): Retrieves and formats data from the SolarSIM-G spectral irradiance meter.

SSD_Data(): Retrieves and formats data from the SolarSIM-D spectral irradiance meter.

toFile_SSG(): Creates, names and formats .csv file needed to store data from SolarSIM-G spectral irradiance meter. Writes data to the file.

toFile_SSD(): Creates, names and formats .csv file needed to store data from SolarSIM-D2 spectral irradiance meter. Writes data to the file.

4.5 Camera

The Sony RX0 camera can officially be controlled remotely via USB using Sony's Remote Camera Control software. However, this software is only available for use on the Windows operating system. An alternative open-source library that allows devices running Linux based operating systems to interface with digital cameras is the gPhoto2 library. It provides the tools required to control the camera as needed. Therefore, this library is used in this project instead of the officially recommended software.

4.5.1 Servo Calculations

The camera used in this project must be powered on and off mechanically. A servo motor is used to physically depress the power button on the camera as required. This section discusses the theory behind the control of the servo motor that is used.

The angle of the servo motor is controlled using PWM (Pulse Width Modulation). The selected servo motor operates at a frequency of 50 Hz. Therefore, a pulse is expected to be received once every 20 ms. The width of the received pulse determines the angular position of the servo. The servo motor is specified to reach its minimum, neutral and maximum angles at the pulse durations shown in Table 4.10.

Table 4.10: Specified pulse duration and corresponding servo angles.

Servo Angle	Pulse Duration
0° (min.)	0.5 ms
90° (neutral)	1.5 ms
180° (max.)	2.5 ms

Under the assumption of a linear relationship between the angle of the servo motor and pulse duration, equation (4.5) is derived to determine the duty cycle required to achieve any given angle:

Due to the assumption of linearity, the equation has the form shown in equation (4.1), where t = pulse width, m = gradient, θ = servo angle.

$$t = m(\theta - \theta_1) + t_1 \tag{4.1}$$

The gradient, m, is determined in equation (4.2) using values obtained from Table 4.10.

$$m = \frac{1.5 - 0.5}{90 - 0} = \frac{1}{90} \tag{4.2}$$

Substituting the values for m and t_1 into equation (4.1) results in equation (4.3).

$$t = \frac{\theta}{90} + 0.5 \tag{4.3}$$

The relationship between pulse width and duty cycle is shown in equation (4.4), where T = period.

$$t = T \times Duty\ Cycle \tag{4.4}$$

Substituting equation (4.4), with period $T = 20$ ms, into equation (4.3) results in equation (4.5).

$$Duty\ Cycle = \frac{\theta}{1800} + 0.025 \tag{4.5}$$

An illustration of PWM control of a servo motor is presented in Figure 4.11. The servo angle is shown to vary based on the pulse width it receives.

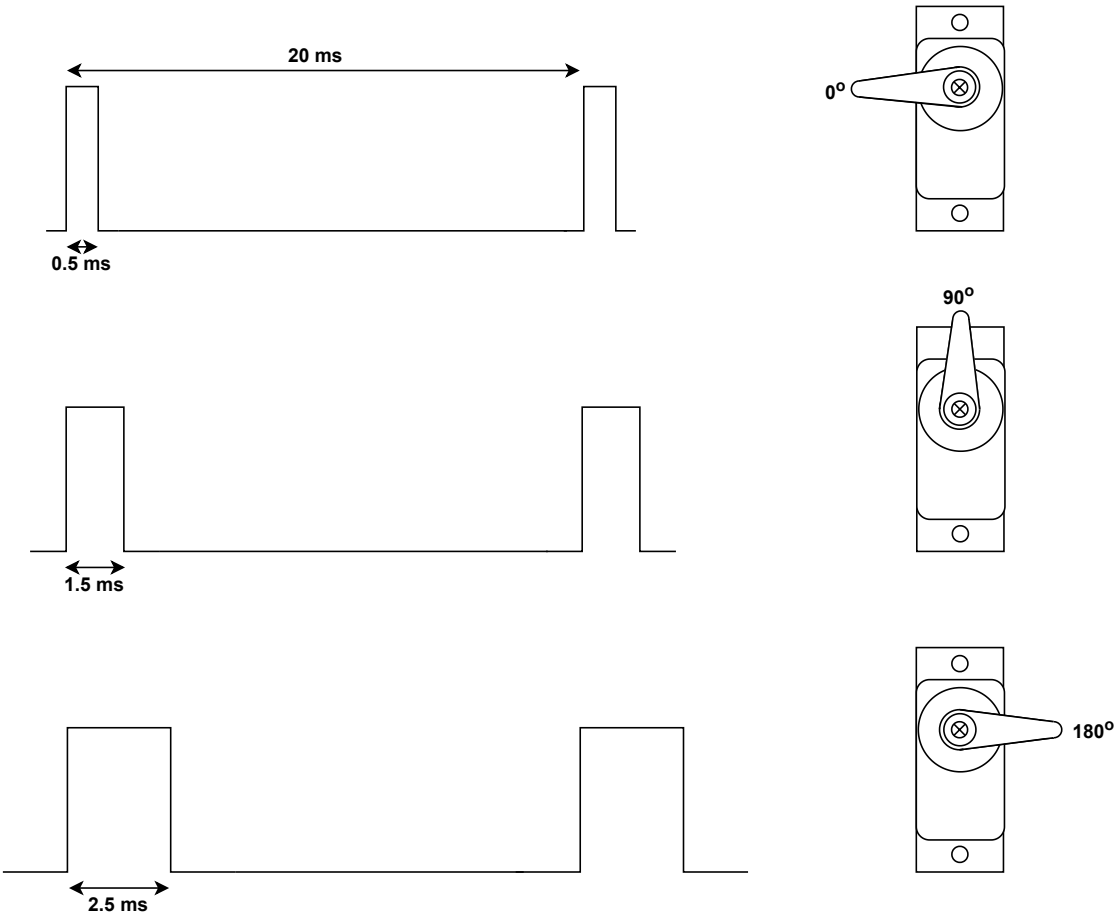

Figure 4.11: Servo control using PWM.

4.5.2 Implementation

The flowchart for the function used to capture images is shown in Figure 4.12. When called, the function checks to determine whether the camera is connected and can be detected. If the camera cannot be detected, the function raises a connection error. If the camera is detected, a folder is created to store the images taken during the day. An image is captured, timestamped and saved in the daily folder that was created.

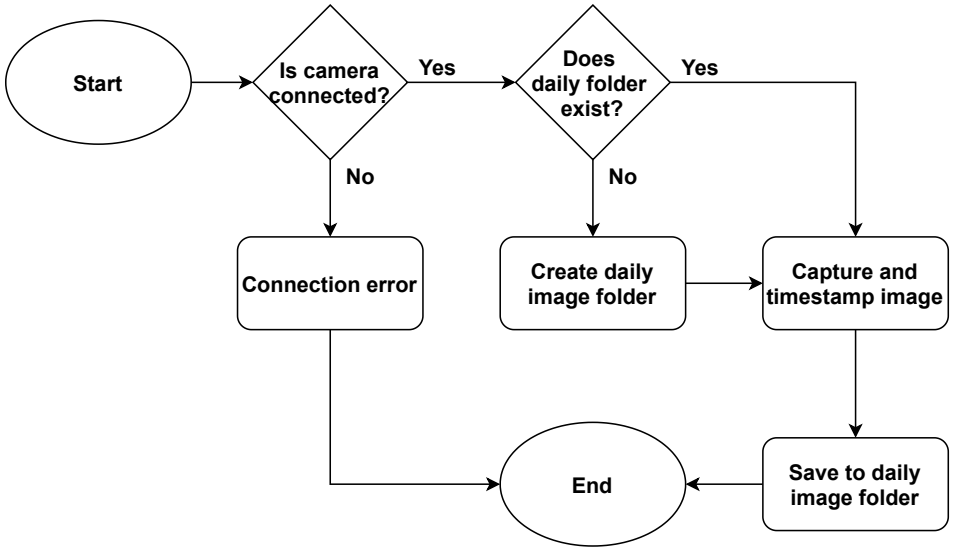

Figure 4.12: Capture Image Function.

Images are captured at a resolution of 15.4 megapixels with 24-bit colour depth in JPEG format. This format is chosen as it offers images of acceptably high quality at a relatively small file size, with an average size of approximately 3 MB per photograph. Uncompressed formats (such as RAW) provide higher quality images. However, the file size is much larger. It is not practical to use an uncompressed format for this application as a large number of photos are taken daily, and storing and downloading these photos would become cumbersome. Images are grouped in folders by the day they were taken for the convenience of the user.

A flowchart of the function used to power the camera on is shown in Figure 4.13. The function does a check to determine if the camera is already active and connected. If the camera is not detected, the servo motor is activated to toggle the power button on the camera. The function pauses for 10 seconds to allow the camera the time needed to activate and connect to the Raspberry Pi and verifies that the camera has been successfully connected. If the camera is not detected, the function attempts to activate it 2 additional times before raising a power-on error. The function to power the camera off operates similarly. The primary difference is that it will toggle the servo only if the camera is determined to be powered on.

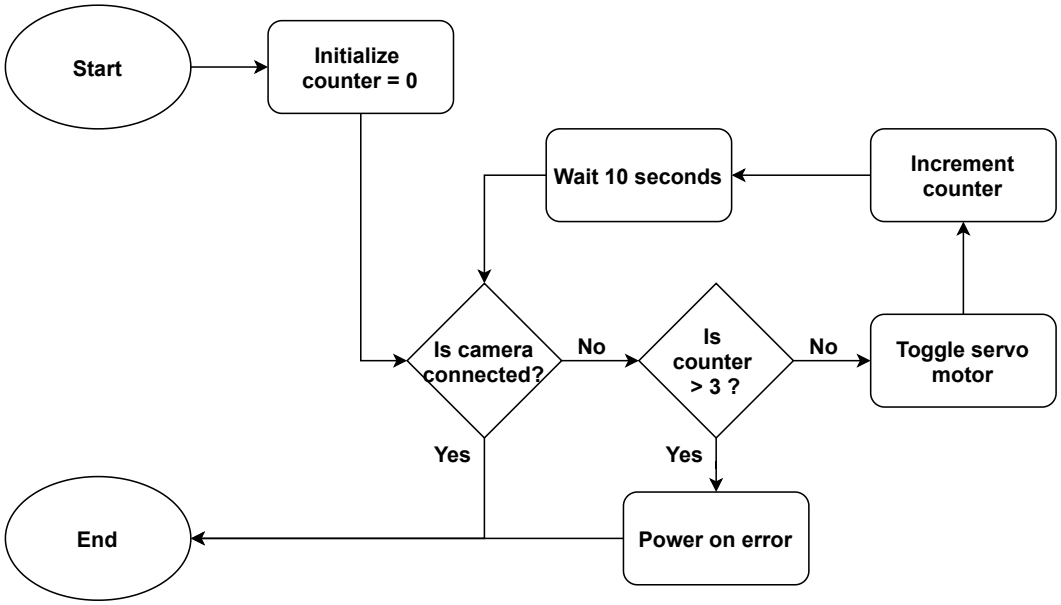

Figure 4.13: Power Camera On.

The servo angle required to press the power button on the camera is measured to be 100°. The flow diagram of the function used to toggle the servo motor is shown in Figure 4.14. The function begins by setting up the PWM according to the parameters shown in Table 4.11. The duty cycle is set to 2.5%, corresponding to a pulse width of 0.5 ms, to initialise the servo angle to 0°. The function uses equation (4.5) to determine that the duty cycle required for the servo to reach an angle of 100° is 8%. The duty cycle is changed and held to 8% for 500 ms to allow the camera time to register the button press. The duty cycle reverts back to 2.5%, moving the servo back to the initial position.

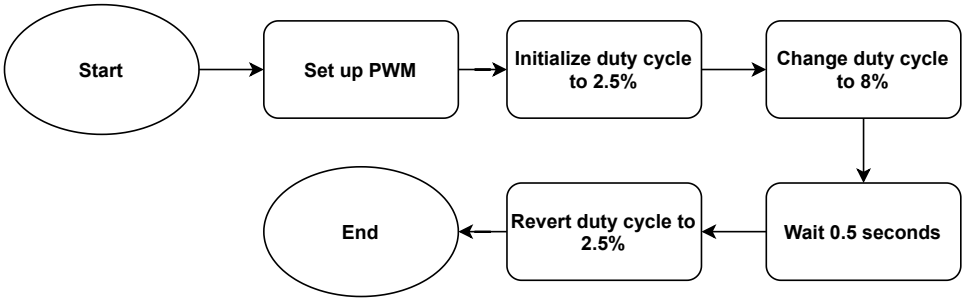

Figure 4.14: Toggle Servo.

Table 4.11: Parameters for PWM setup.

PWM Setup	
GPIO Mode	Board
GPIO Pin	12
Frequency	50 Hz

4.5.3 Description of Functions

The functions used in regards to capturing images are listed below:

capture(): Captures and timestamps an image. Saves the captured image into the specified directory.

power_on(): Toggles the servo motor such that it presses the button to power the camera on.

power_off(): Toggles the servo motor such that it presses the button to power the camera off.

4.6 Solar Tracking

Various algorithms exist that are able to estimate the position of the sun in the sky accurately. Each of these algorithms calculates the solar position with varying degrees of precision, with those that are more precise being more complex to implement.

The Almanac algorithm presented by Michalsky [75] is found to estimate the position of the sun to within 0.01° until the year 2050. The PSA algorithm presented by Blanco-Muriel et al. [76] improves on the Almanac algorithm and estimates the solar azimuth and zenith angles with improvements of up to 15% and 22% respectively. The algorithm presented by Reda and Andreas [77] claims to calculate the solar zenith and azimuth angles with uncertainties of ±0.0003°, exceeding the capabilities of both the Almanac and PSA algorithms.

However, the pan/tilt unit used to point the instruments towards the sun is not precise enough to take advantage of the accurate estimates afforded by the aforementioned algorithms. Therefore, the decision is made to estimate the position of the sun with the use of the equations presented in Chapter 2.2.4, owing to the reduced complexity in implementation. An additional algorithm is employed afterwards to improve the accuracy by correcting for any misalignment of the measurement station and its instruments. This makes the station more robust when it is deployed.

The relevant equations are repeated below for convenience:

$$\delta = 23.45 \sin\left[\frac{360}{365}(n - 81)\right], \tag{4.6}$$

$$H = \left(\frac{15^\circ}{hour}\right) \times (hours\ \ before\ \ solar\ \ noon) \tag{4.7}$$

$$ST = CT + \frac{4\ \ minutes}{1^\circ}(Local\ \ Time\ \ Meridian - Local\ \ Longitude)^\circ + E \tag{4.8}$$

$$E = 9.87 \sin 2B - 7.53 \cos B - 1.5 \sin B\ \ (minutes) \tag{4.9}$$

$$B = \frac{360}{364}(n - 81) \ \ (degrees) \tag{4.10}$$

$$\beta = \arcsin(\cos L \cos \delta \cos H + \sin L \sin \delta) \tag{4.11}$$

$$\phi_S = \arcsin\left(\frac{\cos \delta \sin H}{\cos \beta}\right) \tag{4.12}$$

The flowchart in Figure 4.15 illustrates the procedure followed to estimate the solar azimuth and elevation angles. The solar declination angle is calculated using equation (4.6), followed by the hour angle with equations (4.7) - (4.10). Once this is done, the solar elevation and azimuth are calculated using equations (4.11) and (4.12), respectively.

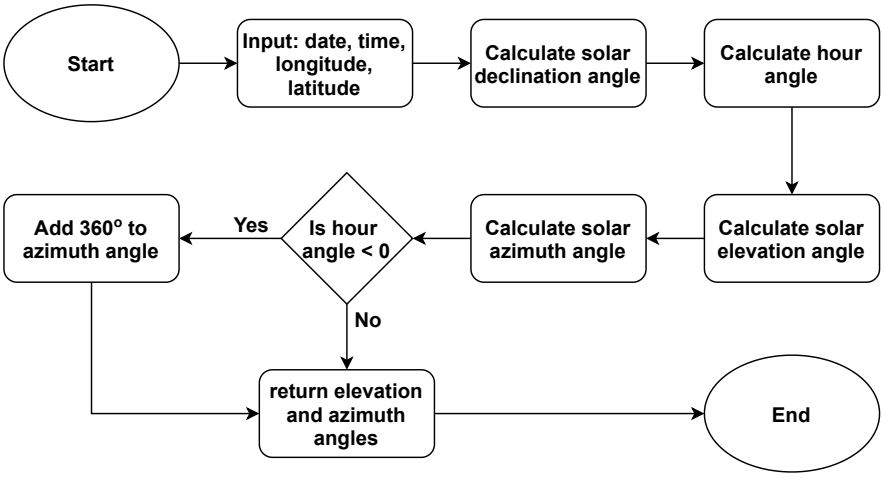

Figure 4.15: Solar Position Overview.

The flowchart of the calibration sequence used to align the pyrheliometer and SolarSIM-D with the sun is shown in Figure 4.16. This process is essential as both devices have only a 5° field of view. The instruments are pointed towards the estimated solar position. The azimuth angle is then rotated 5° counter-clockwise of that estimated position. The DNI is measured, and the corresponding angle is recorded. The station is rotated 1° clockwise, and the DNI and angle are recorded again. This process repeats until the measurement station has completed 11 measurements and now facing 5° clockwise from the original estimated azimuth angle. The DNI values are compared, and the measurement station rotates to the azimuth angle at which the highest value was recorded. The same process is used to determine the elevation angle for the maximum DNI, with the station taking measurements from -5° to +5° of the estimated elevation angle. The range -5° to +5° of the estimated position is selected in order to make the station more robust. The station will be able to track the sun even if it is misaligned and not perfectly facing North. The drawback of such a large range is that more time is needed to find the optimum position.

Another disadvantage of this method is that the system could struggle to accurately track the sun if there are fast moving clouds overhead.

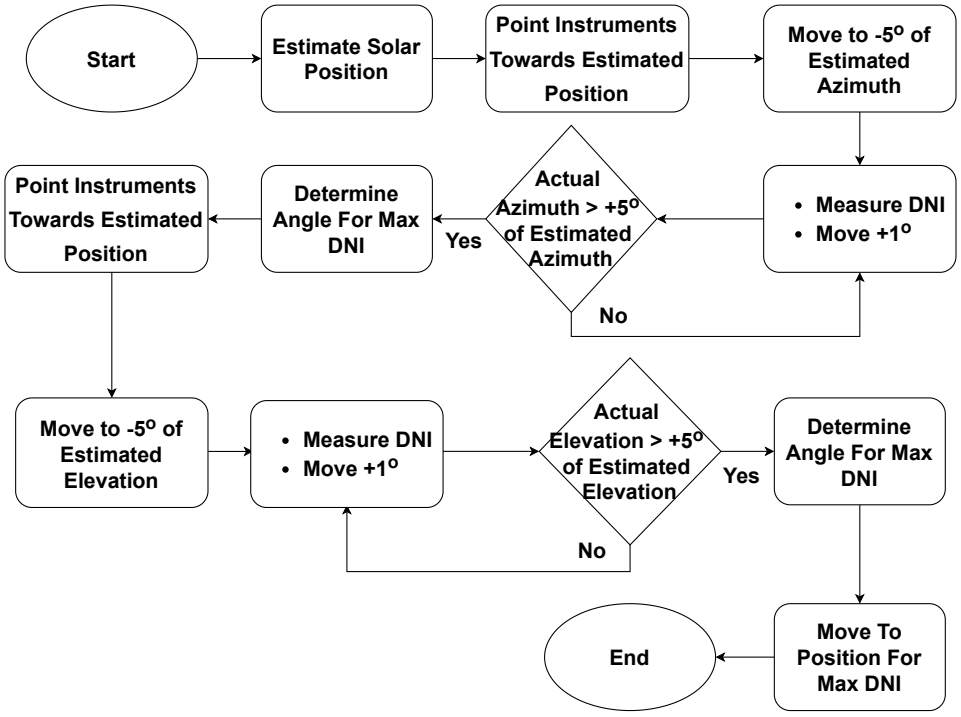

Figure 4.16: Positional Calibration.

4.6.1 Description of Functions

The functions used to determine the position of the sun in the sky and align the pan/tilt unit are briefly discussed below:

declination_Angle(): Calculates and returns the solar declination angle.

solar_Noon(): Calculates and returns the time at which solar noon will occur.

hour_Angle(): Calculates and returns the hour angle.

alt_Angle(): Calculates and returns the solar elevation angle.

az_Angle(): Calculates and returns the solar azimuth angle.

cal_Azimuth(): Corrects the orientation of the pan/tilt unit so that its azimuth angle is aligned with the sun.

cal_Elevation(): Corrects the orientation of the pan/tilt unit so that its tilt angle is aligned with the sun.

4.7 Measurement Sequence

The measurement sequence of the station is configured as shown in Figure 4.17. The measurement sequence begins by orientating the pan/tilt unit such that the instruments on the station are pointed towards the desired position. The positional calibration described in Chapter 4.6 is used to accurately point the instruments towards the sun if needed. It is important to note that while the positional calibration tracks the sun accurately under clear sky conditions, it might struggle to track the sun accurately under overcast conditions. A minimum of 2 seconds elapses from the time the pan/tilt unit points towards the desired position before any measurements are made. This is because the Kipp & Zonen instruments have a 2 second response time before the measurements they capture are acceptable. An image of the sky is taken first as it takes the longest to capture and save. Data is then captured by the SHP1 pyrheliometer, SMP10 pyranometer, SolarSIM-D2 Spectral Irradiance Meter and SolarSIM-G Spectral Irradiance Meter in that order. The process repeats until measurements are recorded in all desired positions.

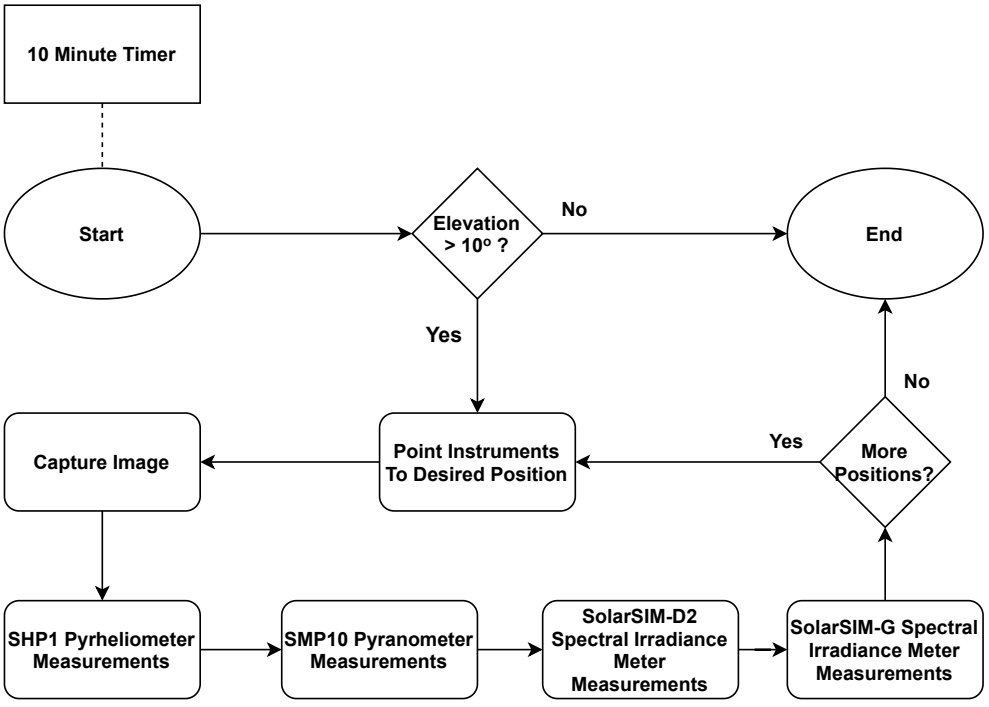

Figure 4.17: Measurement Sequence.

The program is set to execute once every 10 minutes. This interval can be adjusted by the user as required. The station is set only to perform measurements if the elevation angle of the sun is greater than 10°, as the pan/tilt unit only has a tilt range of 0° - 80°.

4.8 Chapter Review

This chapter discussed the software used to control the measurement station. An overview of the protocols used to communicate with the various devices is provided, and their implementation is discussed.

The Kipp & Zonen instruments, Spectrafy instruments and pan/tilt unit all communicate via RS-485. They use the Modbus RTU, RS-485 ASCII and Pelco-D protocols, respectively. The Kipp & Zonen devices capture broadband irradiance data and record it in a .csv file. The Spectrafy devices record the various data they collect in .csv files that are formatted specifically as required by Spectrafy to be processed using the supplied Spectrafy software. They are each connected on a separate serial bus.

The camera is controlled using the tools provided in an open-source library. The captured images are timestamped and stored in a folder by the day they are taken. A servo motor is used to power the camera on and off mechanically. The theory behind the control of this servo motor is discussed and implemented.

Various solar tracking algorithms are then investigated to accurately align the instruments on the station with the sun. It is determined that the high accuracy afforded by using complex algorithms is not beneficial due to the mechanical limitations of the pan/tilt unit. The equations presented in Chapter 2.2.4 are used to estimate the position of the sun, owing to their reduced complexity in implementation. A calibration algorithm is implemented afterwards to fine-tune the tracking accuracy and provide better disturbance rejection. Finally, the measurement sequence used by the station to collect data is described. The sequence can be configured according to the specific needs of the user. The set up of the station and the currently configured measurement positions are described in Chapter 5.

Chapter 5

Station Set Up and Data Collection

5.1 Introduction

This chapter begins by describing the location used to test and verify the operation of the measurement station. The set-up and connections of the station are discussed, and the process used for data collection is explained and motivated.

5.2 Test Site

The measurement station is set up on the roof of the Department of Electrical and Electronic Engineering at Stellenbosch University (33°55'42.9"S 18°52'01.4"E) for testing purposes. This location is selected due to its close proximity with the workshop and other facilities that are required to easily resolve any problems that are identified with the station during testing. The system is powered by one of the many PV panels that are already installed on the roof. The path of the movement of the sun over the test site throughout the year is presented in Figure 5.1.

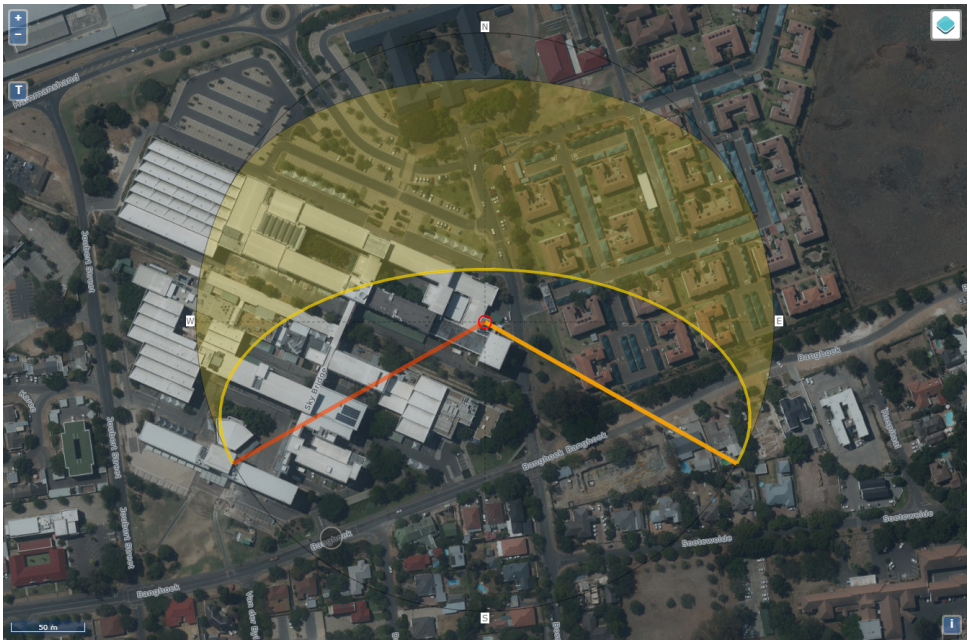

Figure 5.1: Sun Path Above Test Site.

This location generally offers a very clear view of the passage of the sun in the sky throughout the day. The buildings to the east are not found to impact measurements in the mornings. However, during late afternoon, the buildings to the west may obstruct the view of the sun as shown in Figure 5.2. Measurements taken during these times are discarded. Once the operation of the measurement station is validated, the measurement station would ideally be deployed in a flat area with clear, unobstructed views of the horizon to collect the data required for irradiance forecasting.

Figure 5.2: Obstruction of Sun by Buildings.

5.3 Set-Up of Measurement Station

5.3.1 Set-Up

The completely assembled measurement station is shown in Figure 5.3. The components of the measurement station are mounted on to a tube steel frame. The frame is fixed to the structure which supports the PV panel, and it is weighed down by sandbags to prevent it from falling over. Ideally, the frame would be fixed to poles driven into the ground for support, but this is not possible at this test site as it is on the roof of a building. The station is made to face true North with the aid of a compass and taking into account the local magnetic declination of approximately -25.8°. Its orientation is fine tuned by setting the platform to face directly into the sun at solar noon and using the alignment aids on the pyrheliometer to adjust its bearing until it is correctly aligned.

The aluminium platform enclosure houses the Raspberry Pi, the power supplies and the digital camera as these devices require protection from the elements and cannot be left exposed. There is additional space within the enclosure to mount solid-state drives if more storage capacity is necessary. This enclosure is mounted on top of the pan/tilt unit. The instruments responsible for data collection are attached to the lid and sides of the enclosure. Since all the devices are mounted on top of the pan/tilt unit, there is no relative motion between them. This ensures that the cables connecting them do not get twisted or damaged while the station operates.

The IP65 electrical enclosure mounted at the bottom of the tube steel frame contains the MPPT, battery pack, router and power supply. The weight of the battery pack at the bottom helps to lower the centre of gravity of the entire system, providing additional stability.

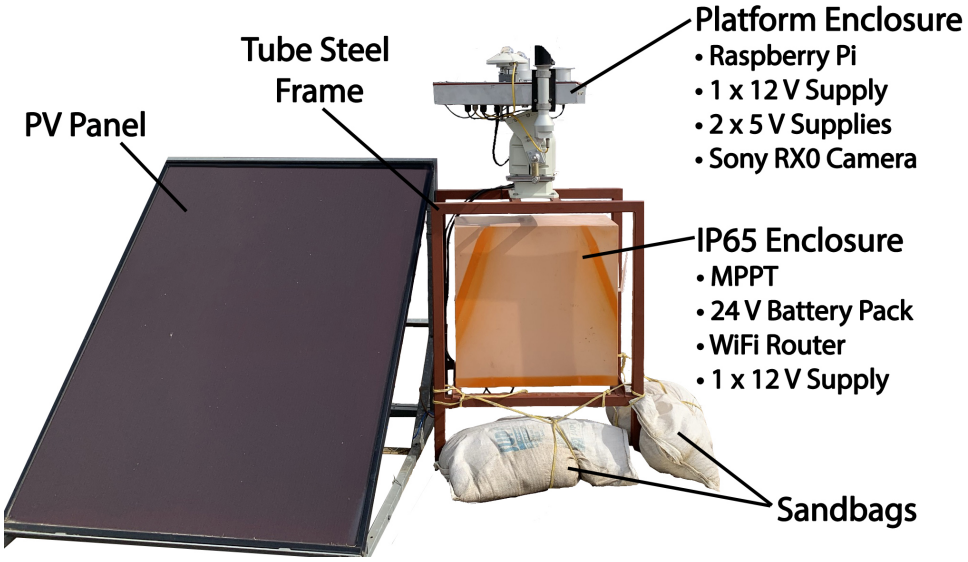

Figure 5.3: Measurement Station Overview.

The pan/tilt unit features power and communications pass-through from its fixed base to the part that rotates and tilts. This allows the devices inside the IP65 electrical enclosure to connect to the devices on top of the pan/tilt unit without any risk of cables being damaged by the motion of the unit. The pass-through power cable carries 24 V DC from the battery pack to the power supplies contained within the platform enclosure. The communications pass-through cable is used to connect the Raspberry Pi to the WiFi router via Ethernet. A cable connection is required for communication with the Raspberry Pi - wireless communication is not possible as the aluminium enclosure shields the Pi from wireless signals.

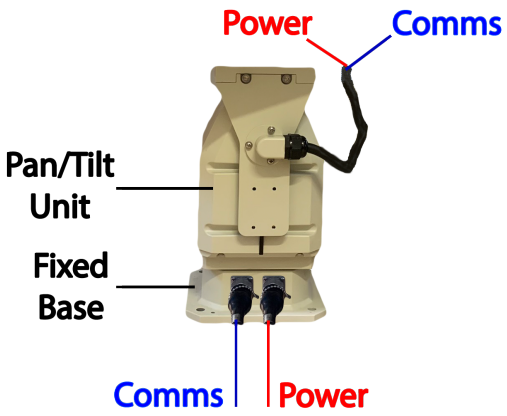

Figure 5.4: Power and Communications Pass-through on Pan/Tilt Unit.

As mentioned in Chapter 3.3.4, a 20° wedge is fabricated and placed between the surface of the pan/tilt unit and the aluminium enclosure. This wedge provides the offset

required so that the unit can tilt from 0° (horizontal for GHI measurements) to 80° (almost vertical to view the horizon), instead of the standard -20° to 60° tilt range which is less useful in this application.

During initial testing, it was seen that the pan/tilt unit had difficulties in tilting upwards. This is despite the fact that the actual payload of 16.8 kg is approximately 24% less than the advertised maximum capabilities of the unit. Initially, a counter-weight system was implemented in an attempt to reduce the resultant torque on the unit. This was found to be unsuccessful because the counter-weights could only be mounted a short distance from the pivot point, which resulted in excessively heavy weights being required to produce sufficient counter-torque. The issue was resolved by creating an apparatus with a spring which could be mounted on the pan/tilt unit without interfering with its operation. The system with the spring produces enough counter-torque to significantly improve performance. The spring stiffness for optimal performance is determined in Chapter 3.7 to be 4.88 N/mm. An exact spring could not be manufactured as a bulk order is required by the manufacturers for a production run. However, a spring with a measured spring stiffness coefficient of approximately 5.5 N/mm and unstretched length of 95 mm was found in the workshop. This spring is appropriate and is successfully used to balance the torque on the pan/tilt unit.

The implementation of the 20° wedge used to offset the tilt range, and the implementation of the spring apparatus used to balance the torque is shown in Figure 5.5. The rubber gasket used to create a weather-tight seal between the back of the enclosure and the lid is also visible.

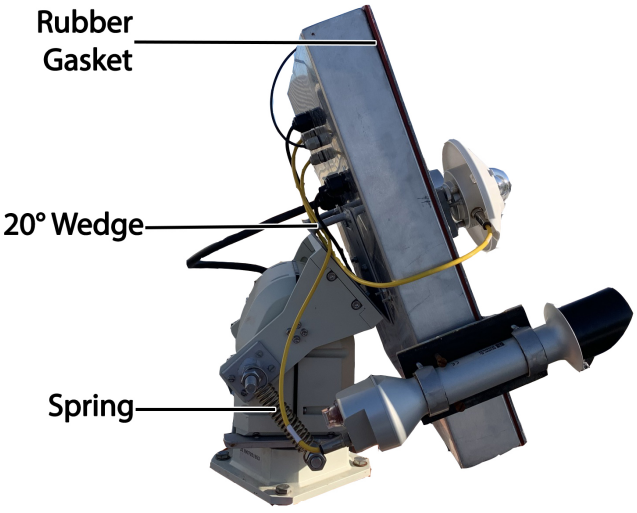

Figure 5.5: Implementation of 20° Wedge and Spring Apparatus on Station.

The instruments are mounted on the aluminium enclosure as shown in Figure 5.6. The Spectrafy SolarSIM-G and the Kipp & Zonen SMP10 are mounted on the lid of the enclosure and leveled with the included bubble levels when the platform is in the horizontal position. The Spectrafy SolarSIM-D2 is mounted on its own platform which is attached to the side of the enclosure. The direction in which it faces is fine tuned by adjusting the height of each of the 3 screws that hold it in place. It is aligned

with the sun by turning the platform to face directly into the sun at solar noon, and adjusting the height of each of the screws until a bright spot of light passes through the alignment pinhole and falls directly over the alignment spot marked on the device. The Kipp & Zonen SHP1 is mounted using an aluminium bracket which attaches to the lid of the enclosure. The direction it faces can be finely adjusted using screws on the side of the bracket. The process for its alignment with the sun is similar to that of the Spectrafy SolarSIM-D2. The lid of the enclosure is textured using glass fibres and painted with matte grey paint to scatter incident light in different directions to avoid influencing measurements as much as possible. The color was chosen such that the enclosure absorbs as little heat as possible. The devices contained inside the enclosure would not function correctly if the internal temperature is too high. The instruments are placed in such a way that the weight is distributed as evenly as possible on the station.

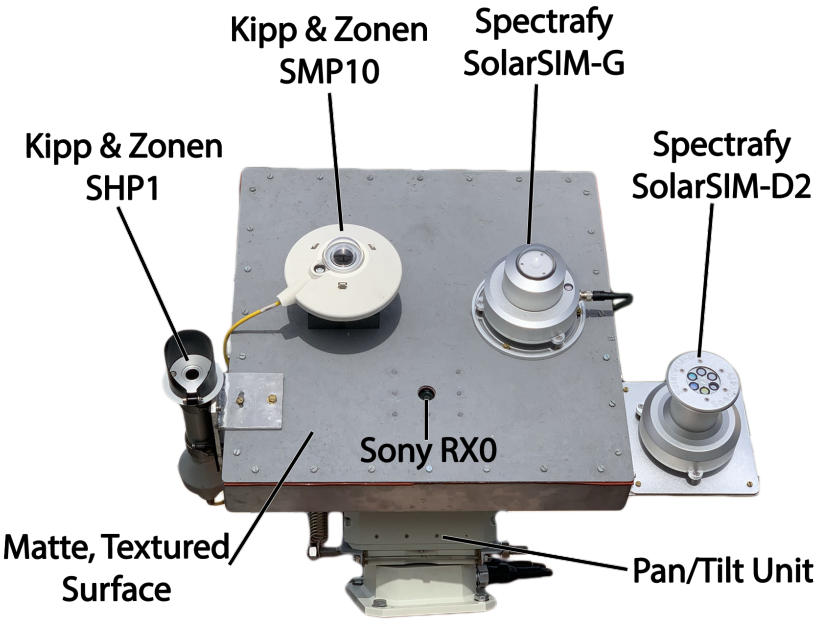

Figure 5.6: Instruments on Measurement Station.

The Kipp & Zonen SMP10 pyranometer and the Spectrafy SolarSIM-G spectral irradiance meter must have the height of their domes at the same level. This prevents each device from influencing the measurements of other device, either by reflecting light into its sensor, or by casting a shadow over it. The domes of the devices are leveled as shown in Figure 5.7. The Kipp & Zonen SMP10 is noticeably shorter than the Spectrafy SolarSIM-G, and so an HDPE (High Density Polyethylene) block is machined and placed between the platform and the pyranometer to increase its height appropriately. HDPE is selected as the material for the block for its low weight, high strength and easy machinability. It is also very durable, and has good chemical and corrosion resistance.

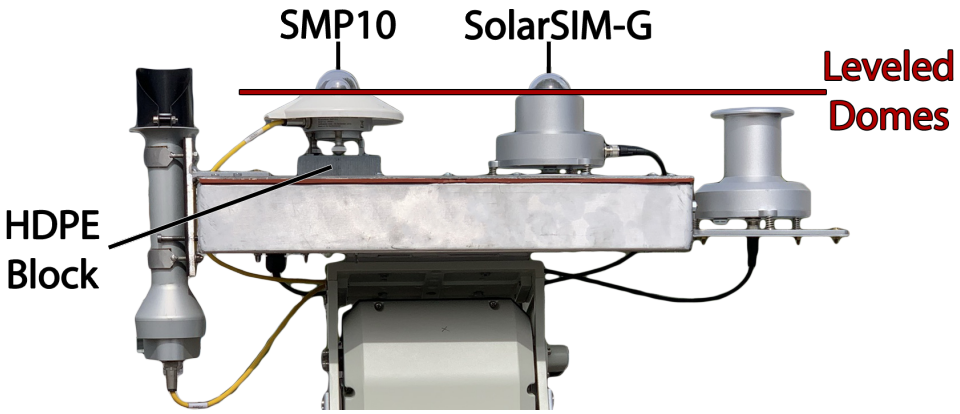

Figure 5.7: Leveled Domes of Kipp & Zonen SMP10 and Spectrafy SolarSIM-G.

The Sony RX0 digital camera is mounted inside the enclosure using the 3D-printed mounting bracket designed in Chapter 3.6.3. As previously discussed, it must be mounted inside the enclosure because it is not weather-resistant when the back cover is removed to enable charging and communication. The mounting of the camera and servo motor inside the enclosure is shown in Figure 5.8. A rubber gasket is placed between the enclosure lid and camera, and silicone is used to seal the surrounding area to ensure that no water or dust can enter the enclosure from the outside.

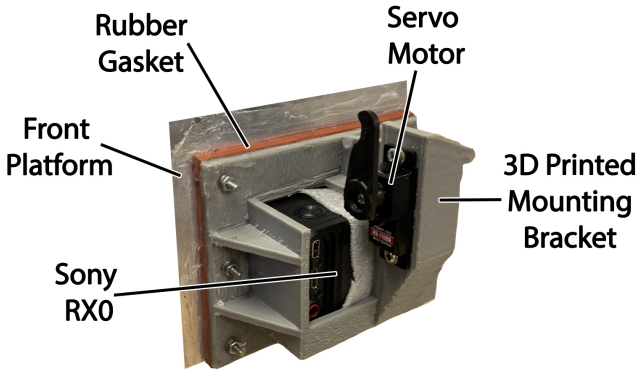

Figure 5.8: Camera and Servo Motor Mounted Inside Enclosure.

5.3.2 Device Connections

The physical connections between the devices on the measurement station are shown in Figure 5.9. As previously stated, 24 V power and Ethernet communication is made accessible to the devices on top the pan/tilt unit via the available pass-through functionality. The 24 V DC serves both as the power source for the unit itself, as well as an input to both 5 V supplies and the single 12 V supply. All the supplies share a common ground. The first 5 V supply provides power to the Raspberry Pi and its peripheral devices, while the second 5 V supply exclusively powers the servo motor. The 12 V supply is used to power the Kipp & Zonen instruments.

The digital camera is plugged directly into one of the USB ports of the Raspberry Pi for both power and communication. The RTC and servo motor interface with the Pi via

its dedicated SPI pins and PWM pin respectively.

The Raspberry Pi communicates with and controls the pan/tilt unit and the Kipp & Zonen instruments using an RS485 converter. The Spectrafy instruments are connected to the Raspberry Pi using the provided Spectrafy ComBoxes. The ComBoxes act as RS485 converters as well as power supplies for the instruments. Since each instrument makes use of its own unique ComBox and each ComBox is on a unique serial bus, it is important that the Raspberry Pi can differentiate between the two ComBoxes. This ensures that the correct commands are sent to the correct device. This is done by assigning each ComBox a fixed port name. A USB device list file is created which includes port rules regarding the unique attributes of each ComBox. Once a ComBox is plugged into the Pi, a check is done to identify its attributes. Once the ComBox is identified, the port name corresponding to the identified attributes is allocated to it.

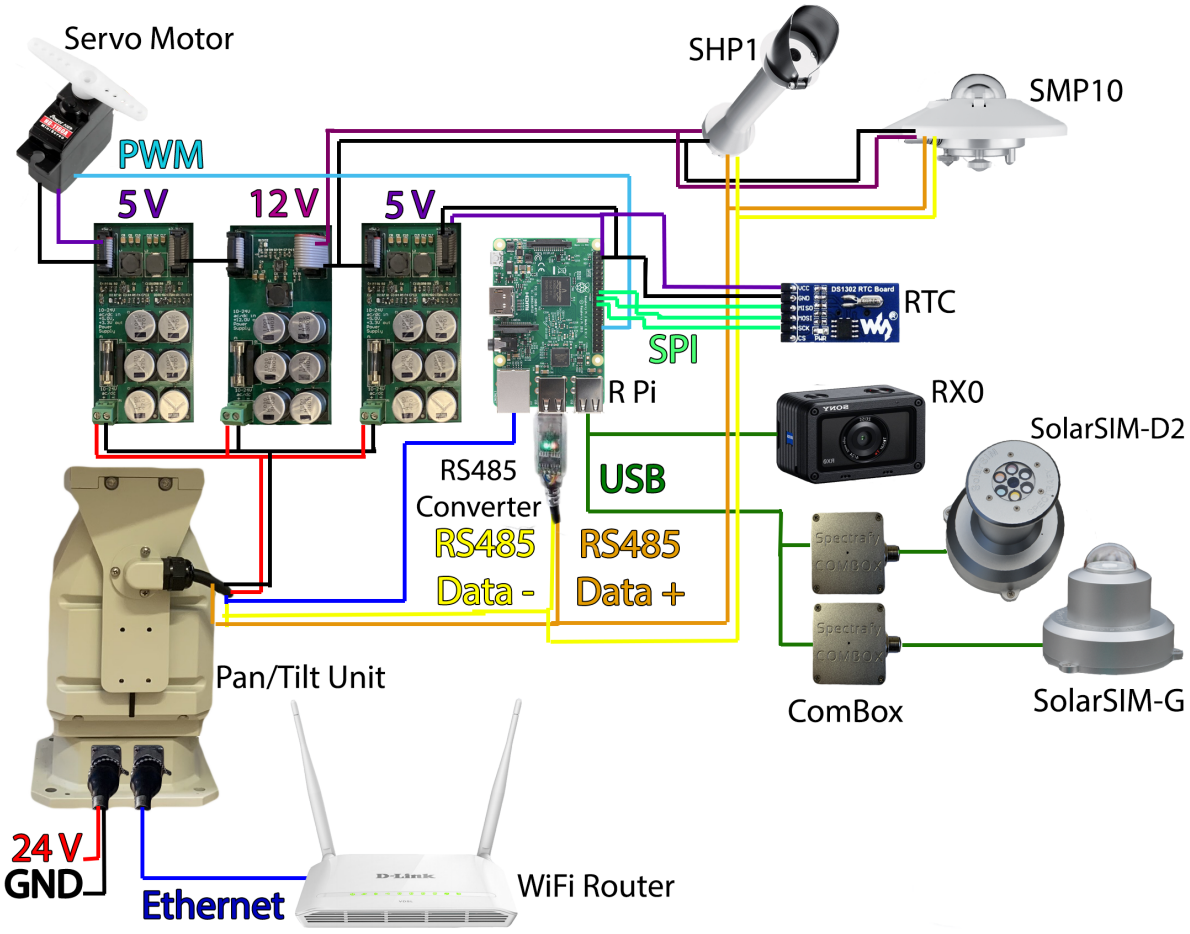

Figure 5.9: Device Connections.

The connections made between the devices inside the IP65 electrical enclosure are shown in Figure 5.10. The output of the PV panel is connected to the input of the MPPT charge controller. The battery pack, consisting of 2 series-connected 12 V 102 Ah silver-calcium batteries, is connected to the output of the MPPT via a fuse. The fuse is installed to prevent damage in the case that the batteries are somehow shorted. The output of the battery pack is fed up to the pan/tilt unit to provide power to the

measurement station. The 12 V supply in the electrical enclosure also receives 24 V from the battery pack and provides power to the WiFi router, which is used to connect the Raspberry Pi on to the local network. The antennas of the WiFi router are mounted on the outside of the enclosure with the aid of 2 SMA (SubMiniature version A) extension cables. The antennas are mounted outside the enclosure because the enclosure shields the router from all external wireless signals.

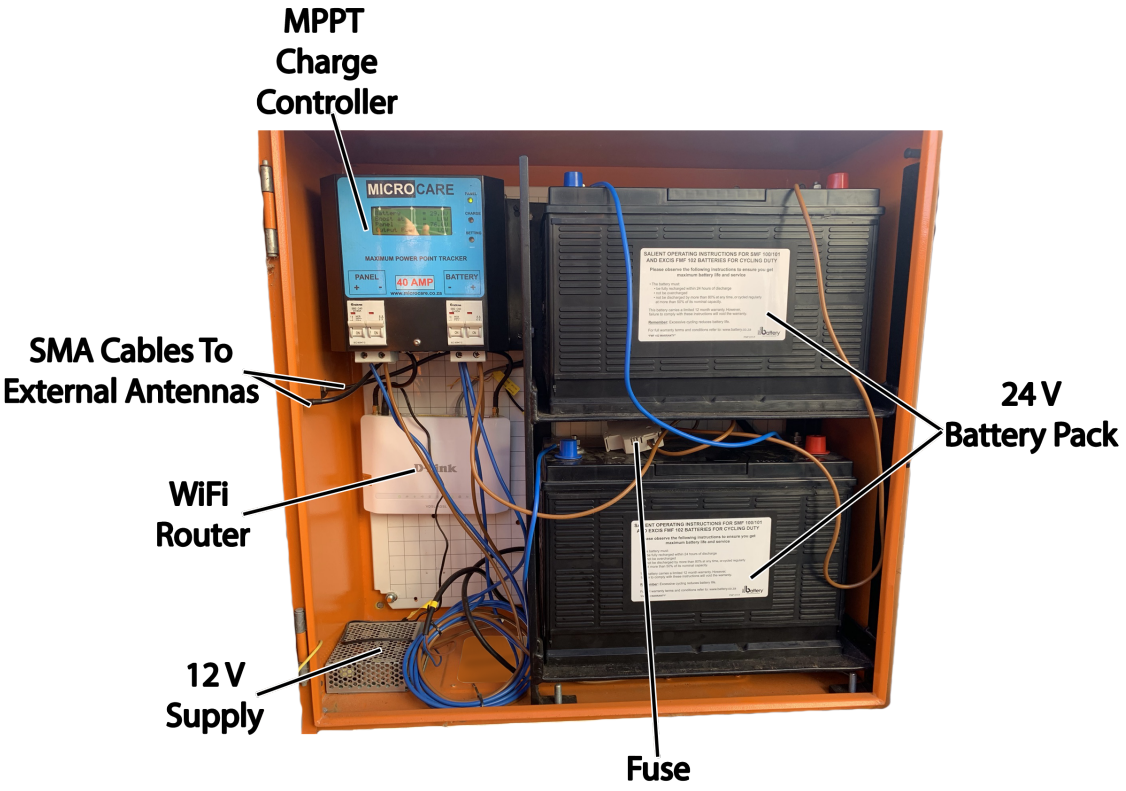

Figure 5.10: Connections inside of IP65 Electrical Enclosure.

5.4 Data Collection

5.4.1 Measurement Position Configuration

The measurement station is currently configured to capture data in 4 distinct measurement positions, as shown in Figure 5.11.

In position 1, the station is configured to point the instruments directly towards the sun. The azimuth angle of the station is aligned with that of the sun, and the platform is tilted such that it is perpendicular to the incident solar irradiance. The optimum tilt angle is determined using equation (5.1), as presented by Masters [8, p.196]. This measurement position is selected because the collected data can be correlated to the output of PV panels with double-axis tracking.

$$Tilt\ Angle = 90° - Solar\ Elevation\ Angle \tag{5.1}$$

Position 2 has the station configured to face North, with the platform tracking the zenith angle of the sun for optimal tilt. This measurement position is selected to allow for the correlation of measured data with the output of PV panels with single-axis tracking (East-West axis).

Position 3 has the station facing North, with the platform having a tilt angle of 30°. It is common for fixed-tilt PV panels in South Africa to be placed at a tilt angle of 30°. According to Masters [8, p.194], the ideal tilt angle of a fixed-tilt PV panel is equal to the local latitude angle. Therefore, an angle of 30° is chosen to account for the average latitude of South Africa. The data collected in this position can be correlated to the output of fixed-tilt PV panels in South Africa.

In position 4, the station faces North and the platform has a 0° tilt (i.e. it is horizontal). This is done to enable GHI and corresponding global spectral irradiance measurements. This is also the position occupied by the station while it is inactive in between measurements and overnight. It is ideal as it minimizes the cross sectional surface area of the station in the direction of the wind. This reduces wind resistance and lowers the risk of damage to the station.

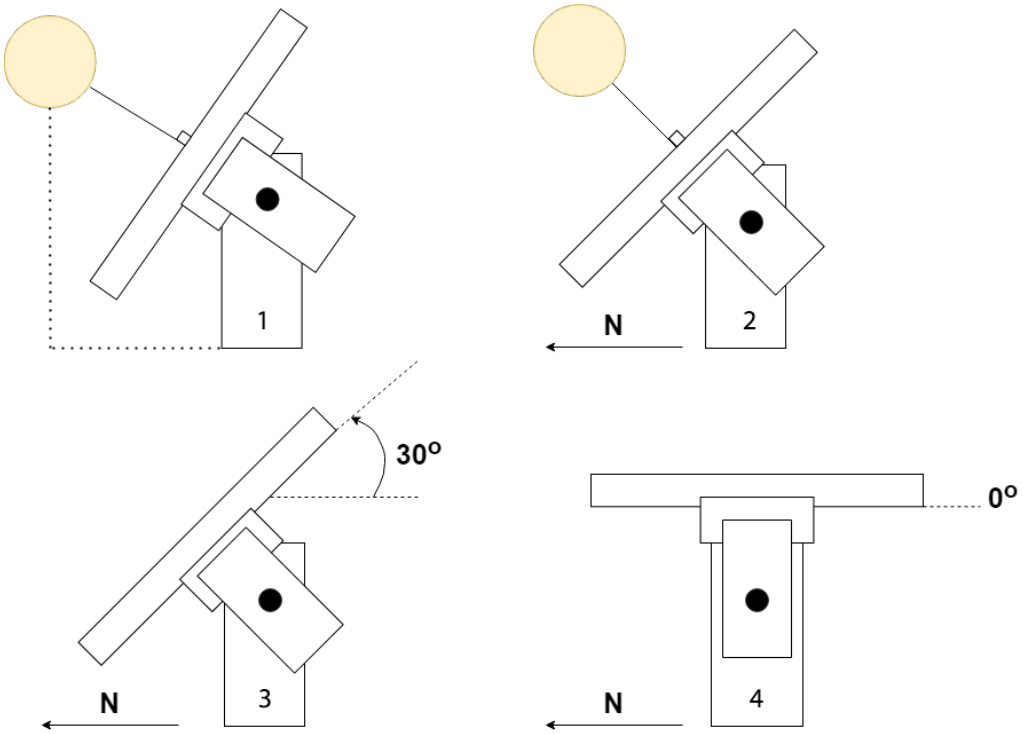

Figure 5.11: Currently Configured Measurement Positions.

Figure 5.12 shows a potential future measurement position configuration. In this configuration, the station would capture an array of measurements and images which could be stitched together to obtain a spectral map of the sky dome above.

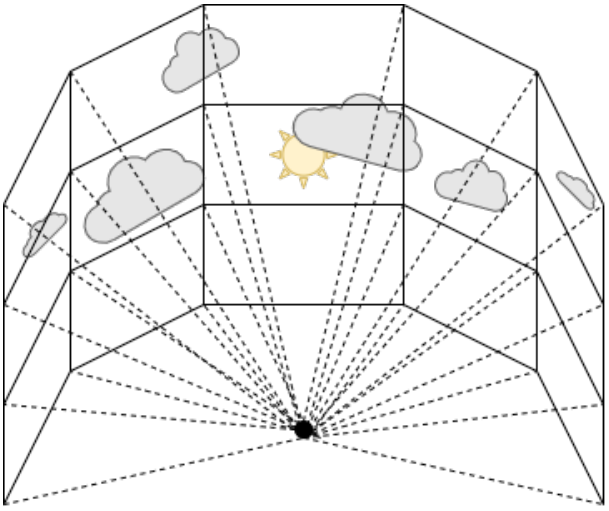

Figure 5.12: Potential Future Measurement Configuration.

5.4.2 Data Retrieval

Measurements are made only while the solar elevation angle is above 10° owing to the tilt angle limitations of the pan/tilt unit. Measurements are initiated once every 10 minutes, and take approximately 3 minutes to complete. More than half of the 3 minute measurement time is spent on finding the precise solar position using the positional calibration algorithm shown in Figure 4.16. This algorithm provides more accurate solar tracking and more robustness (as it is less sensitive to slight alignment errors) at the expense of increased time between measurements. The benefits to implementing this algorithm far outweigh the drawbacks, as accurate solar tracking is essential.

The measurement station captures the data listed in Table 5.1 in each of the 4 positions:

Table 5.1: Details of Measured Parameters.

Measured Parameter	**Unit/Specification of Measurement**
Narrow FOV irradiance	W/m^2
Wide FOV irradiance	W/m^2
Narrow FOV spectral irradiance	$W/m^2/nm$
Wide FOV spectral irradiance	$W/m^2/nm$
Atmospheric ozone	Dobson unit
Aerosol optical depth	Dimensionless/no unit
Precipitable water vapor	mm
Humidity	%
Air pressure	kPa
Temperature	°C
Sky image	15.4 MP, 24-bit colour, .jpg format

Approximately 17.5 days worth of measurements can be stored on the microSD card installed in the Raspberry Pi. This is determined because on average, 800 MB worth of data is captured per day and the Raspberry Pi has a microSD card with 16 GB capacity of which approximately 14 GB is free. The Raspberry Pi model 3B officially supports

microSD cards with a maximum capacity of up to 32 GB. However, it is possible that a microSD card with up to 128 GB capacity is also recognized, but this depends on the model and manufacturer of the card. Data is retrieved from the Pi every few days, therefore, no additional storage space in the form of solid-state drives or a higher capacity microSD card is required.

Data is retrieved from the Pi using SSH (Secure Shell) with a laptop connected on the same local network. The login details for connecting to the local network and using SSH to gain access to the Raspberry Pi are shown in Table 5.2. The username and password of the Raspberry Pi are what was configured by default. These are not secure and should be changed by the future users of the station for added security. The key to the wireless network should also be changed for security by the future users of the station, as it is the same as the SSID and can be easily exploited.

Table 5.2: Details for SSH.

WiFi Router	
SSID	MeasurementStation
Key	MeasurementStation

Raspberry Pi	
IP Address	10.0.0.5
Port	22
Username	pi
Password	raspberry

5.5 Chapter Review

The measurement station was set up and tested on the roof of the Department of Electrical and Electronic Engineering at Stellenbosch University. This location offered a clear view of the sky, except during late afternoon when the buildings to the west would obstruct the view of the sun.

Sandbags were used to stabilise the station, as poles could not be driven into the roof for structural support. The process used to align the measurement station was discussed, and a detailed description of the assembly of the station was provided. The power and communications connections between all the devices were shown.

The pan/tilt unit was seen to struggle during tilt operation, so a spring was implemented in order to reduce the overall torque on the unit and improve its performance. A 20° wedge was placed between the pan/tilt unit and the platform to offset the tilt range from -20°–60° to 0°–80°, as this is more useful for this application. The SMP10 pyranometer is levelled with the SolarSIM-G spectral irradiance meter using an HDPE block. This was done so that one device does not influence the measurements of the other.

The configured measurement positions were described and motivated, along with the data captured in each position. The process to retrieve data from the station was discussed, and the details needed to interface with the station were provided.

The data collected by the measurement station is analysed in Chapter 6, and the performance of the system is evaluated.

Chapter 6

Station Evaluation and Data Analysis

6.1 Introduction

This chapter evaluates the performance of the measurement station to determine if it operates as designed and analyses some data collected by the station to determine how spectral irradiance is affected under different conditions.

The broadband irradiance measurements are evaluated by comparison to measurements made by an independent station nearby to determine if they are valid. The station is then misaligned, and its ability to accurately track the sun is assessed. The spectral irradiance measurements are evaluated by comparison to the reference spectrum to determine the correlation between them. Finally, the FOV of the pyrheliometer relative to the captured images is determined, and the camera performance is assessed. Analysis of the collected data shows the impact of different solar tracking methods on the received irradiance, and the variation of the solar spectrum under different conditions is also observed.

6.2 Evaluation of Measurement Station

6.2.1 Evaluation of Irradiance Measurements

The Southern African Universities Radiometric Network (SAURAN) is a network of radiometric measurement stations located at universities across South Africa [78], [79]. The data captured by SAURAN is publicly available. The radiometric measurement station named SUN is a part of SAURAN and is set up at the faculty of Engineering at Stellenbosch University. The irradiance data captured by the measurement station presented in this thesis can be validated using irradiance data captured by SUN, as both the stations are situated in close proximity to one another. It should be noted that the instruments on SUN have last been calibrated in 2016, while the instruments on the measurement station presented in this thesis were last calibrated towards the end of 2020.

The measurements shown in Figures 6.1 and 6.2 are taken on the 17^{th} of February 2021, which is a clear summers day. It should be noted that the data captured by SUN is taken in 1 minute intervals, while the measurement station records data once every 10 minutes. Consequently, the measured data is of a lower resolution than that of

SUN. Great care is taken in correctly aligning the measurement station to ensure that it accurately tracks the movement of the sun in the sky.

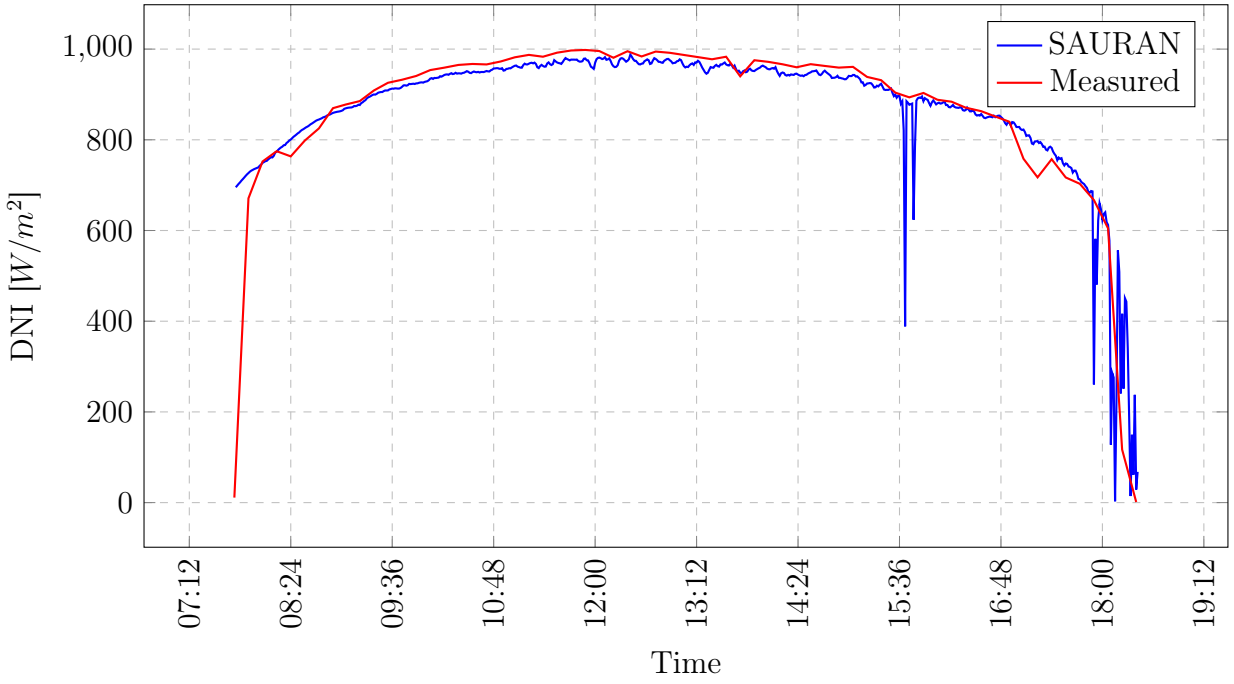

Figure 6.1: Comparison of Measured DNI with SAURAN DNI.

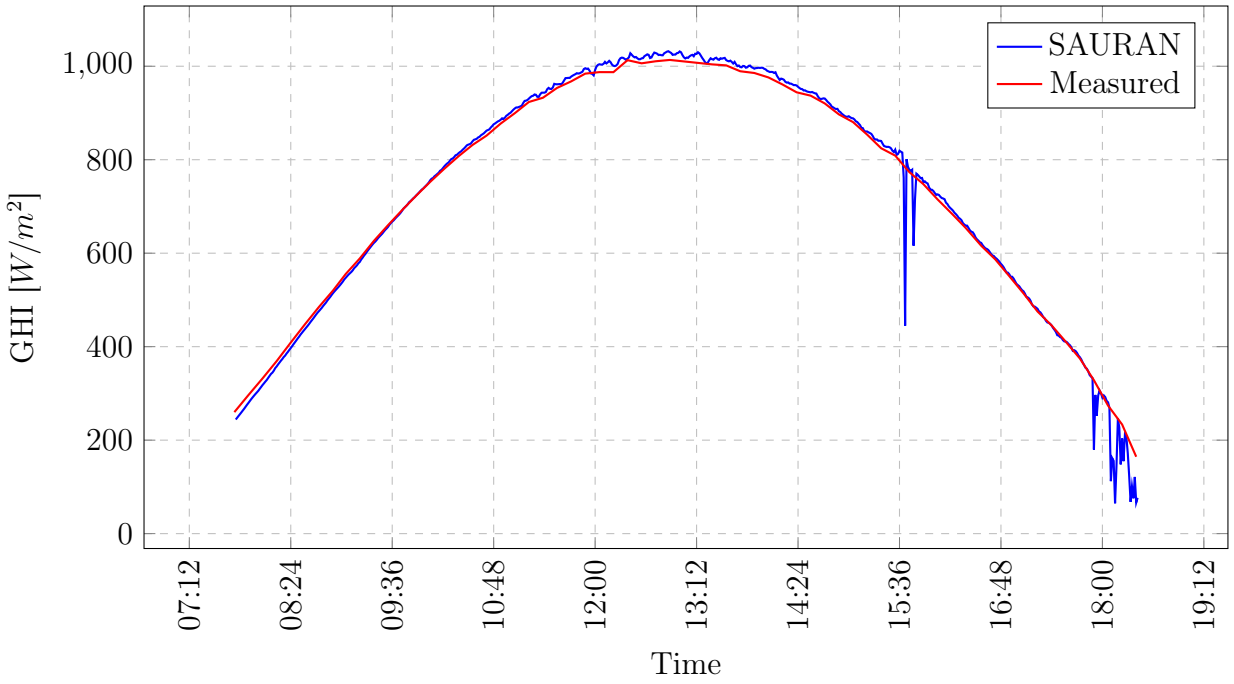

Figure 6.2: Comparison of Measured GHI with SAURAN GHI.

It is seen in Figure 6.1 that the measured DNI correlates very well with the DNI measured by the SAURAN SUN station. The reduced measurement frequency results in spikes in irradiance not being recorded by the measurement station. The station is able

to follow the sun for many hours in the day, as the measurements are captured in summer when the sun is higher up in the sky. The limited tilt range does not significantly affect the tracking ability in the summer.

Figure 6.2 shows the high correlation between the measured GHI and the GHI recorded by SAURAN. Once again, it is seen that the lower measurement frequency results in irradiance spikes not being recorded. However, the station can be configured to capture data more frequently if required. The correlation between the measured data and the SAURAN data shows that the station can measure irradiance to an acceptable standard.

6.2.2 Evaluation of Positional Calibration for Solar Tracking

The measurement station is set up and deliberately misaligned with true North in order to evaluate the performance of the positional calibration sequence. The positional calibration sequence is used to fine tune the ability of the measurement station to accurately track the sun. The DNI measurements with and without positional calibration are compared with DNI measurements from the SAURAN SUN station in Figure 6.3. The data is captured on the 5^{th} of August 2021 between 10:00 and 16:30.

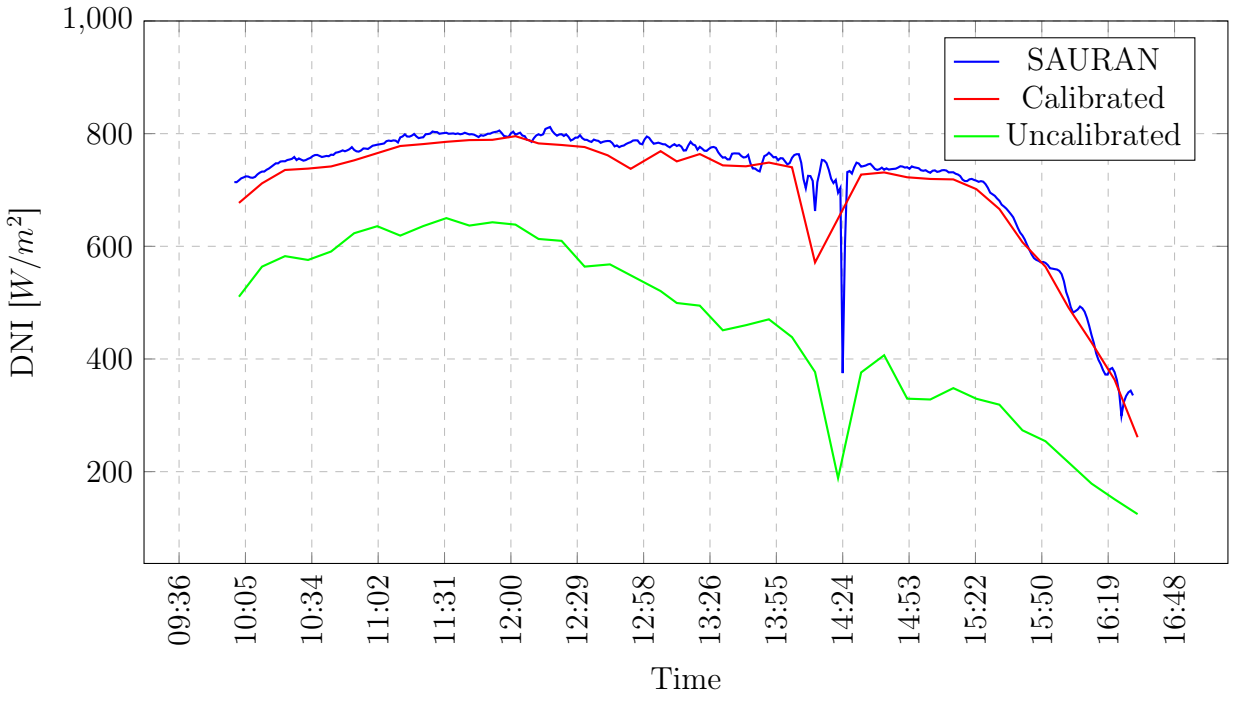

Figure 6.3: Evaluation of Positional Calibration Sequence.

It is seen that the DNI measurements made while using the positional calibration very closely follow the DNI measurements made by the SAURAN SUN station. However, the reduced measurement frequency of one measurement per 10 minutes in comparison to the frequency of one measurement per minute used by SAURAN results in a loss of fine details. The measurements made without using positional calibration are significantly affected by the misalignment of the station and are not reliable. This validates that the positional calibration sequence is necessary and achieves its goal to aid in accurately

tracking the sun. It adds good disturbance rejection to the system by reducing the sensitivity of the station to being perfectly aligned.

6.2.3 Evaluation of Spectral Irradiance Measurements

The standard reference solar spectra have been developed to allow for the performance of various PV devices in different locations to be evaluated and compared. The American Society for Testing and Materials (ASTM) G173 reference spectra describe the spectral irradiance received on the surface of the earth under specific atmospheric conditions. These atmospheric conditions include a total column water vapor equivalent of 1.42 cm and a total column ozone equivalent of 0.34 cm. The ASTM G173 spectrum is measured at a solar elevation angle 41.81° for an air mass factor of 1.5. [11]

The comparison between the direct circumsolar and the global tilted spectral irradiance measurements and the ASTM G-173 reference spectra is shown in Figure 6.4 and Figure 6.5 respectively. These spectra were captured on February 17^{th} 2021 at 09:44. The solar elevation angle at this time was 41°, resulting in an air mass factor of 1.52 in contrast to the air mass factor of 1.5 used in the reference spectra. The atmospheric water vapor is determined to be 1.403 cm and the atmospheric ozone is determined to be 0.293 cm in contrast to 1.42 cm of water vapor and 0.34 cm of ozone in the reference spectra. The ambient temperature was 32.3 °C, the air pressure was 99.4 kPa and the humidity was 29.8% as the measurements were made.

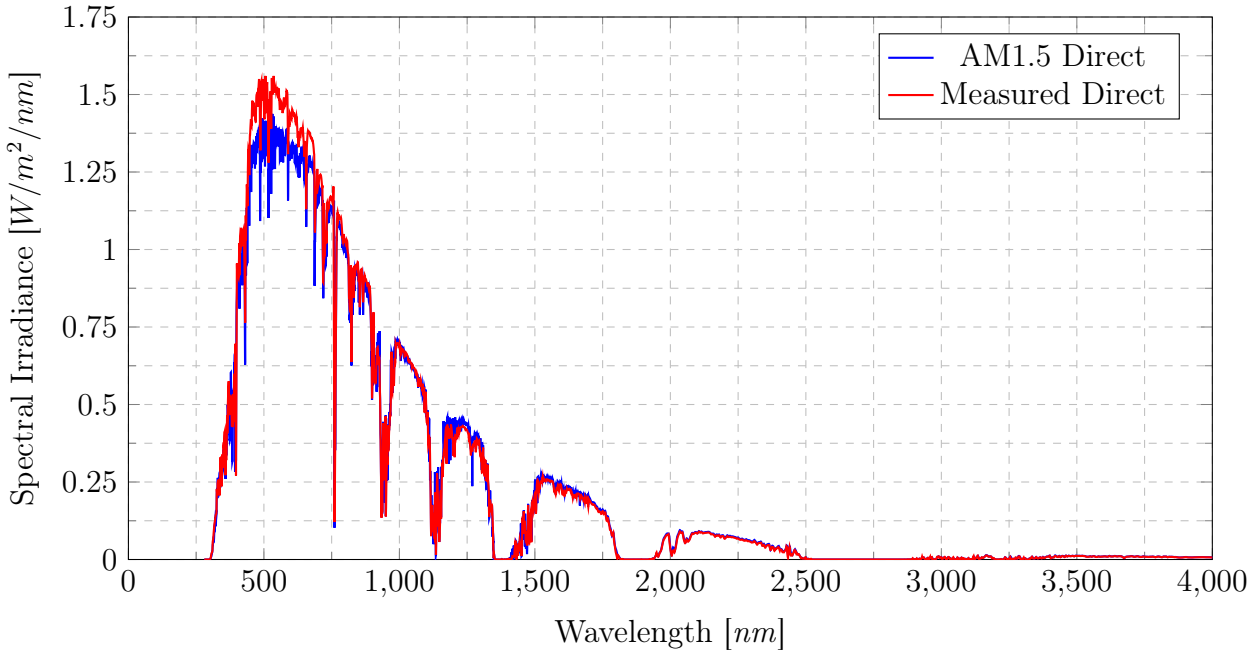

Figure 6.4: Measured Direct Circumsolar Spectrum Compared to ASTM-G-173-03 AM1.5 Direct Spectrum.

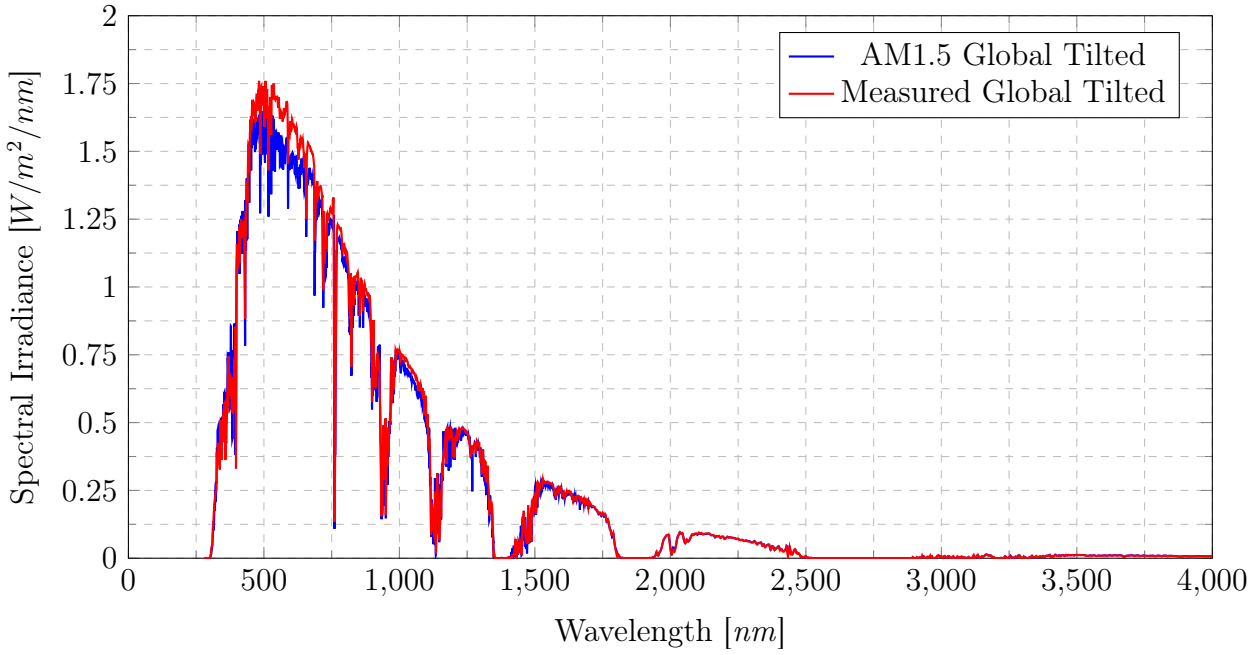

Figure 6.5: Measured Gloabal Tilted Spectrum Compared to ASTM-G-173-03 AM1.5 Global Tilted Spectrum.

The measured direct circumsolar and global tilted spectral irradiances are both marginally higher than the reference spectra. This is more noticeable at shorter wavelengths. Overall, the measured spectra correlate very well to the ASTM G-173 reference spectra. The direct spectral irradiance has a correlation factor of 0.9984 and the global spectral irradiance has a correlation factor of 0.9988 to the reference spectra. The strong correlation between the measured spectra and reference spectra under similar conditions helps to validate the operation of the measurement station.

6.2.4 Relating Pyrheliometer Field of View to Captured Images

The method that is used to relate field of view of the pyrheliometer to the images taken of the sky is described in this section. The measurement station is configured to align with the azimuth angle of the sun at solar noon on August 3^{rd} 2021. The tilt angle is continually adjusted for optimal tilt. DNI measurements and photos are captured in 1 minute intervals as the sun moves across the field of view of the pyrheliometer. The resultant plot of the measured DNI is shown in Figure 6.6.

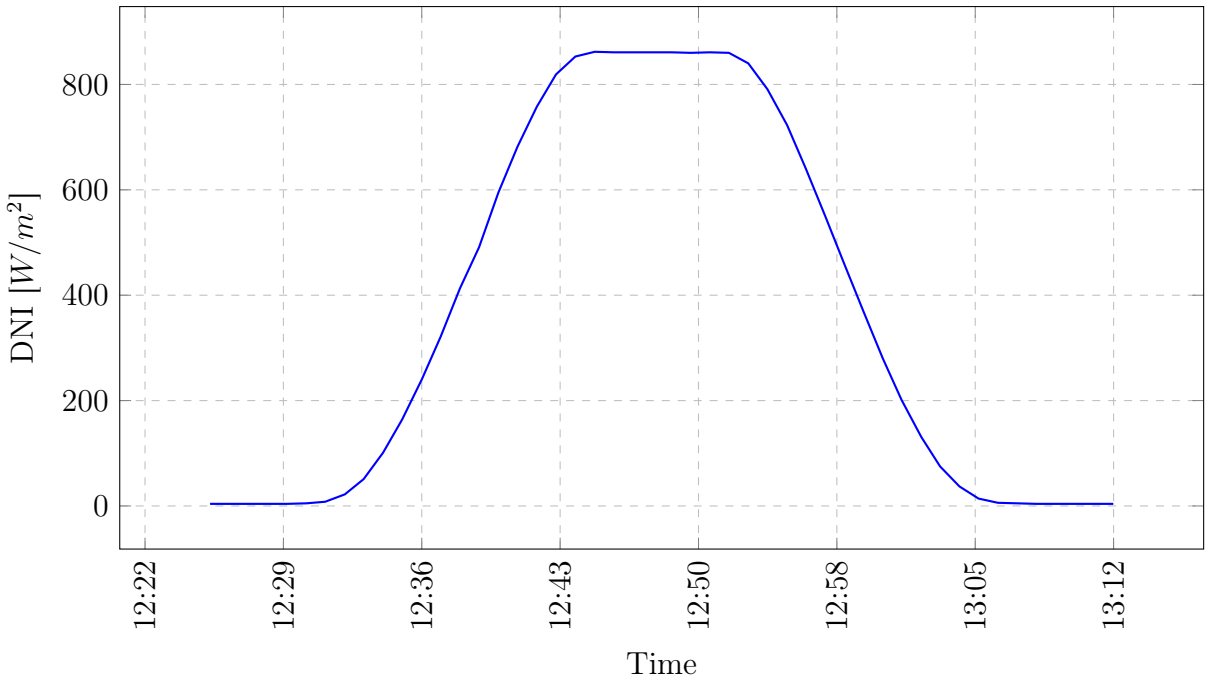

Figure 6.6: Measured DNI as Sun Moves Across Pyrheliometer FOV.

From Figure 6.6, it is seen that the sun is fully within the field of view of the pyrheliometer between 12:45 and 12:52. The corresponding images taken at these times are shown in Figure 6.7. Black rings are overlaid on the solar disks in these images to help distinguish the solar disk from the background.

(a) Sun in Frame at 12:45.

(b) Sun in Frame at 12:52.

Figure 6.7: Sun Moving Across Pyrheliometer Field of View.

These two images are superimposed on each other, resulting in the image shown in Figure 6.8. The distance between the centres of the two rings is measured to account for 75 pixels of the 4800 pixel wide image. Therefore, it is concluded that the field of view of the pyrheliometer consists of approximately 75 pixels in the captured images. It is important to note that this value may change based on the season, as the distance between the earth and the sun changes.

Figure 6.8: Merged Images of Sun at Maximum DNI Readings.

6.2.5 Camera Performance in Winter

Figure 6.9 shows dew on the lens of the camera. This is observed to only occur during winter when the ambient temperature is very low. The dew usually fully evaporates from the lens by the time the measurement station completes its third measurement set of the day and the issue is resolved. A hydrophobic coating applied to the lens may reduce or eliminate the problem.

Figure 6.9: Dew on Camera Lens on a Cold Morning.

6.3 Data Analysis

6.3.1 Global Irradiance Measured at Different Positions

Figure 6.10 shows the global irradiance measured in the 4 currently configured measurement positions of the station on the 5^{th} of August 2021. The "Direct" measurement position aligns the station with the azimuth angle of the sun, and the tilt angle of the station tracks the zenith angle of the sun. The "Optimal Tilt" position aligns the station true North, and the tilt angle of the station tracks the zenith angle of the sun. The "Fixed Tilt" position aligns the station with true North, with a fixed tilt angle of 30°. This is the angle at which most PV panels are tilted in South Africa, as previously discussed. The "Horizontal" position has the tilt angle set to 0° to capture GHI measurements.

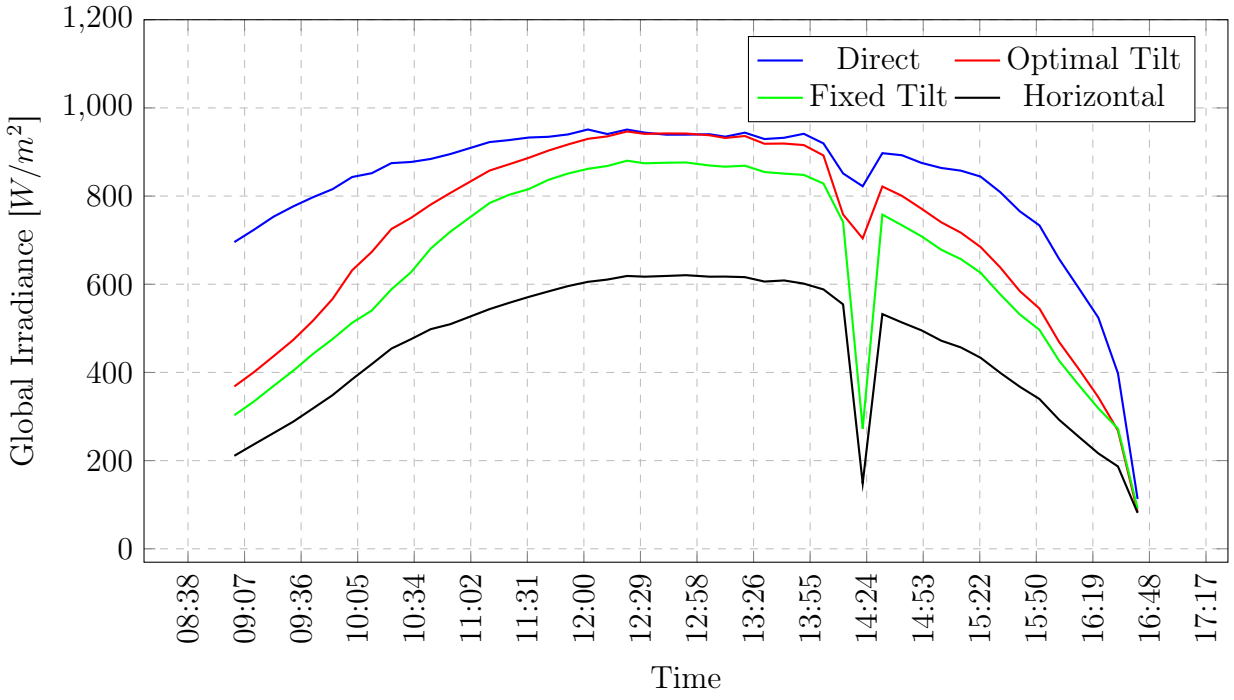

Figure 6.10: Global Irradiance in Different Measurement Positions.

Using the data plotted during the 5^{th} of August 2021 in Figure 6.10, it is determined that a PV panel placed in the "Direct" measurement position (i.e. mounted on a double-axis tracker) receives approximately 28% more irradiance than a panel which faces North with a fixed tilt of 30°. A PV panel with optimal tilt (i.e. single-axis tracking) receives approximately 12% more irradiance than a North facing panel with fixed 30° tilt. A panel laying horizontally receives 29% less irradiance through the day than a fixed tilt panel.

As mentioned in Chapter 2.6.3, the internal series resistance of a PV module decreases as the received irradiance is increased. This improves the efficiency of the module. Therefore, implementing tracking systems for solar panels increases their efficiency by increasing the irradiance they receive.

Figure 6.11 shows the movement of clouds past the sun, causing the dip in irradiance observed in Figure 6.10 at approximately 14:24.

(a) Sky on 05/08/2021 at 14:02.

(b) Sky on 05/08/2021 at 14:12.

(c) Sky on 05/08/2021 at 14:22.

(d) Sky on 05/08/2021 at 14:32.

Figure 6.11: Movement of Clouds Past the Sun Causing Dip in Irradiance

6.3.2 Spectral Irradiance at Different Times of Day

A comparison of the direct circumsolar and global tilted spectra measured at different times on February 17^{th} 2021 is shown in Figures 6.12 and 6.13 respectively. The times at which the spectra were measured, along with the corresponding atmospheric parameters are shown in Table 6.1.

Table 6.1: Atmospheric Conditions.

Time	**Direct Irradiance**	**Temp.**	**Air Pressure**	**Humidity**	**Air Mass**	**Water Vapor**	**Ozone**
09:44	932 W/^{2}	29.36 °C	99.47 kPa	29.9 %	1.52	1.403 cm	0.293 cm
12:54	991 W/m^2	33.97 °C	99.45 kPa	22.2 %	1.08	1.45 cm	0.311 cm
16:14	884 W/m^2	27.93 °C	99.52 kPa	40.8 %	1.54	1.749 cm	0.324 cm

It is seen that both the direct circumsolar and the global tilted spectral irradiance is higher at 12:54. This is as expected, because this is at solar noon where the air mass factor is approximately 1. The air mass at 09:44 and 16:14 is higher at approximately 1.5. The spectra at 09:44 and 16:14 are very similar, with 99.99% correlation between them.

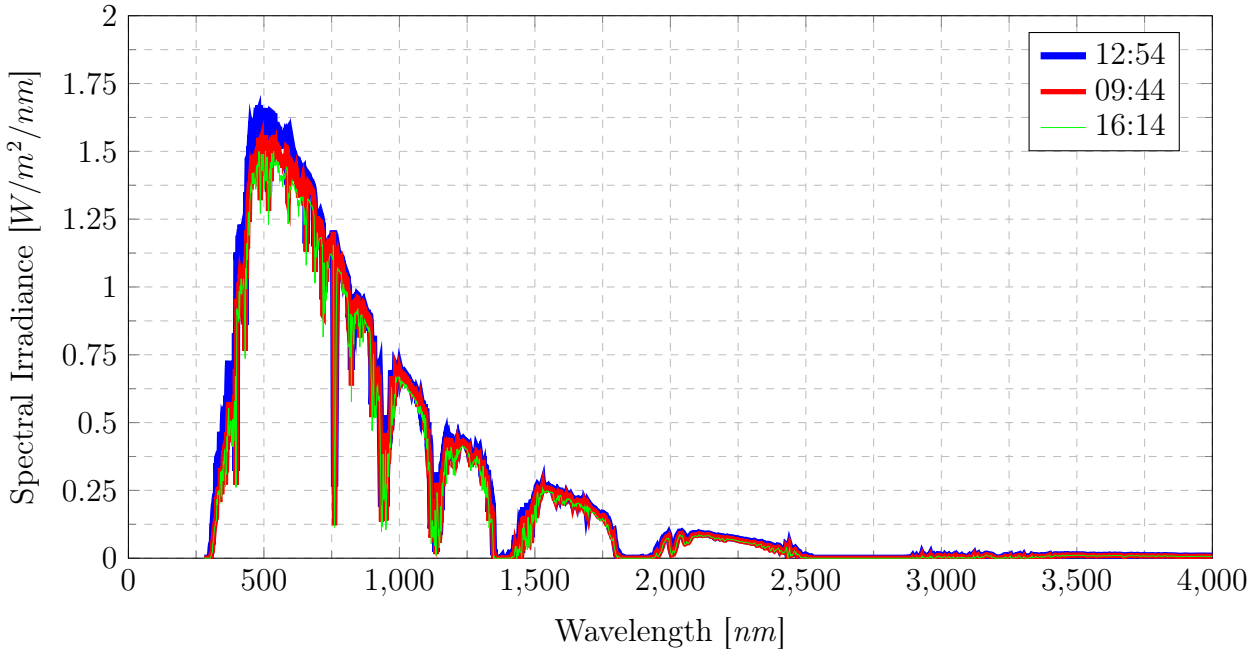

Figure 6.12: Direct Circumsolar Spectral Irradiance at Different Times.

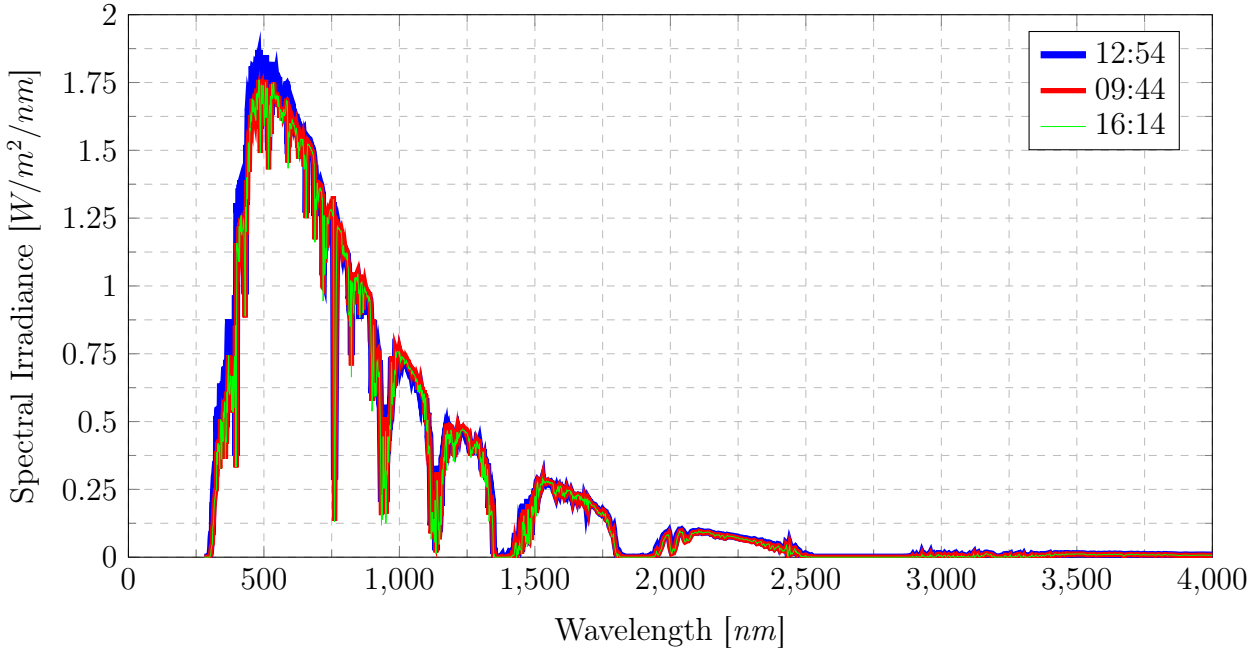

Figure 6.13: Global Tilted Spectral Irradiance at Different Times.

6.3.3 Spectral Irradiance in Different Seasons

A comparison between spectral irradiance measurements during summer and winter are shown in Figure 6.14 and Figure 6.16. The summer spectrum was measured on the 17^{th} of February 2021 at 09:44 and the winter spectrum was measured on the 5^{th} of August 2021 at 12:43. The corresponding measured atmospheric parameters are shown in Table 6.2.

Table 6.2: Atmospheric Conditions.

Date	Direct Irradiance	Temp.	Air Pressure	Humidity	Air Mass	Water Vapor	Ozone
17/02	932 W/m^2	29.36 °C	99.47 kPa	29.9 %	1.52	1.403 cm	0.293 cm
05/08	762 W/m^2	22.27 °C	100.8 kPa	42.2 %	1.58	1.528 cm	0.391 cm

In Figure 6.14, it is seen that the magnitude of the direct circumsolar spectral irradiance is significantly lower across all wavelengths in the winter than it is in the summer. This happens despite the measurements being taken at similar air mass factors and atmospheric conditions.

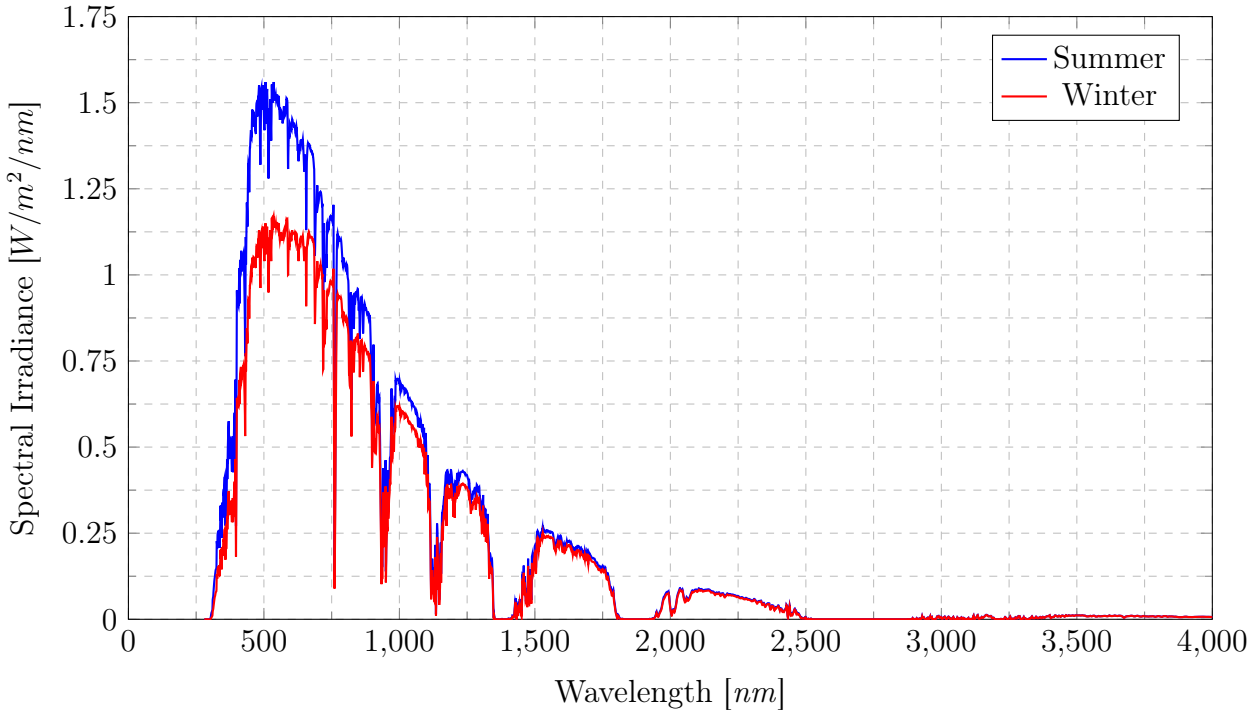

Figure 6.14: Direct Spectral Irradiance in Different Seasons.

The normalised direct spectral irradiance measurements are shown in Figure 6.15. It is seen that there is more relative power in the longer wavelengths during winter than during summer. Consequently, the solar spectrum appears to be red-shifted in the winter and blue-shifted in summer.

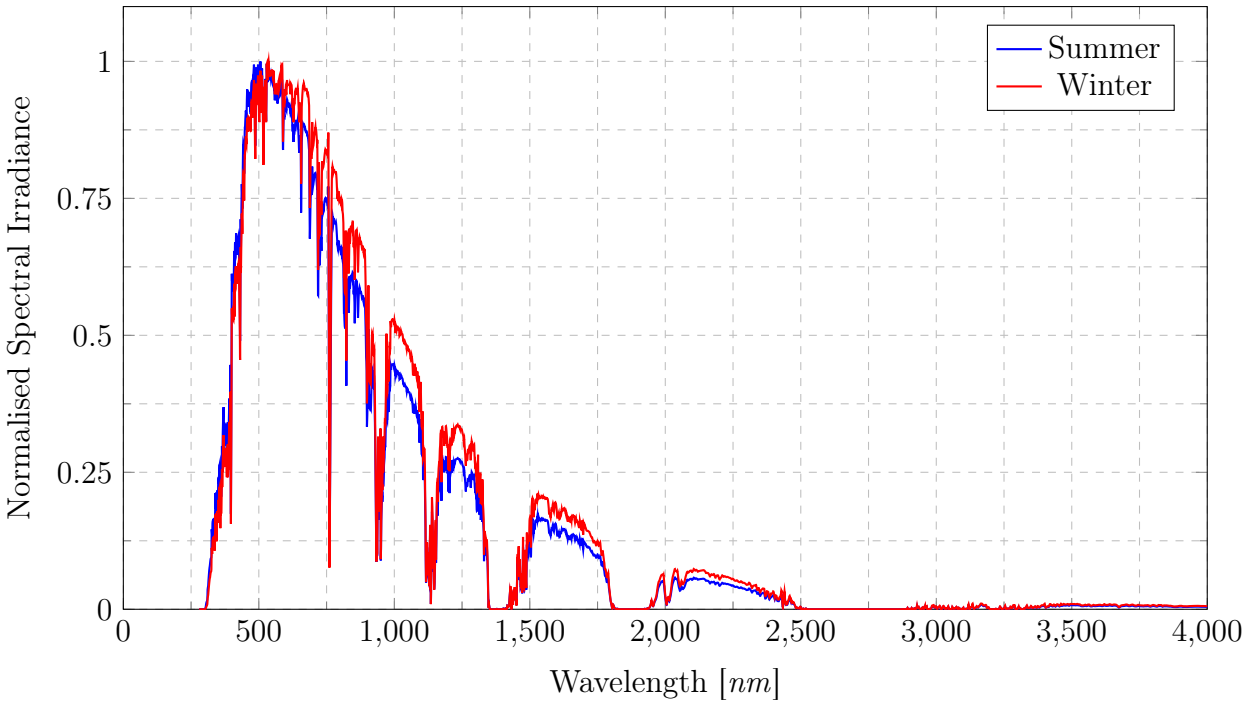

Figure 6.15: Normalised Direct Spectral Irradiance in Different Seasons.

As with the direct spectral irradiance measurements, it is seen in Figure 6.16 that the magnitude of the global tilted spectral irradiance is also lower in the winter compared to the summer across all wavelengths.

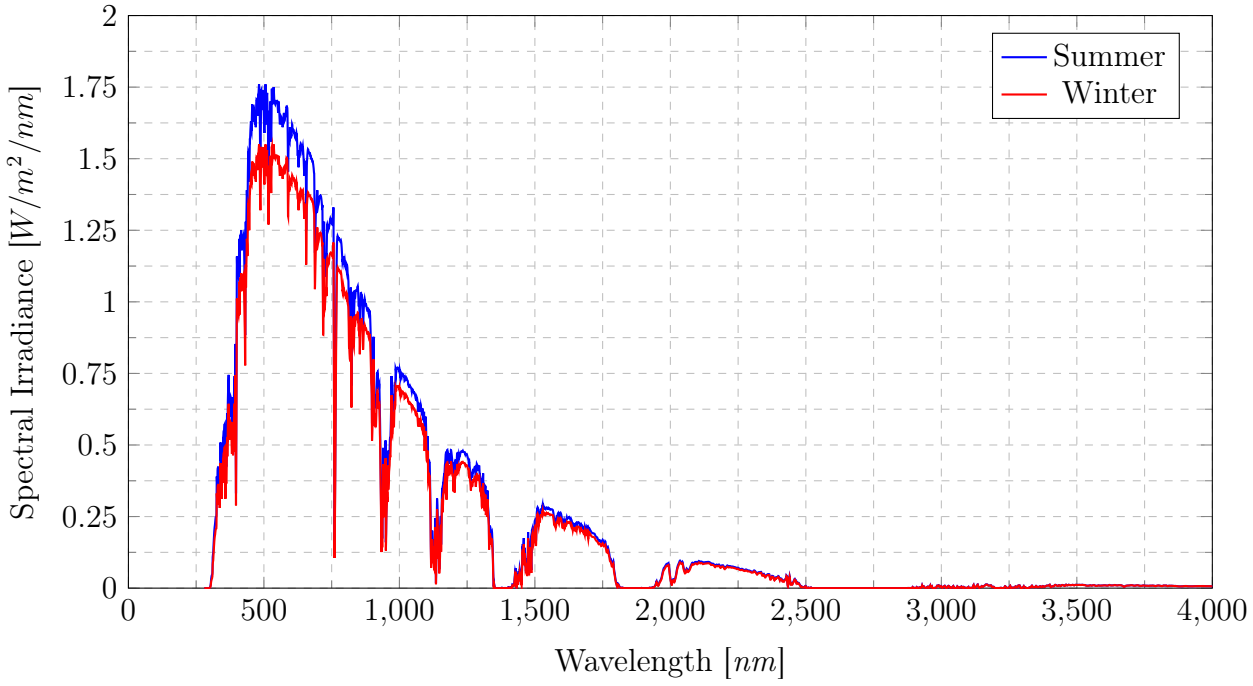

Figure 6.16: Global Spectral Irradiance in Different Seasons.

The normalised global tilted spectral irradiance measurements are shown in Figure 6.17. Again, it appears that the spectrum is red-shifted during the winter and blue-shifted

during the summer. However, this shift is less noticeable in the global tilted spectrum compared to the direct spectrum.

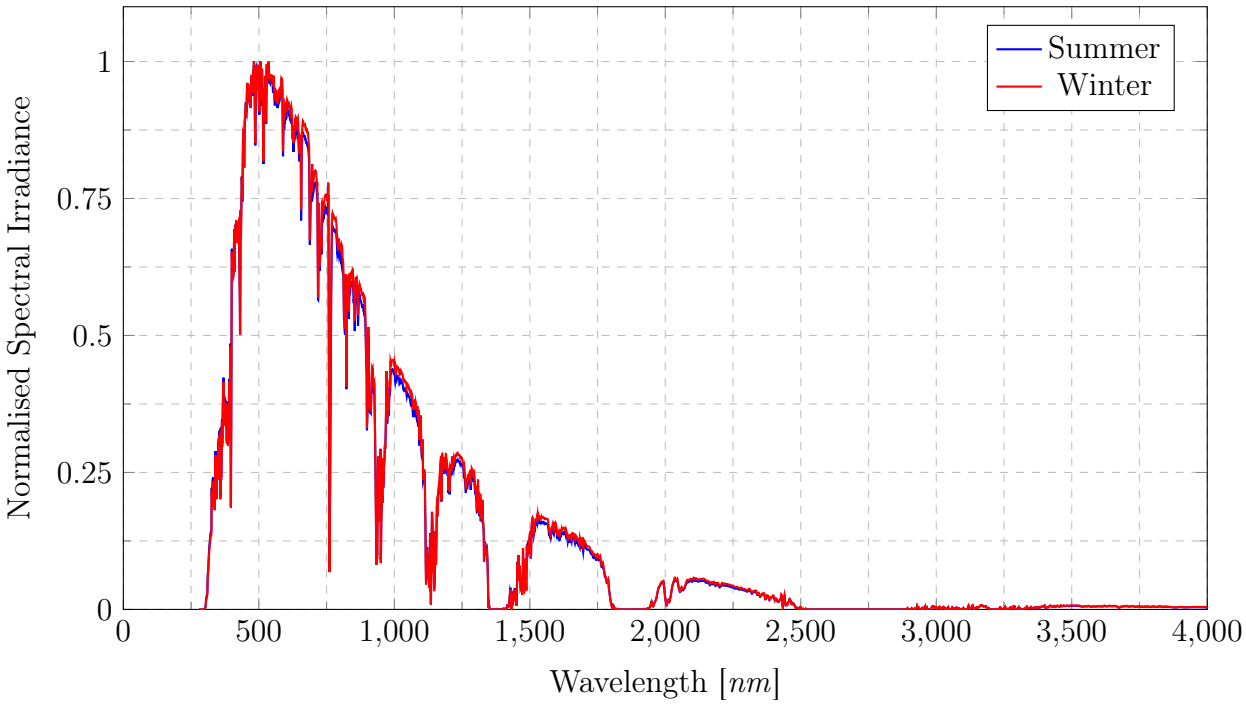

Figure 6.17: Normalised Global Spectral Irradiance in Different Seasons.

The percent decrease in the magnitude of the solar spectra from summer to winter is shown in Figure 6.18. It is seen that both the direct circumsolar and global tilted spectrum are affected in a similar way, with longer wavelengths being attenuated more consistently.

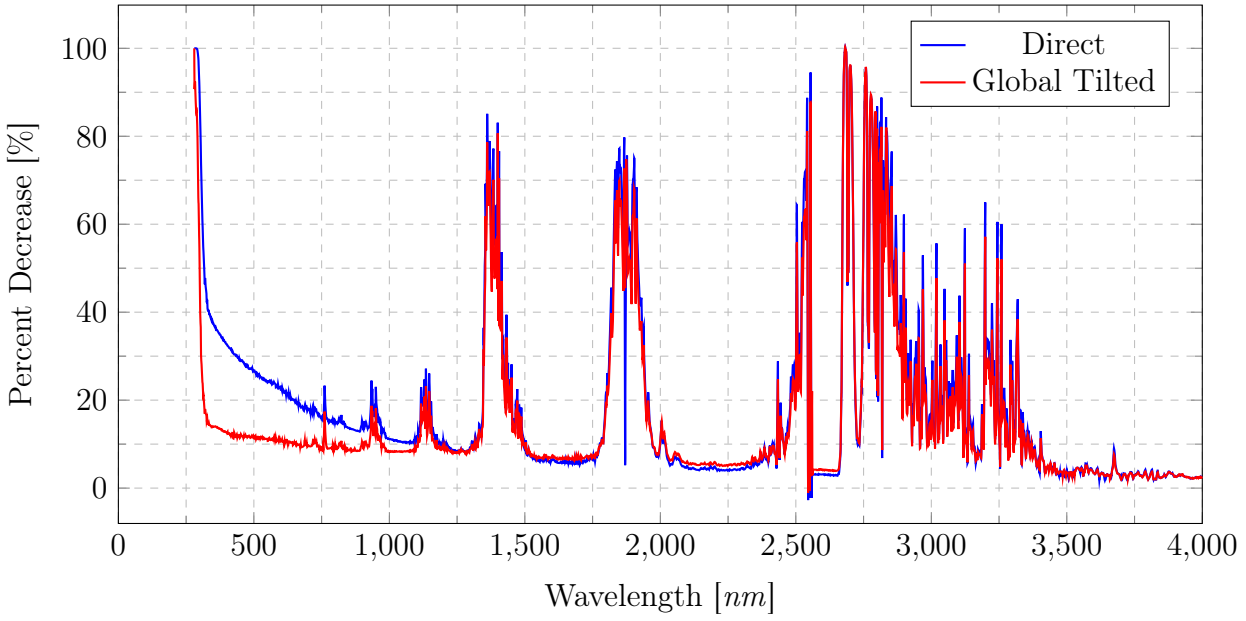

Figure 6.18: Percent Decrease in Spectral Irradiance from Summer to Winter.

The percent decrease in the normalised spectra from summer to winter is shown in Figure 6.19. It is seen that, generally, the relative power increases in longer wavelengths from summer to winter. This helps to illustrate the spectral shift.

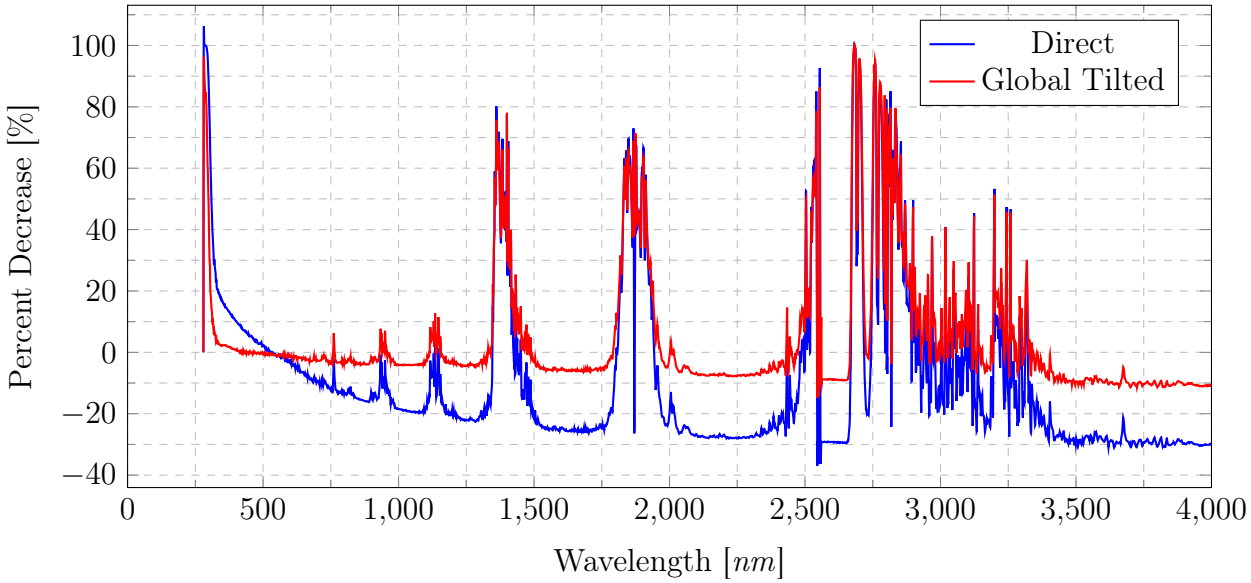

Figure 6.19: Percent Decrease in Normalised Spectral Irradiance from Summer to Winter.

The observed blue-shift of the solar spectrum in summer and red-shift in winter concurs with the findings of Schweiger and Hermann [44], as discussed in Chapter 2.6.3. However, the observed spectral shift does not seem to be significant in this case. It seems unlikely that power output in the different seasons could be optimised with the use of PV panels made from different PV technologies.

The sun is closer to the earth in the summer and farther away from the earth in the winter in the Southern Hemisphere. Figure 6.20 shows the images of the sun in the sky during summer and winter. In the summer, the sun appears approximately 194% larger in the photo compared to the winter. This due to the sun being closer to the earth in the summer than in the winter, as well as the effects of atmospheric lensing. These images were captured at the same time as the spectral measurements presented above.

(a) Image of Sun in Summer.

(b) Image of Sun in Winter.

Figure 6.20: Image of Sun in the Sky in Different Seasons.

6.3.4 Spectral Irradiance in Different Cloud Conditions

6.3.4.1 Partly Cloudy and Clear Conditions

The movement of a cloud across the solar disk is shown in Figure 6.21. These photographs and the corresponding spectral measurements allow for the observation of the impact of different cloud conditions on the solar spectrum. The photo with clouds surrounding the sun was taken on February 12^{th} 2021 at 09:24. The photo after the clouds had moved away was taken 20 minutes later at 09:44.

(a) Sky on 12/02/2021 at 09:24. (b) Sky on 12/02/2021 at 09:44.

Figure 6.21: Movement of Clouds Past the Sun.

The direct spectral irradiance measurements are shown in Figure 6.22. It is seen that the magnitude of the direct spectral irradiance is attenuated across all wavelengths by the clouds moving in front of the sun.

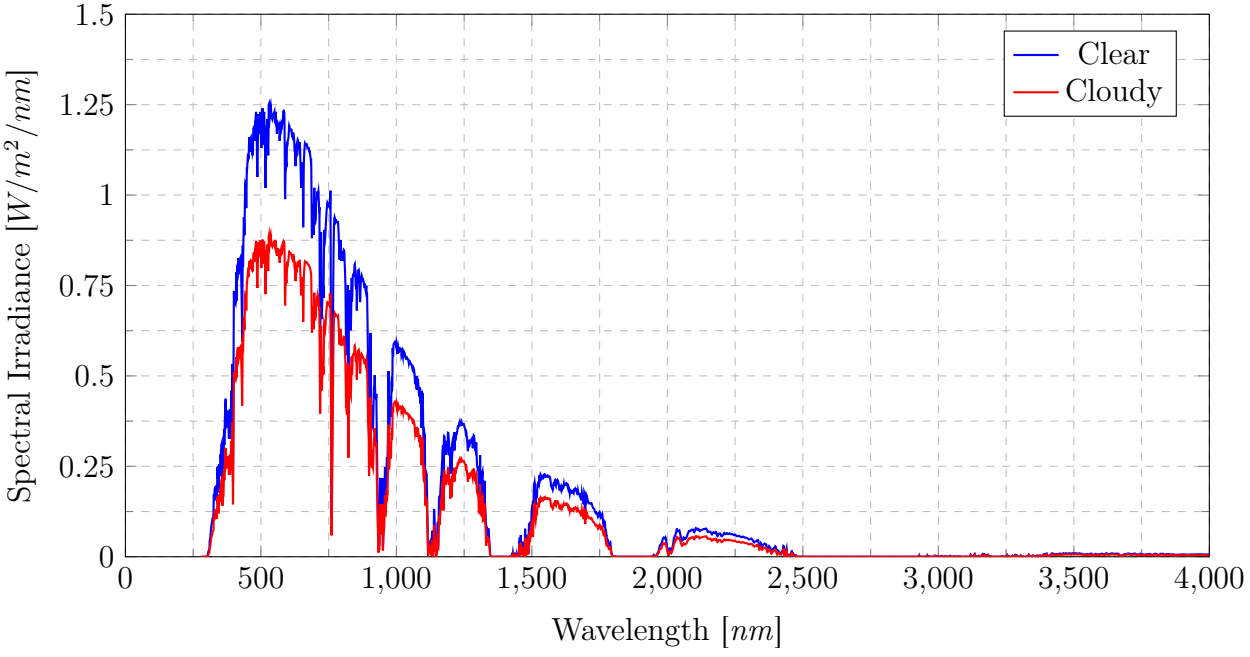

Figure 6.22: Direct Spectral Irradiance under Clear and Cloudy Conditions.

The normalised direct spectral irradiance measurements are shown in Figure 6.23. It is seen that the spectral distribution of the direct irradiance does not change noticeably under this condition. This implies that all the wavelengths are attenuated similarly.

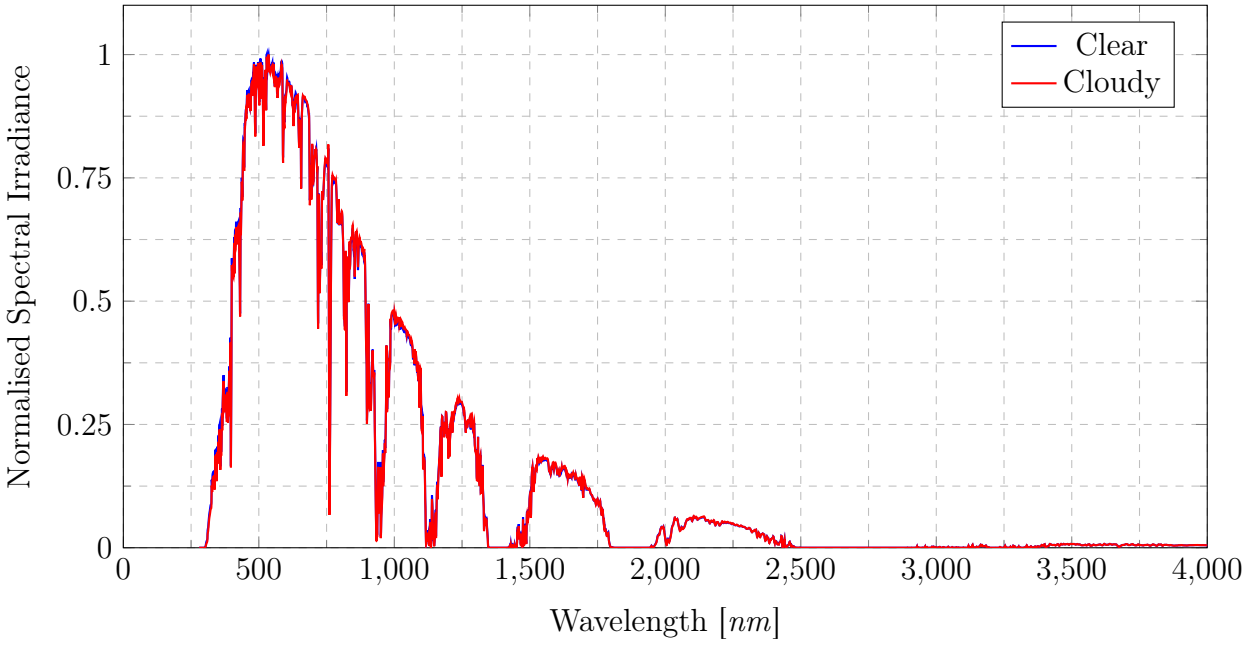

Figure 6.23: Normalised Direct Spectral Irradiance under Clear and Cloudy Conditions.

The global tilted spectral irradiance measurements are shown in Figure 6.24. It is seen that the magnitude of the global spectral irradiance is also attenuated by the clouds.

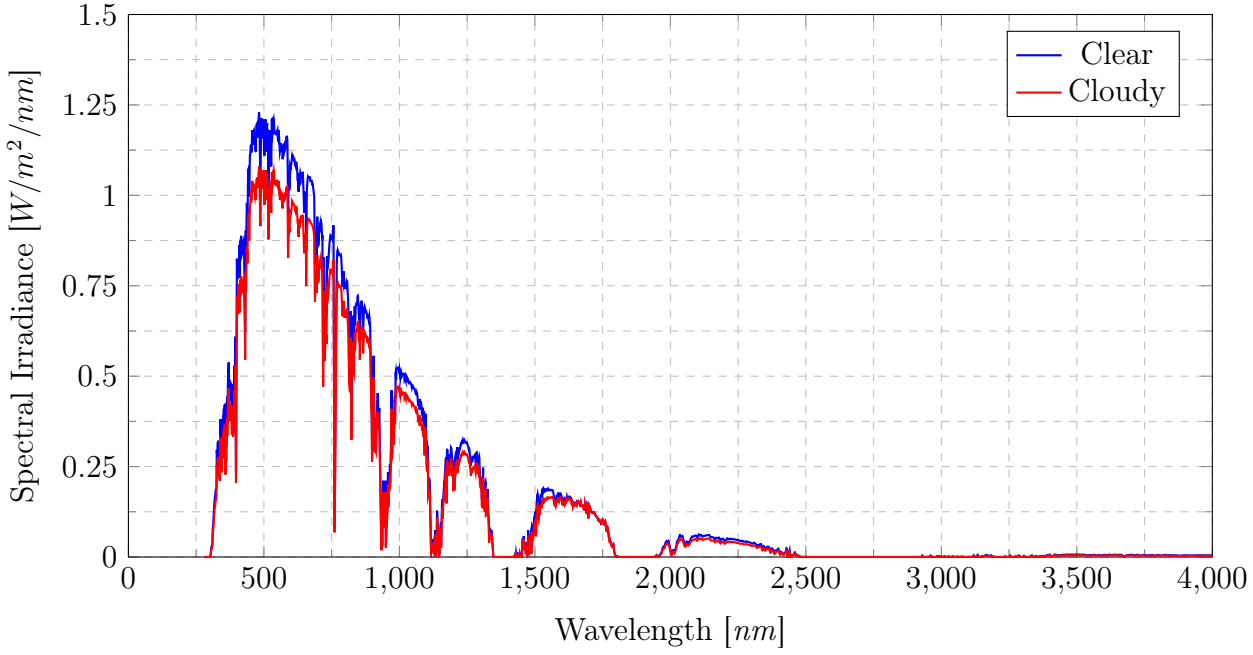

Figure 6.24: Global Tilted Spectral Irradiance under Clear and Cloudy Conditions.

The normalised global tilted spectral irradiance is shown in Figure 6.25. Again, it is seen that the spectral distribution of the irradiance does not change significantly. However, the distribution does change more than it did for the direct measurements.

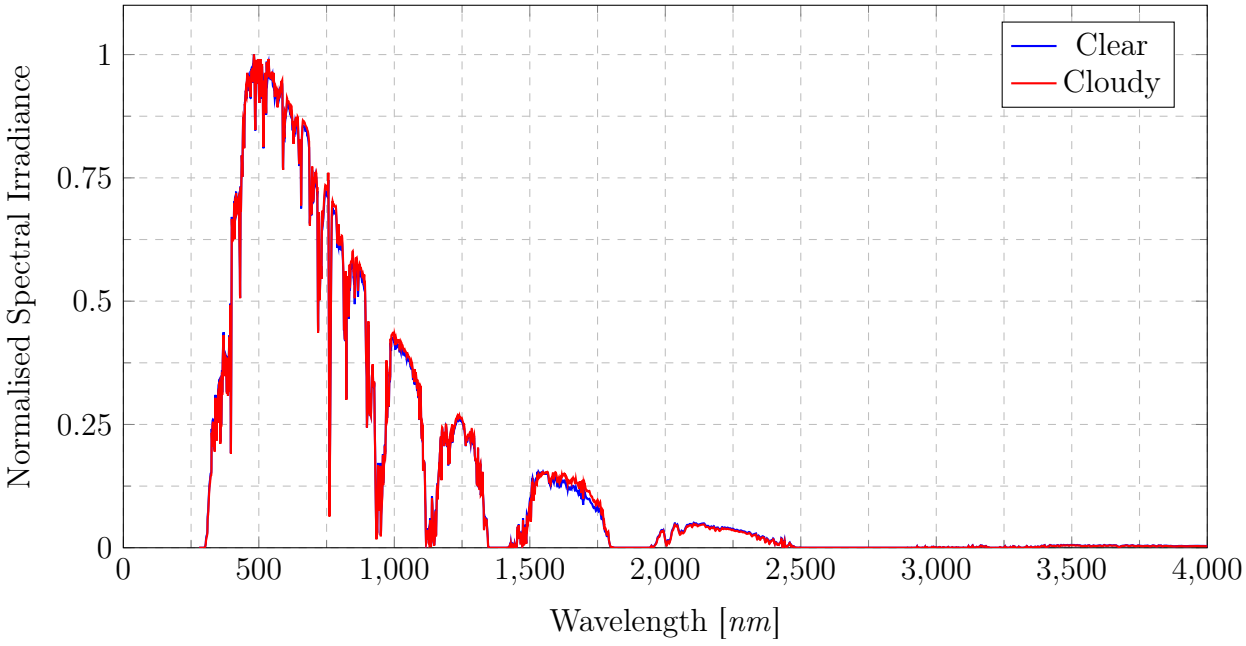

Figure 6.25: Normalised Global Spectral Irradiance under Clear and Cloudy Conditions.

The decrease in the magnitude of the spectral irradiance across different wavelengths caused by clouds is shown in Figure 6.26. It is seen that the direct spectral irradiance is more highly attenuated across all wavelengths than the global tilted spectral irradiance. It is also seen that the power in some wavelengths is actually boosted, and not attenuated, in the case of global tilted irradiance under this cloud condition.

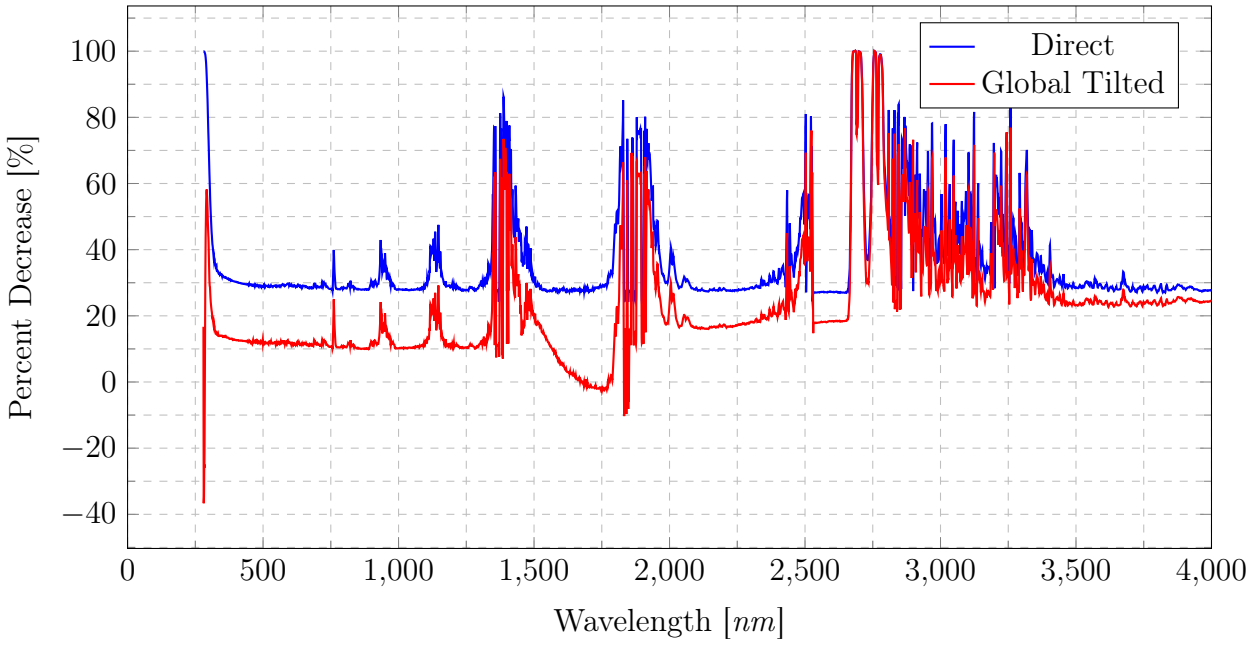

Figure 6.26: Percent Decrease in Spectral Irradiance Caused by Moving Clouds.

The percent decrease in the normalised spectra is shown in Figure 6.27. While most wavelengths are attenuated, it is interesting to note the increase in relative power in the wavelengths from approximately 1600 nm to 1800 nm in the global tilted spectrum.

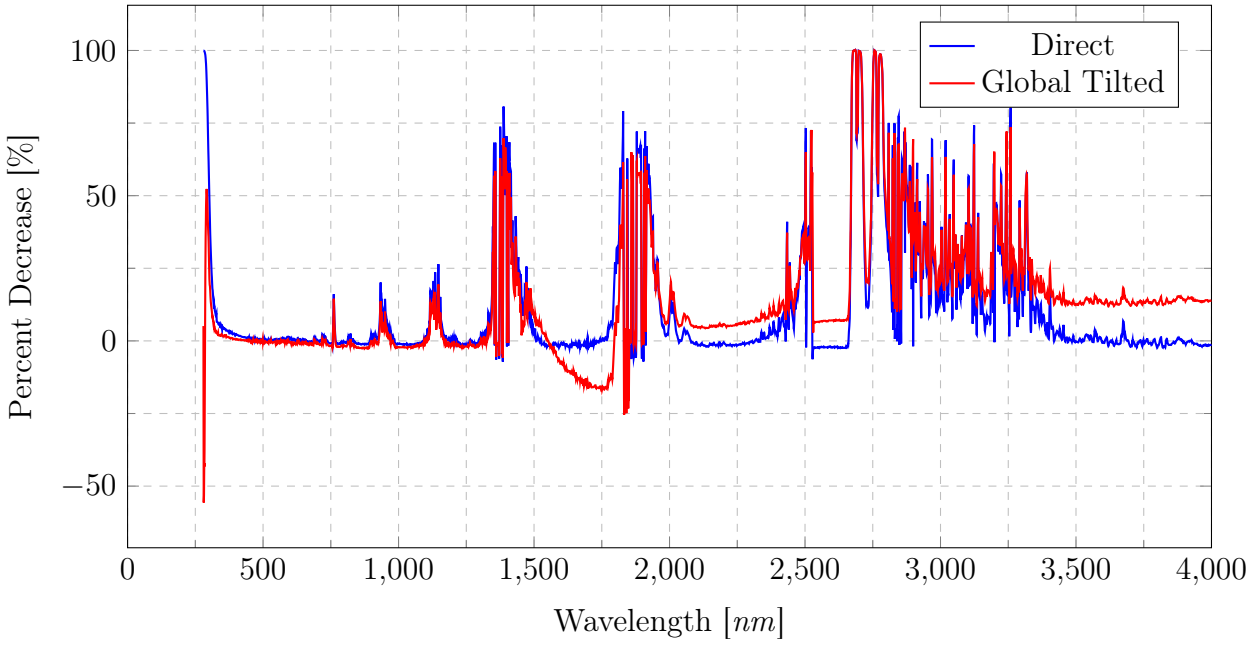

Figure 6.27: Percent Decrease in Normalised Spectral Irradiance Caused by Moving Clouds.

The increase in the power of certain wavelengths, as shown in Figure 6.26 and Figure 6.27 is likely caused by reflections. These wavelengths are in the infra-red range, and infra-red light is reflected more easily than light of a shorter wavelength. The albedo of the earth causes these wavelengths to be reflected from the surface of the earth towards the sky. Some of this radiation is absorbed by clouds and gas molecules, such as carbon dioxide and water vapor, in the atmosphere while some radiation is reflected back towards the earth. The combination of the radiation coming from the sun and the reflected radiation results in the observed power increase of these wavelengths. The fact that the power increase is only seen in the global-tilted spectrum, and not in the direct spectrum, further validates that reflections are responsible - as reflected radiation would not easily influence measurements taken with a narrow field-of-view sensor.

6.3.4.2 Overcast and Clear Conditions

The solar spectral irradiance measured on a fully overcast day is compared to that measured on a clear day in order to further understand the impact of clouds on the solar spectrum. Figure 6.28 shows the photos taken of the sky on the overcast and clear days when the spectral measurements were recorded. The overcast day was on February 14^{th} 2021 and the clear day was 3 days later on February 17^{th} 2021. The measurements were recorded at 09:44 on the respective days, with the air mass factor being approximately 1.52.

At the time of the measurements on the 14^{th} of February, the temperature was 22.27 °C, the air pressure was 99.72 kPa and the humidity was 70.7%. At the time of the

measurements on the 17^{th} of February, the temperature was 29.36 °C, the air pressure was 99.47 kPa and the humidity was 29.9%.

(a) Overcast Day on 14/02/2021. (b) Clear Day on 17/02/2021.

Figure 6.28: Images of Sky on Clear and Overcast Days

It is seen in Figure 6.29 that the magnitude of the spectral irradiance is heavily attenuated across all wavelengths on an overcast day. The attenuation is more significant than on a partly cloudy day as previously seen.

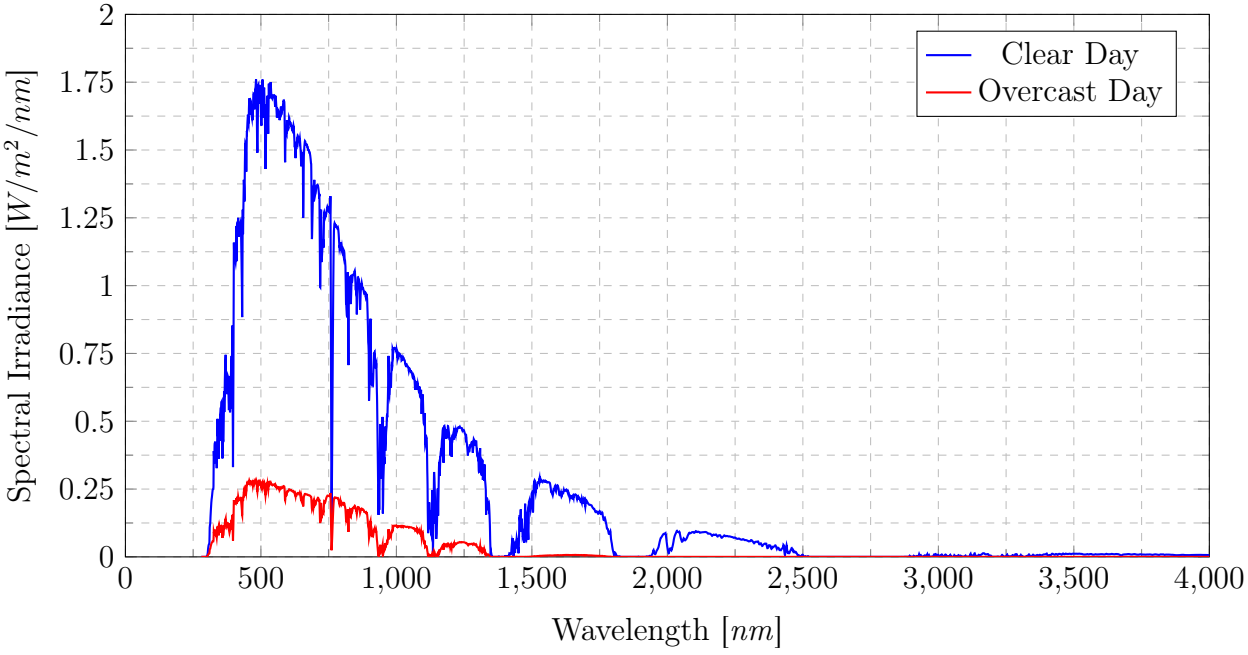

Figure 6.29: Global Tilted Spectrum on Clear and on Overcast Days.

The normalised global tilted spectral irradiance measurements are shown in Figure 6.30. It is seen that the relative power at shorter wavelengths is increased, while the relative power is significantly attenuated at longer wavelengths. It seems that the spectrum is blue-shifted under overcast conditions in comparison to clear conditions.

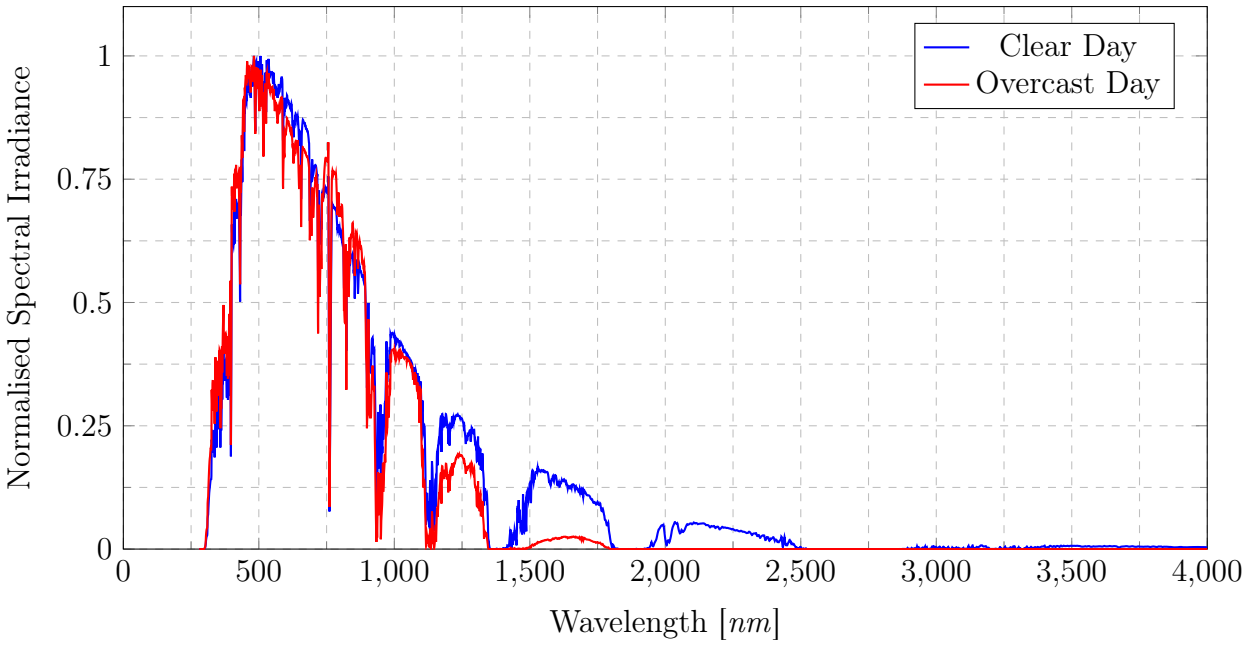

Figure 6.30: Normalised Global Tilted Spectrum on Clear and on Overcast Days.

In Figure 6.31, it is shown that the spectral irradiance is attenuated less at shorter wavelengths and almost completely attenuated at wavelengths longer than approximately 1800 nm.

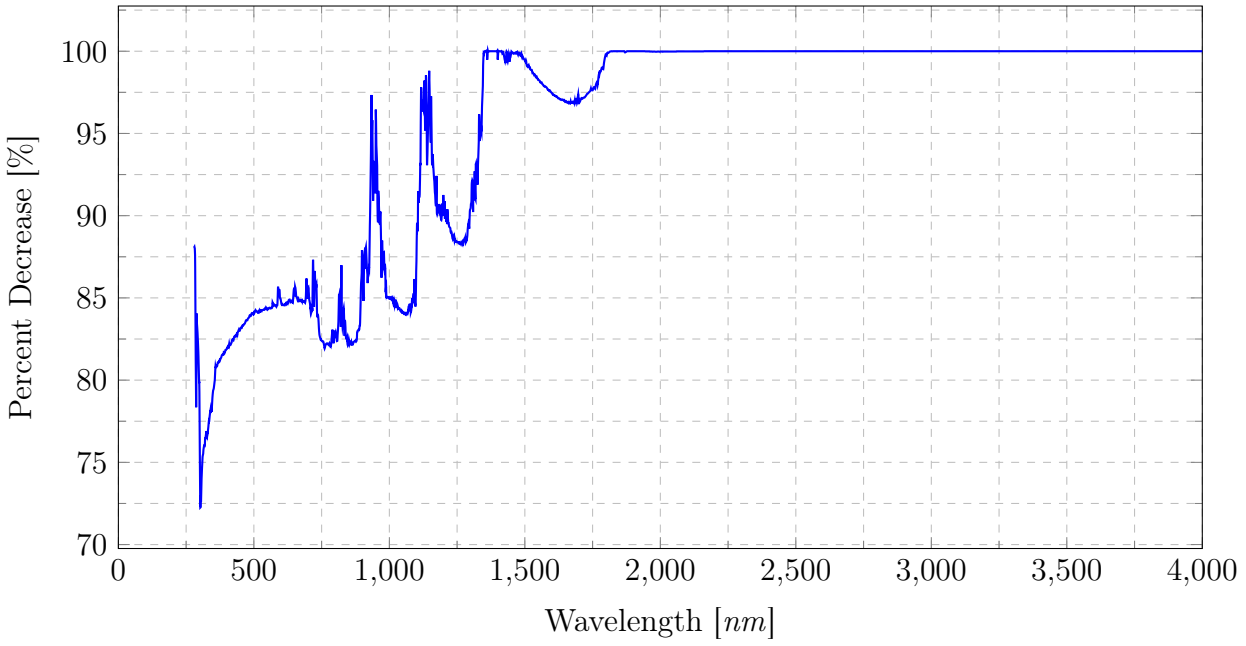

Figure 6.31: Percent Decrease in Spectral Irradiance from Clear to Overcast Conditions.

From Figure 6.32, it is seen that the relative power in the wavelengths from approximately 290 nm to 490 nm is significantly increased. However, the relative power is suppressed across most of the remaining wavelengths, as previously discussed.

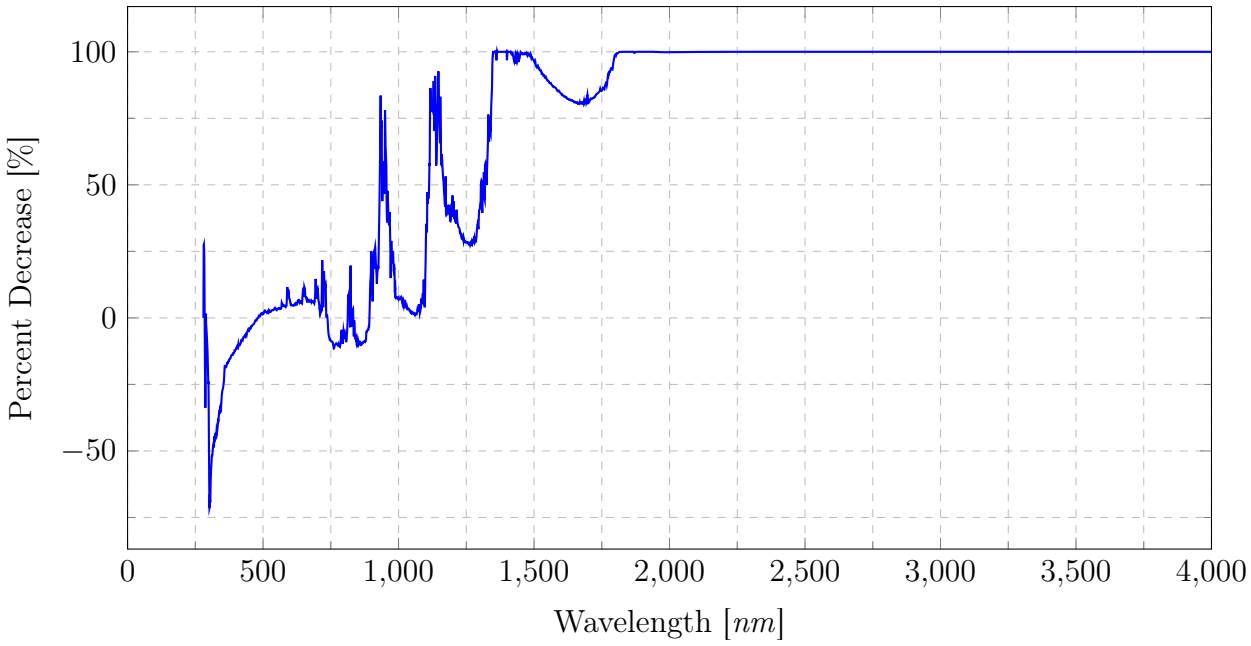

Figure 6.32: Percent Decrease in Normalised Spectral Irradiance from Clear to Overcast Conditions.

Panels made from different PV technologies achieve peak efficiencies at different wavelengths, as stated in Chapter 2.6.3. Under overcast conditions, it seems that PV technologies such as CdTe, which reach peak efficiency at approximately 800 nm, would be more beneficial than polycrystalline or monocrystalline silicon panels, which reach peak efficiency at 950 nm and 1030 nm respectively.

6.4 Chapter Review

The measurement station was evaluated and found to perform as intended. Testing showed that the station was able to track the sun accurately, even when it was misaligned.

The broadband irradiance measurements were compared with measurements made by an independent measurement station nearby. The results were shown to correlate very well, and it was concluded that these measurements are valid. Spectral irradiance measurements were made under similar conditions to the ASTM G173 reference spectra. These measurements were then compared with the reference spectra, and it was seen that they had a high correlation. This helped to validate the measurements.

The camera performed well during testing. Images corresponding to measurements were successfully captured. The only issue that was observed was that dew would form on the camera lens overnight in winter, which resulted in blurred images in the morning. However, the issue resolved itself within 30 minutes of normal operation. The pyrheliometer FOV was determined to account for 75 pixels of the 4800 pixel wide images captured by the camera.

Analysis of the captured data showed that the solar spectrum varies under many different conditions. The spectrum was seen to change due to variations in air mass at

different times of day, as well as during different seasons where the distance between the earth and the sun was varied. The spectrum was observed to be red-shifted in winter and blue-shifted in summer. The spectrum was also impacted by different cloud conditions. In general, it was observed that longer wavelengths are more significantly attenuated by clouds, and some shorter wavelengths are actually boosted under certain cloud conditions. The spectrum seems to be blue-shifted under overcast conditions in comparison to clear conditions.

Chapter 7

Conclusion and Recommendations

7.1 Conclusion

Short-term irradiance forecasting models are important tools used to manage energy fluctuations in PV power plants. However, these models only consider changes in broadband irradiance caused by clouds and do not consider the changes in spectral irradiance. Furthermore, existing software tools used in the PV industry also do not account for spectral variations under different atmospheric conditions. There is a lack of existing systems dedicated to data collection for the development of these models. This project aimed to design and build a measurement station to collect the data needed improve upon and develop irradiance forecasting models and PV software tools.

The measurement station is designed and built to meet the design objectives as outlined in Chapter 3.2 and the performance of the measurement station is evaluated in Chapter 6.

The station is shown to accurately track the movement of the sun, even in situations where the station is misaligned, by using the positional calibration algorithm. The broadband irradiance measurements made by the station are validated by comparison with measurements made by an independent measurement station in close proximity. The direct-circumsolar and global-tilted spectra are measured under similar conditions as the ASTM G-173 reference spectra. A comparison between the measured spectra and the reference spectra reveals a close correlation between them.

The attenuation of the solar spectrum under different cloud conditions is shown, and photographs captured by the onboard camera are used to identify the cloud conditions responsible for these changes. The variation in solar spectral irradiance during different times of day and during different seasons is also shown.

The measurement station is compact, solar-powered and relatively weather-resistant (it was only tested under mild weather conditions). This enables it to be deployed in remote locations to gather data. It is able to preform pre-programmed tasks automatically and interface with external devices for data transfer and communication purposes. It is customizable, and allows the measurement sequence and measurement frequency to be configured as required. The collected data can be stored for many days at a time, and additional storage can be easily added. This radiometric measurement station fulfils the

requirements and can successfully gather the data required by researchers to improve irradiance prediction models and PV software tools. The station has the potential to help optimize PV power stations as well as domestic PV installations.

7.2 Problems and Recommendations

Although the measurement station performed well overall, a few problems were identified during testing. Suggestions for some improvements to the station are listed below:

- The tilt range of the measurement station is currently limited from 0° to 80°. As a result, the station cannot capture data while the sun is close to the horizon during early mornings and late afternoons. A pan/tilt unit with a range of 0° to 90° would be a better choice.
- The pan/tilt unit had difficulty in lifting the current enclosure and instruments. This resulted in the implementation of a spring to reduce the resultant torque on the unit. A future version of the station could have an enclosure made of a lighter material to avoid this problem.
- An onboard GPS receiver could be implemented on the measurement station. This would remove the need for the configuration of the station for each location where it is deployed. It would also allow for more accurate time keeping.
- On cloudy or hazy days, the positional calibration algorithm could cause the instruments on the station to be pointed towards the brightest point in the sky, and not directly at the sun. This could be rectified by capturing a calibration cycle from sunrise to sunset on a clear day, and using that calibration cycle to correct for any positioning errors in software. This would also reduce measurement time, as positional calibration would not need to occur before each measurement.
- It was observed that dew would form on the camera lens during cold winter nights. A hydrophobic coating applied to the lens might prevent this from happening.

Appendices

Appendix A

Power Supply

A.1 5 V Supply

The list of component values used in the design of the 5 V supply, as labelled in the schematic presented below, is shown in Table A.1. The PCB layout is shown in Figure A.1.

Table A.1: Component Values Used.

Component Name	**Component Value**
C1a	1 mF
C1b	1 mF
C1c	1 mF
C2	4.7 μF
R1	220 kΩ
R2	22 kΩ
C4	10 nF
C5	1 μF
R3	62 kΩ
C6	100 nF
L1	4.7 μH
C7	10 pF
R4	100 kΩ
R5	1 MΩ
R6	191 kΩ
C8	47 μF
C9	47 μF
C10	47 μF
R7	190 Ω

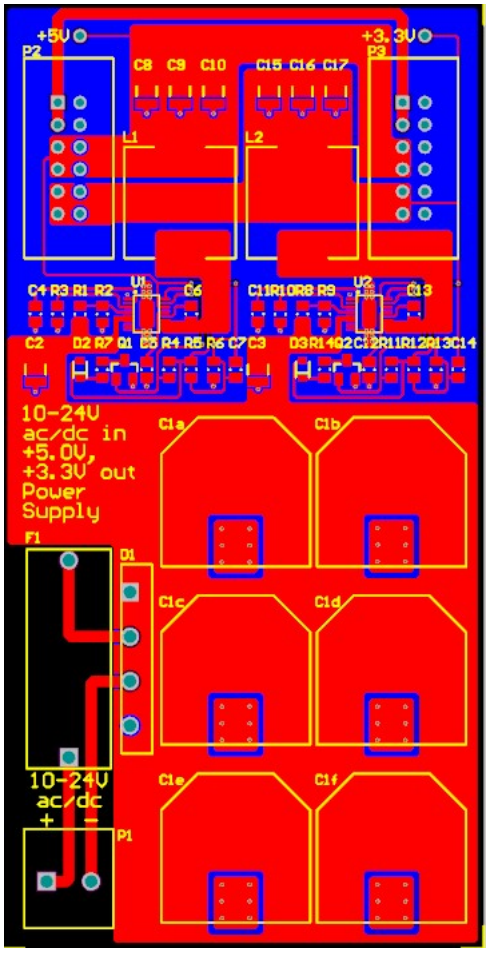

Figure A.1: PCB Layout of 5 V Supply.

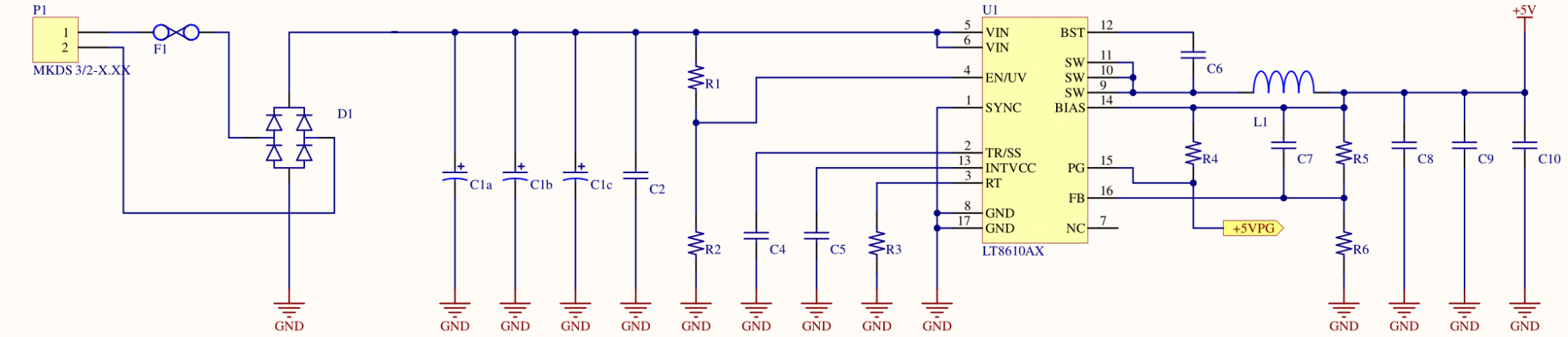

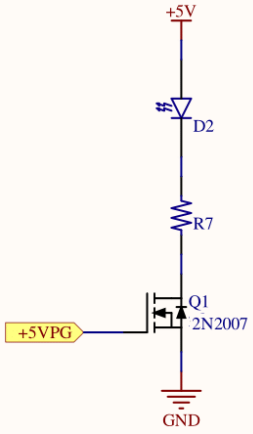

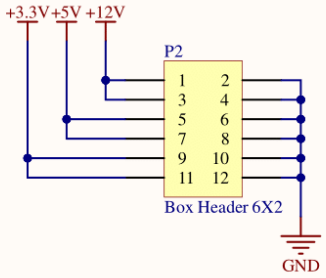

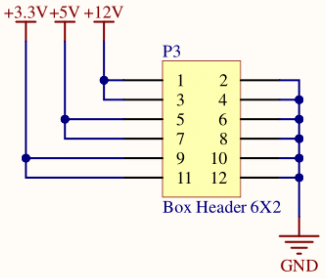

Title		
Size A4	Number	Revision
Date: 10/31/2021		Sheet of
File: Power supply.SchDoc		Drawn By:

A.2 12 V Supply

The list of the component values used in the design of the 12 V supply, as labelled in the schematic presented below, is shown in Table A.2. The PCB layout is shown in Figure A.2.

Table A.2: Component Values Used.

Component Name	**Component Value**
C1a	1 mF
C1b	1 mF
C1c	1 mF
C1d	1 mF
C1e	1 mF
C1f	1 mF
C2	10 μF
C3	10 μF
R1	1 MΩ
R2	120 kΩ
R3	22 kΩ
C4	4.7 μF
C5	100 nF
C6	100 nF
L1	4.7 μH
R4	39 kΩ
R5	1 MΩ
R6	91 kΩ
C7	820 pF
R7	10 kΩ
C8	33 pF
C9	4.7 μF
C10	4.7 μF
R8	3.9 kΩ
R9	1 kΩ
R10	220Ω

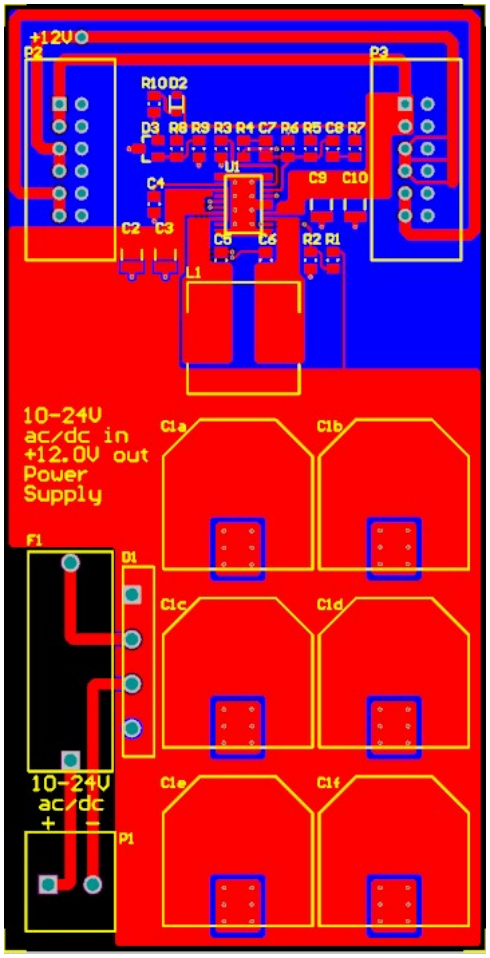

Figure A.2: PCB Layout of 12 V Supply.

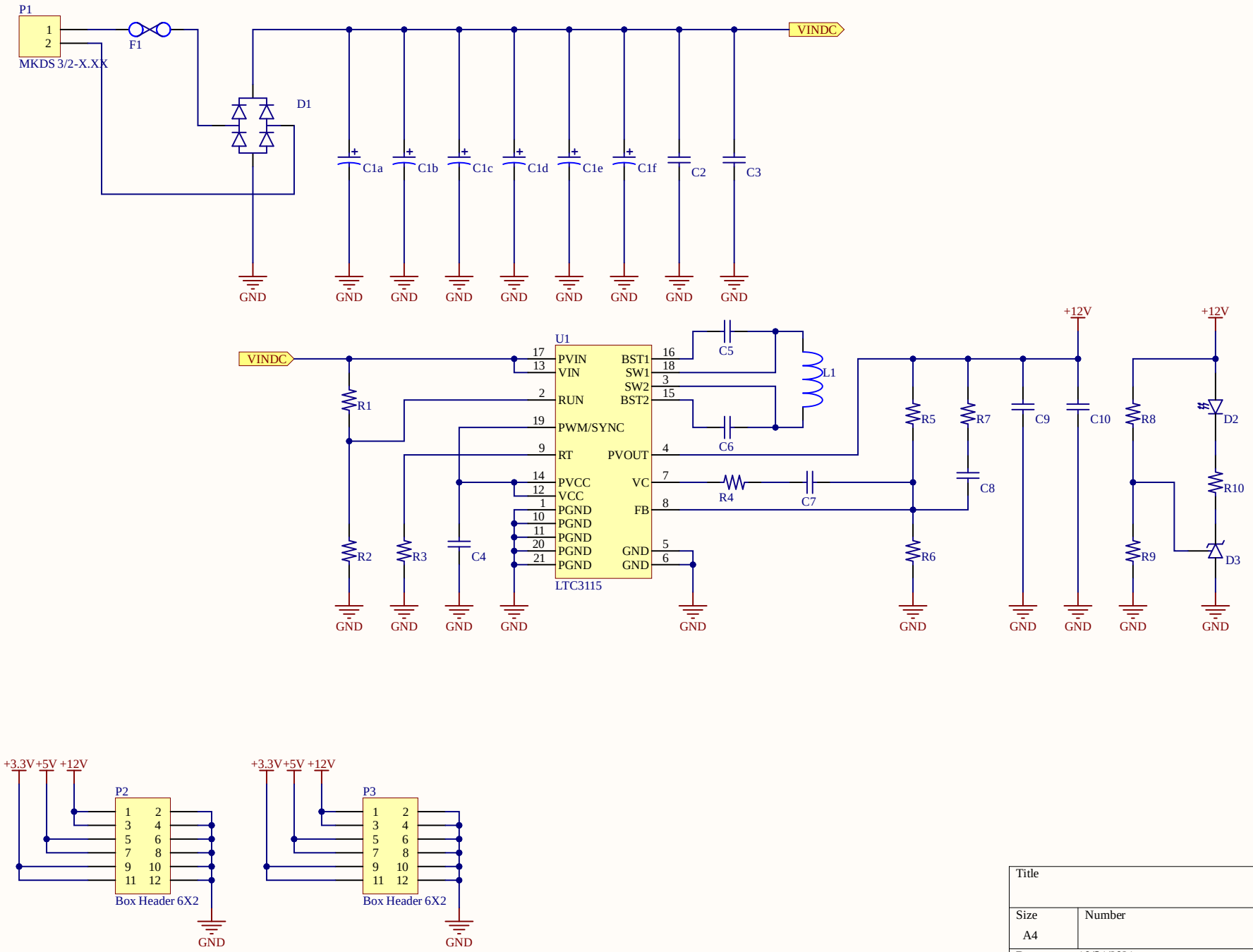

Title		
Size A4	Number	Revision
Date: 10/31/2021		Sheet of
File: Power supply.SchDoc		Drawn By:

Appendix B

Technical Drawings

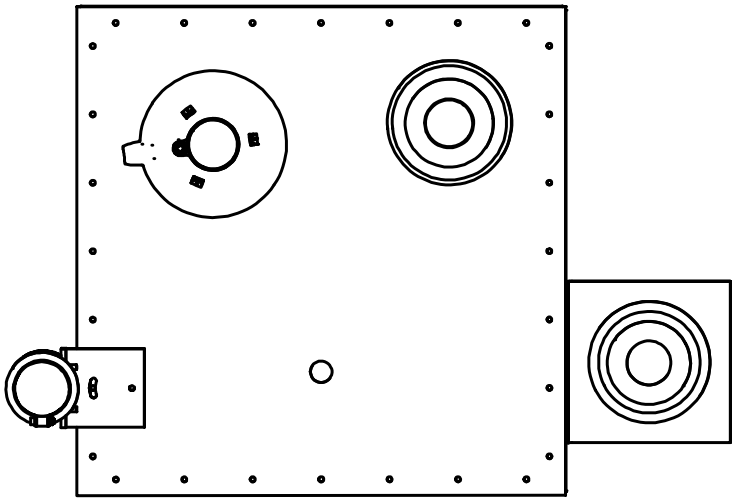

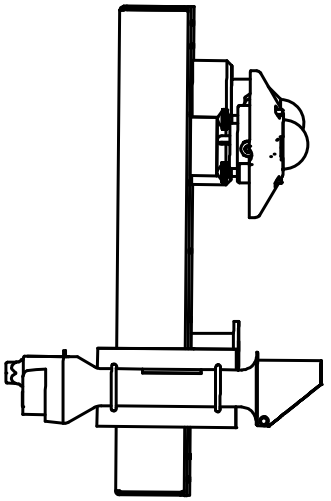

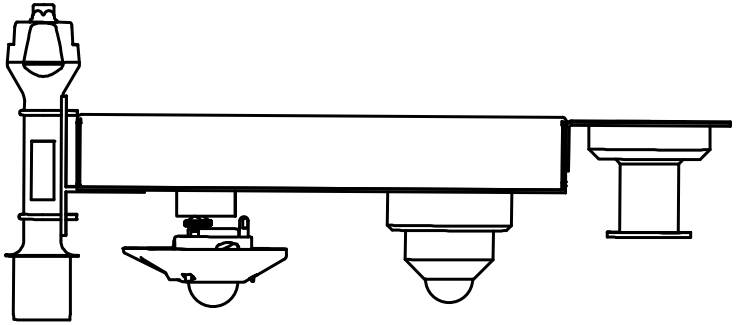

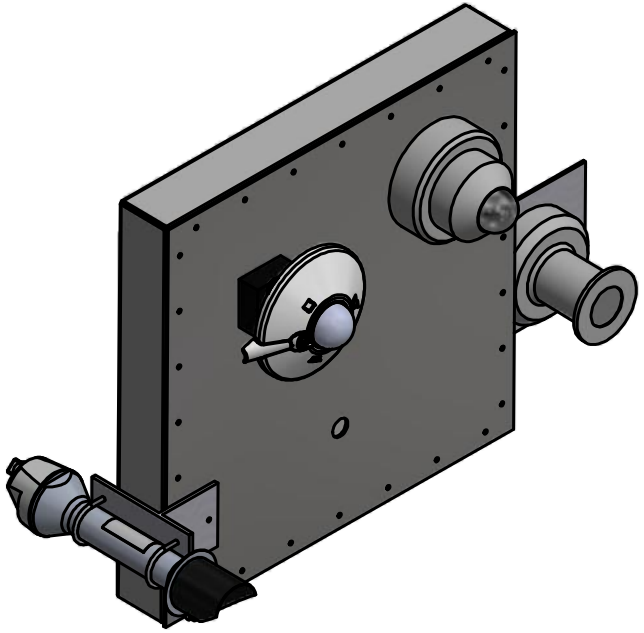

ITEM	BESKRYWING	AANTAL	MATERIAAL / SPESIFIKASIES

UNIVERSITEIT VAN STELLENBOSCH

SKAAL OP A

MATE IN mm

TITEL: Enclosure Assembly

STUDENTE No. 18496407	TEKENAAR M MELI	NAGESIEN	DATUM	VEL No. VAN VELLE	No.

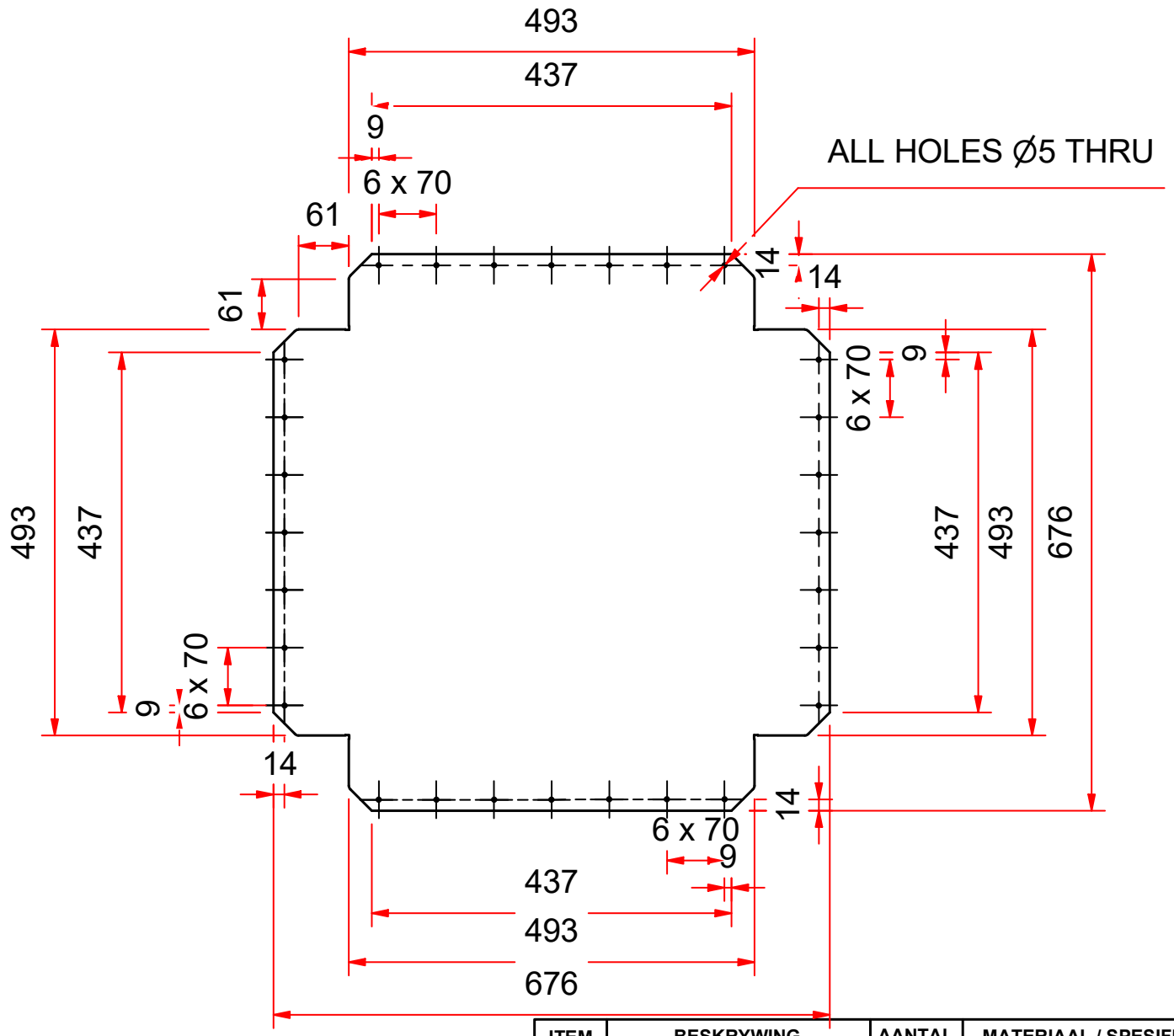

ITEM	BESKRYWING	AANTAL	MATERIAAL / SPESIFIKASIES 2 mm Aluminium

UNIVERSITEIT VAN STELLENBOSCH

SKAAL OP A4 = 1:8			TITEL: Enclosure Back - Unfolded		
MATE IN mm					
STUDENTE No. 18496407	TEKENAAR M MELI	NAGESIEN	DATUM	VEL No. VAN VELLE	No.

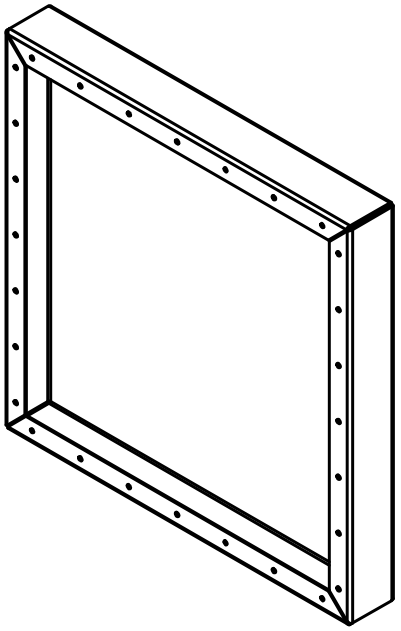

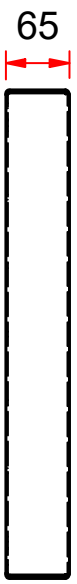

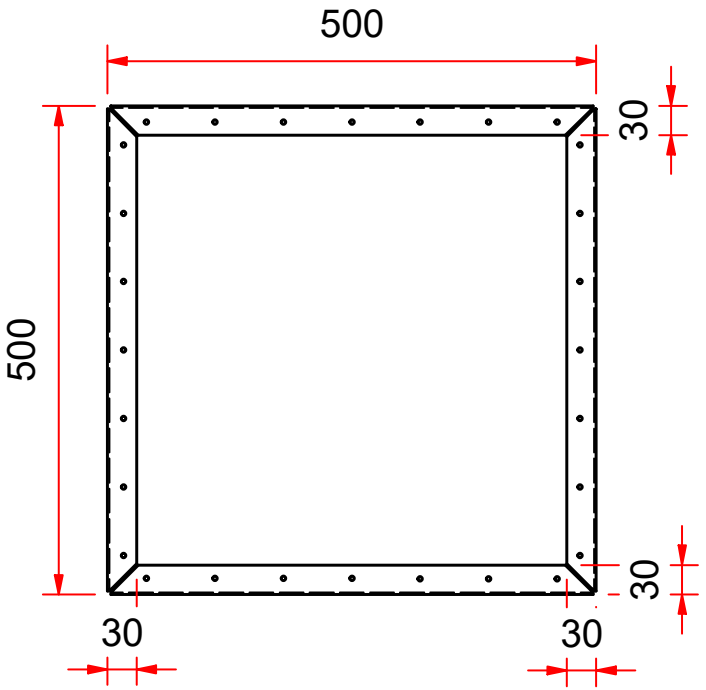

ITEM	BESKRYWING	AANTAL	MATERIAAL / SPESIFIKASIES 2 mm Aluminium

UNIVERSITEIT VAN STELLENBOSCH

SKAAL OP A4 = 1:8
MATE IN mm

TITEL: Enclosure Back - Folded

STUDENTE No. 18496407	TEKENAAR M MELI	NAGESIEN	DATUM	VEL No. VAN VELLE	No.

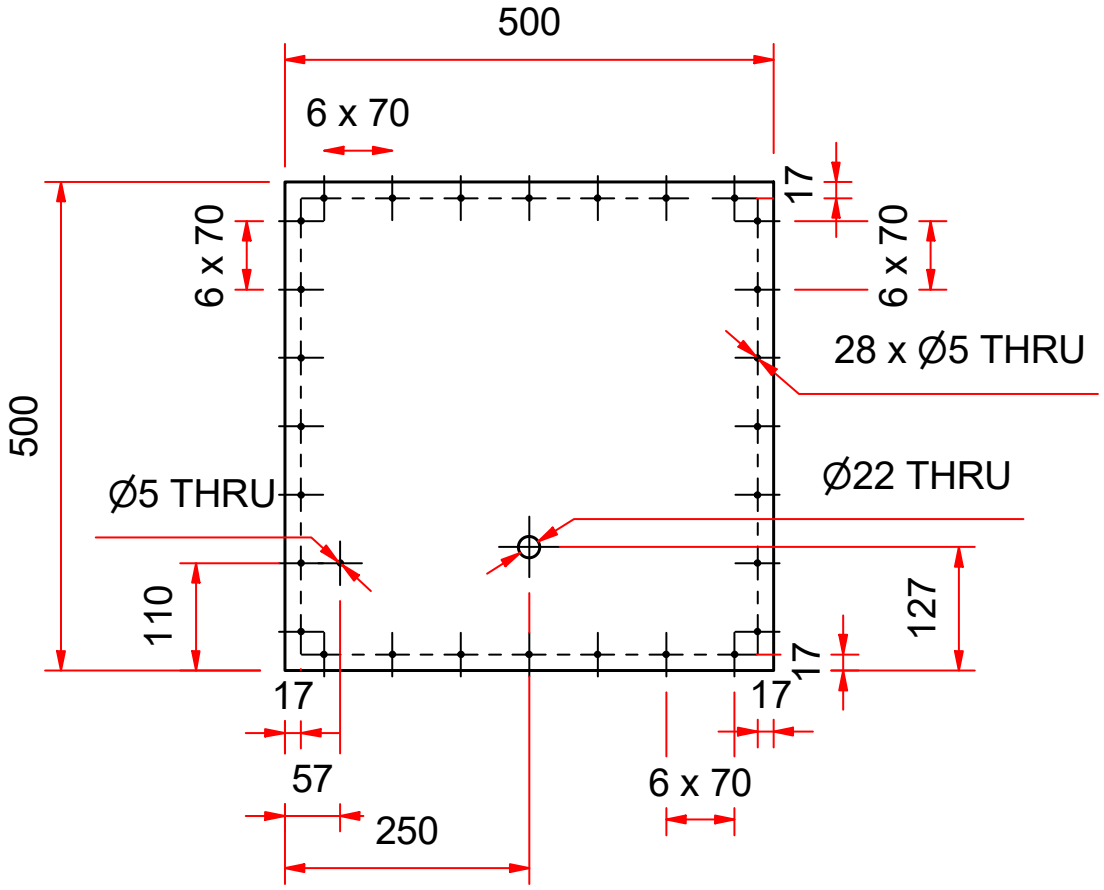

ITEM	BESKRYWING	AANTAL	MATERIAAL / SPESIFIKASIES 3 mm Aluminium

UNIVERSITEIT VAN STELLENBOSCH

STUDENTE No. 18496407	TEKENAAR M MELI	NAGESIEN	DATUM	VEL No. VAN VELLE No.

SKAAL OP A4 = 1:8
MATE IN mm
TITEL: Enclosure Front

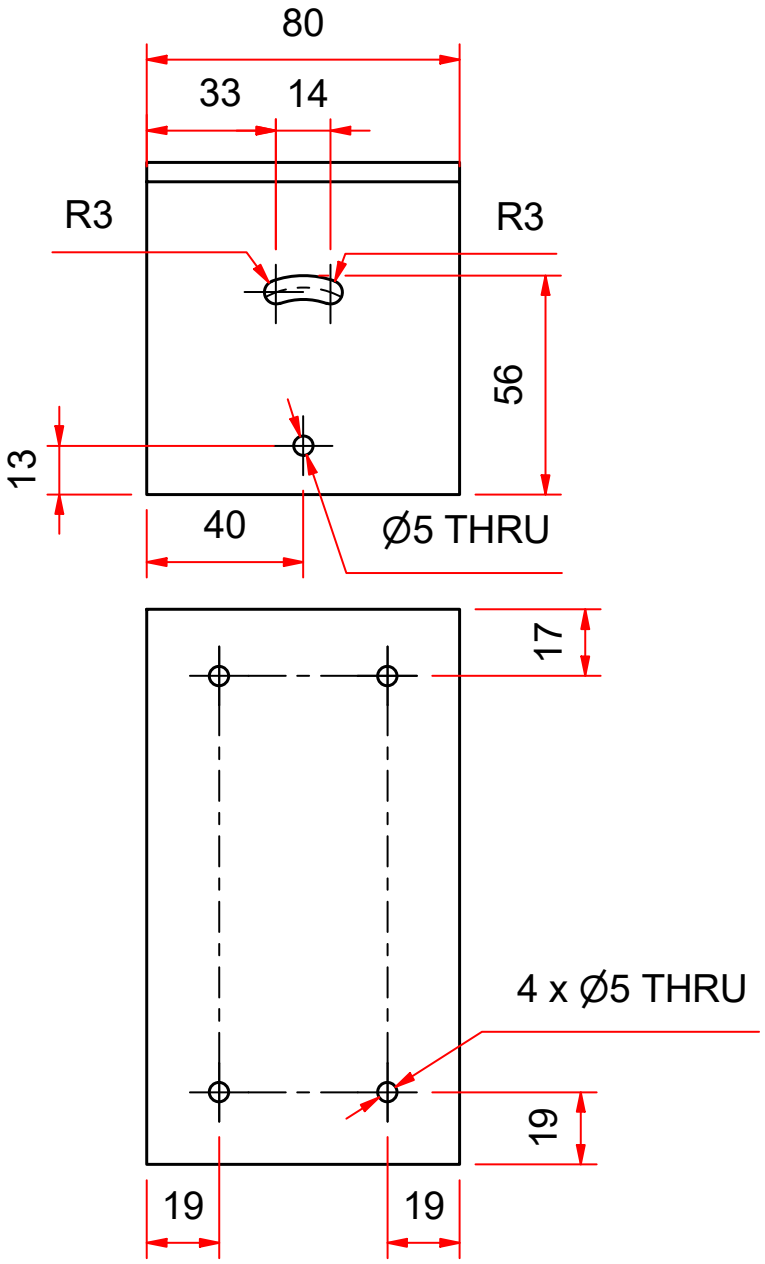

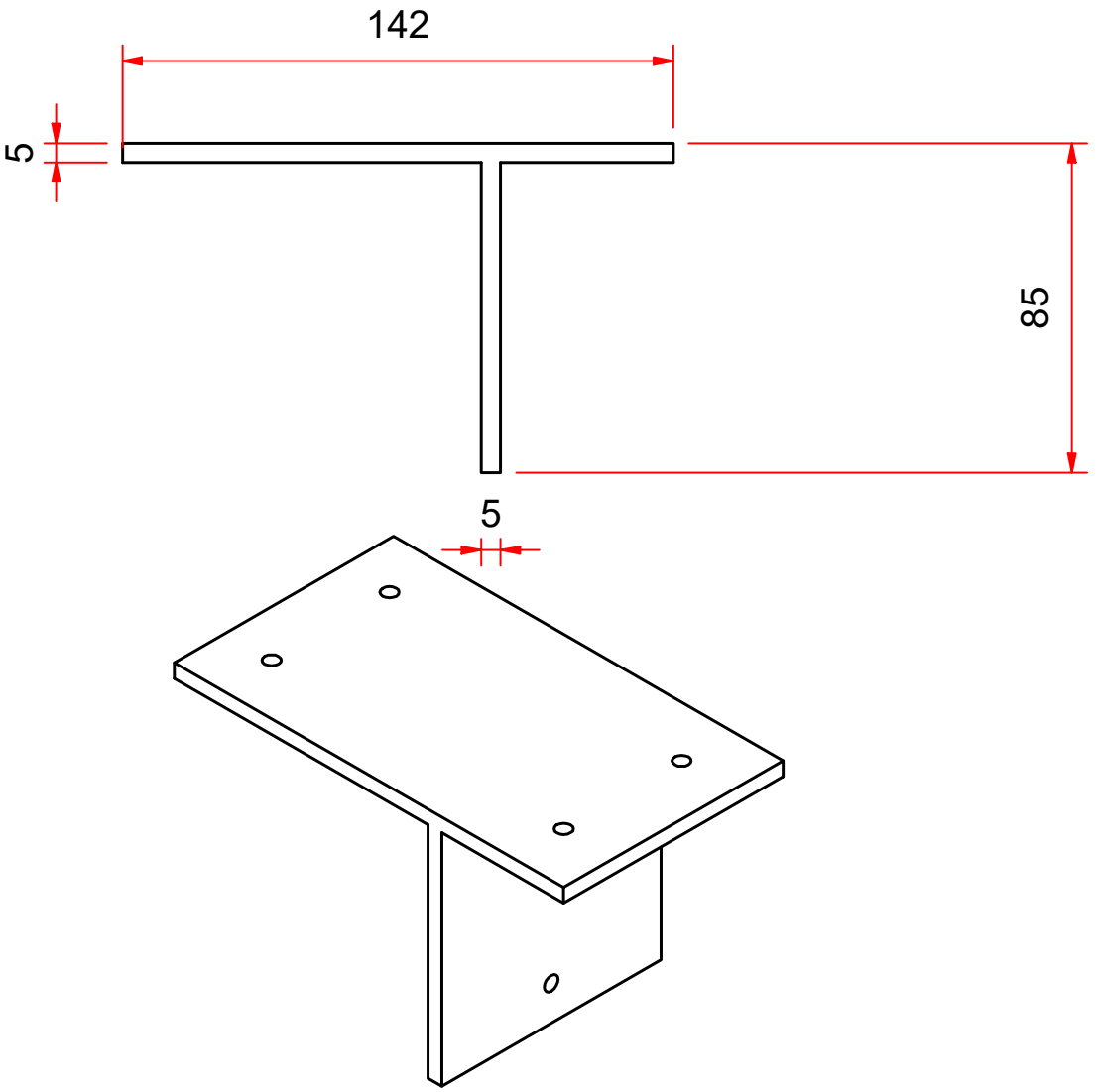

ITEM	BESKRYWING	AANTAL	MATERIAAL / SPESIFIKASIES 5 mm Aluminium

UNIVERSITEIT VAN STELLENBOSCH

SKAAL OP A4 = 1:2		TITEL: Pyrheliometer Mounting Bracket	
MATE IN mm			
STUDENTE No. 18496407	TEKENAAR M MELI	NAGESIEN	DATUM
VEL No.	VAN	VELLE	No.

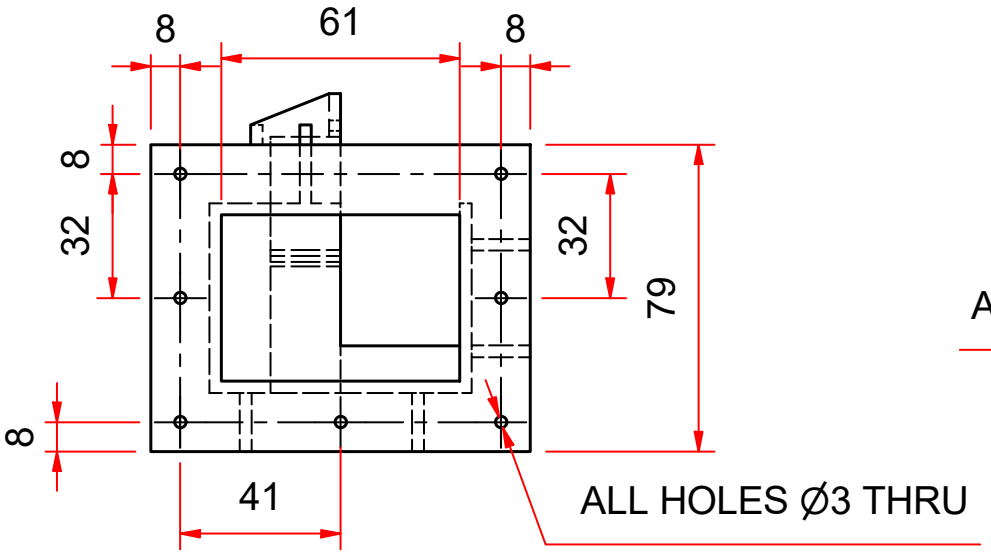

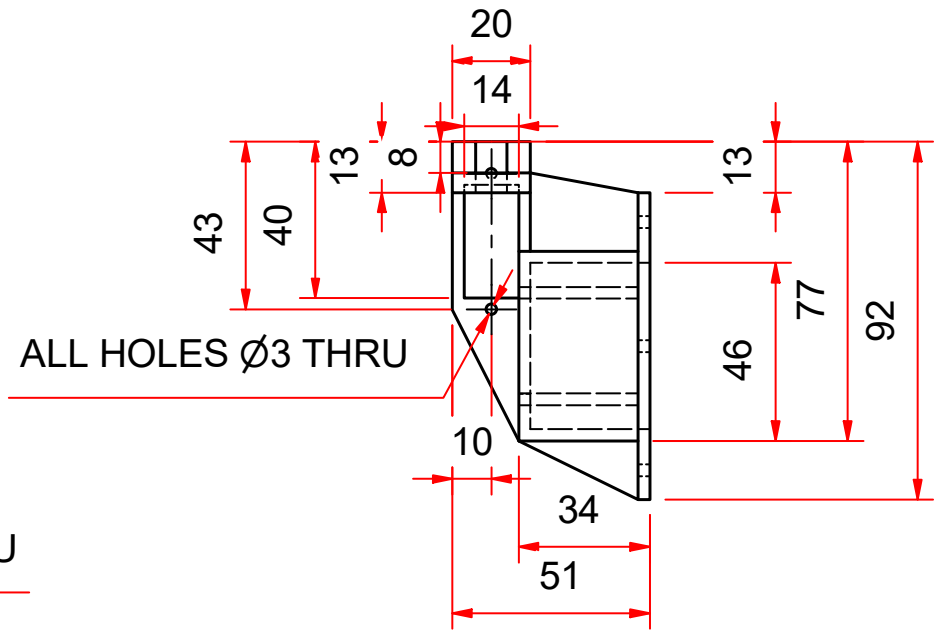

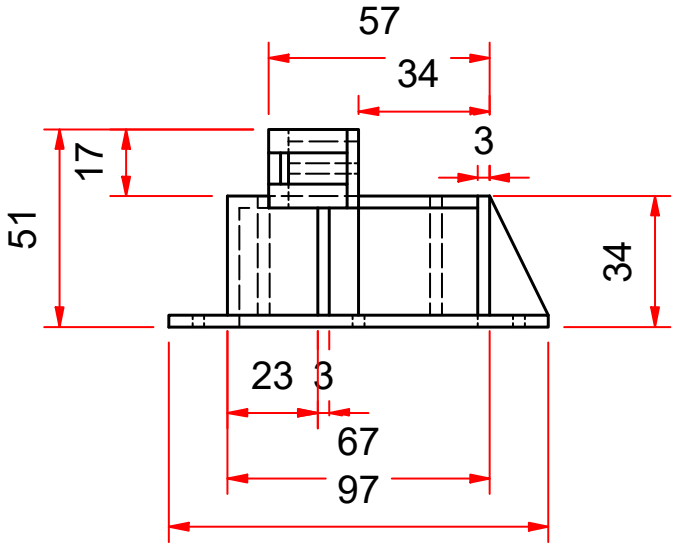

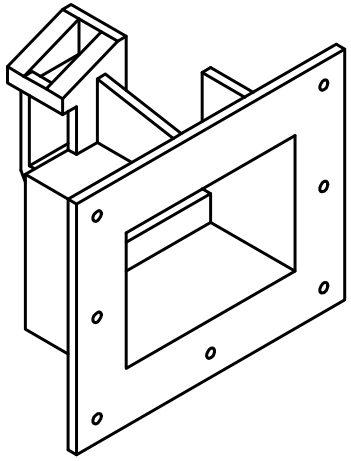

ITEM	BESKRYWING	AANTAL	MATERIAAL / SPESIFIKASIES 3 mm PLA

UNIVERSITEIT VAN STELLENBOSCH

SKAAL OP A4 = 1:2		TITEL: Camera Mounting Bracket	
MATE IN mm			
STUDENTE No. 18496407	TEKENAAR M MELI	NAGESIEN	DATUM
VEL No.	VAN	VELLE	No.

List of References

[1] United Nations Framework Convention on Climate Change. (2021) The paris agreement. [Online]. Available: https://unfccc.int/process-and-meetings/the-paris-agreement/the-paris-agreement

[2] UCSUSA. (2017) Benefits of renewable energy use. [Online]. Available: https://www.ucsusa.org/resources/benefits-renewable-energy-use

[3] Department of Energy | South Africa. solar-power. [Online]. Available: http://www.energy.gov.za/files/esources/renewables/r_solar.html

[4] Department of Mineral Resources and Energy | South Africa. (2019) Integrated resource plan (irp2019). [Online]. Available: http://www.energy.gov.za/IRP/2019/IRP-2019.pdf

[5] K. Passow and M. Lee, "Effect of spectral shift on solar pv performance," *2016 IEEE Conference on Technologies for Sustainability (SusTech)*, pp. 246–250, 2016.

[6] F. Giraud and Z. M. Salameh, "Analysis of the effects of a passing cloud on a grid-interactive photovoltaic system with battery storage using neural networks," *IEEE Transactions on Energy Conversion*, vol. 14, no. 4, pp. 1572–1577, 1999.

[7] G. Wang, M. Ciobotaru, and V. G. Agelidis, "Minimising output power fluctuation of large photovoltaic plant using vanadium redox battery storage," *6th IET International Conference on Power Electronics, Machines and Drives (PEMD 2012)*, pp. 1–6, 2012.

[8] G. M. Masters, *Renewable And Efficient Electric Power Systems, 2nd ed.* Hoboken, New Jersey: John Wiley & Sons, Inc., 2013.

[9] R. A. Messenger and J. Ventre, *Photovoltaic Systems Engineering, 3rd ed.* Boca Raton, Florida: CRC Press, Taylor & Francis Group, 2010.

[10] A. Reinders, P. Verlinden, W. van Sark, and A. Freundlich, *Photovoltaic solar energy : from fundamentals to applications.* Chichester, West Sussex, United Kingdom: John Wiley & Sons, Inc., 2017.

[11] The National Renewable Energy Laboratory. Reference air mass 1.5 spectra. [Online]. Available: https://www.nrel.gov/grid/solar-resource/spectra-am1.5.html

[12] H. Zirin. Solar constant. Encyclopedia Britannica. [Online]. Available: https://www.britannica.com/science/solar-constant

[13] C. B. Honsberg and S. G. Bowden. Air mass. [Online]. Available: https://www.pveducation.org/pvcdrom/properties-of-sunlight/air-mass

[14] Hukseflux. (2006) What is a pyrheliometer? [Online]. Available: https://www.hukseflux.com/uploads/inline/note-what_is_a_pyrheliometer_v2006.pdf

[15] ——. (2006) What is a pyranometer? [Online]. Available: https://www.hukseflux.com/uploads/inline/note-what_is_a_pyranometer_v2006.pdf

[16] Ossila Ltd. Spectrometer working principles, uses, and more. [Online]. Available: https://www.ossila.com/pages/spectrometer-application-notes

[17] V. Tatsiankou, K. Hinzer, J. Mohammed, A. Muron, M. Wilkins, J. Haysom, H. Schriemer, and S. Myrskog, "Reconstruction of solar spectral resource using limited spectral sampling for concentrating photovoltaic systems," in *Photonics North 2013*, vol. 8915, International Society for Optics and Photonics. SPIE, 2014, pp. 33–43.

[18] S. Pelland, J. Remund, J. Kleissl, T. Oozeki, and K. De Brabandere, *Photovoltaic and Solar Forecasting: State of the Art*. International Energy Agency Photovoltaic Power Systems Programme, 2013.

[19] X. Wang, P. Chen, L. Wen, B. Xiao, Z. Zhou, and H. Peng, "Prediction of direct normal irradiance using a novel multi-model algorithm," *2018 Chinese Automation Congress (CAC)*, pp. 2265–2269, 2018.

[20] S. Allan, D. Bryan, and B. Pouliot, "High-resolution numerical weather prediction (nwp) with data assimilation over placentia bay, newfoundland," *2014 Oceans - St. John's*, pp. 1–8, 2014.

[21] P. Mathiesen and J. Kleissl, "Evaluation of numerical weather prediction for intra-day solar forecasting in the continental united states," *Solar Energy*, vol. 85, no. 5, pp. 967–977, 2011.

[22] P. Mathiesen, C. Collier, and J. Kleissl, "A high-resolution, cloud-assimilating numerical weather prediction model for solar irradiance forecasting," *Solar Energy*, vol. 92, pp. 47–61, 2013.

[23] G. de Freitas Viscondi and S. Alves-Souza, "A systematic literature review on big data for solar photovoltaic electricity generation forecasting," *Sustainable Energy Technologies and Assessments*, vol. 31, pp. 54–63, 2019.

[24] M. Ozgoren, M. Bilgili, and B. Sahin, "Estimation of global solar radiation using ann over turkey," *Expert Systems with Applications*, vol. 39, no. 5, pp. 5043–5051, 2012.

[25] S. Theocharides, M. Kynigos, M. Theristis, G. Makrides, and G. E. Georghiou, "Intra-day solar irradiance forecasting based on artificial neural networks," *2019 IEEE 46th Photovoltaic Specialists Conference (PVSC)*, pp. 1628–1631, 2019.

[26] A. Rezrazi, S. Hanini, and M. Laidi, "An optimisation methodology of artificial neural network models for predicting solar radiation: a case study," *Theoretical and Applied Climatology*, vol. 123, 2015.

[27] S. Belaid and A. Mellit, "Prediction of daily and mean monthly global solar radiation using support vector machine in an arid climate," *Energy Conversion and Management*, vol. 118, pp. 105–118, 2016.

[28] L. W. Chong, R. W. Ng, Y. W. Wong, and R. K. Rajkumar, "One-hour ahead prediction of solar irradiance using support vector machines," *2018 International Electrical Engineering Congress (iEECON)*, pp. 1–4, 2018.

[29] W. VanDeventer, E. Jamei, G. S. Thirunavukkarasu, M. Seyedmahmoudian, T. K. Soon, B. Horan, S. Mekhilef, and A. Stojcevski, "Short-term pv power forecasting using hybrid gasvm technique," *Renewable Energy*, vol. 40, pp. 397–379, 2019.

[30] S. Cros, O. Liandrat, N. Sebastien, and N. Schmutz, "Extracting cloud motion vectors from satellite images for solar power forecasting," *International Geoscience and Remote Sensing Symposium (IGARSS)*, pp. 4123–4126, 2014.

[31] A. Hammer, D. Heinemann, E. Lorenz, and B. Luckehe, "Short-term forecasting of solar radiation: a statistical approach using satellite data," *Solar Energy*, vol. 67, no. 1–3, pp. 139–150, 1999.

[32] C. W. Chow, B. Urquhart, M. Lave, A. Dominguez, J. Kleissl, J. Shields, and B. Washom, "Intra-hour forecasting with a total sky imager at the uc san diego solar energy testbed," *Solar Energy*, vol. 85, no. 11, pp. 2881–2893, 2011.

[33] S. Dev, F. M. Savoy, Y. H. Lee, and S. Winkler, "Short-term prediction of localized cloud motion using ground-based sky imagers," *2016 IEEE Region 10 Conference (TENCON)*, pp. 2563–2566, 2016.

[34] S. Kapoor, A. K. Singh, S. vir Singh, and R. C. Upadhyay, *Recording of Meteorological Data and Physiological Parameters in Animals*, December 2013.

[35] C. N. Long, J. Sabburg, J. Calbo, and D. Pages, "Retrieving cloud characteristics from ground-based daytime color all-sky images," *Journal of Atmospheric and Oceanic Technology*, vol. 23, pp. 633–652, 2006.

[36] S. Dev, F. Savoy, Y. H. Lee, and S. Winkler, "Wahrsis: A low-cost high-resolution whole sky imager with near-infrared capabilities," *Proceedings of SPIE - The International Society for Optical Engineering*, vol. 9071, p. 90711L, 2014.

[37] A. Ryu, M. Ito, H. Ishii, and Y. Hayashi, "Preliminary analysis of short-term solar irradiance forecasting by using total-sky imager and convolutional neural network," *2019 IEEE PES GTD Grand International Conference and Exposition Asia (GTD Asia)*, pp. 627–631, 2019.

[38] M. Cervantes, H. Krishnaswami, W. Richardson, and R. Vega, "Utilization of low cost, sky-imaging technology for irradiance forecasting of distributed solar generation," *2016 IEEE Green Technologies Conference (GreenTech)*, pp. 142–146, 2016.

[39] S. R. Wenham, M. A. Green, M. E. Watt, R. P. Corkish, and A. B. Sproul, *Applied Photovoltaics, 3rd ed.* Milton Park, Abingdon: Earthscan from Routledge, 2012.

[40] Britannica, The Editors of Encyclopaedia. Photovoltaic effect. Encyclopedia Britannica. [Online]. Available: https://www.britannica.com/science/photovoltaic-effect

[41] Solar Energy Technologies Office. Solar photovoltaic cell basics. U.S. Department of Energy. [Online]. Available: https://www.energy.gov/eere/solar/solar-photovoltaic-cell-basics

[42] Coulee Energy. (2020) Standard test conditions of pv module. [Online]. Available: https://couleenergy.com/standard-test-conditions-of-pv-module/

[43] Center for Sustainable Systems, University of Michigan. (2021) Photovoltaic energy factsheet. [Online]. Available: https://css.umich.edu/factsheets/photovoltaic-energy-factsheet

[44] M. Schwieger and W. Hermann, "Characterizing the impact of solar spectral irradiance on pv module output," *2017 IEEE 44th Photovoltaic Specialist Conference (PVSC)*, pp. 1–3, 2017.

[45] M. Mikofski, A. Oumbe, C. Li, and B. Bourne, "Evaluation and correction of the impact of spectral variation of irradiance on pv performance," *2016 IEEE 43rd Photovoltaic Specialists Conference (PVSC)*, pp. 1357–1362, 2016.

[46] B. Marion, "Influence of atmospheric variations on photovoltaic performance and modeling their effects for days with clear skies," *2012 38th IEEE Photovoltaic Specialists Conference*, pp. 3402–3407, 2012.

[47] M. N. Islam, M. Z. Rahman, and S. M. Mominuzzaman, "The effect of irradiation on different parameters of monocrystalline photovoltaic solar cell," *2014 3rd International Conference on the Developments in Renewable Energy Technology (ICDRET)*, pp. 1–6, 2014.

[48] N. H. Zaini, M. Z. Ab Kadir, M. Izadi, N. I. Ahmad, M. A. M. Radzi, and N. Azis, "The effect of temperature on a mono-crystalline solar pv panel," *2015 IEEE Conference on Energy Conversion (CENCON)*, pp. 249–253, 2015.

[49] Kipp & Zonen, *Instruction Manual SHP1 Smart Pyrheliometer*, User Manual, February 2017. [Online]. Available: https://www.kippzonen.com/Download/596/Manual-Smart-Pyrheliometer-SHP1-English

[50] ——, *Instruction Manual SMP Series Smart Pyranometer*, User Manual, February 2017. [Online]. Available: https://www.kippzonen.com/Download/583/Manual-SMP-series-Smart-Pyranometers

[51] Spectrafy Inc. Solarsim-d2. [Online]. Available: https://www.spectrafy.com/products/solarsim-d2

[52] ——. Solarsim-g. [Online]. Available: https://www.spectrafy.com/products/solarsim-g

[53] GoPro Inc. Gopro hero7 black. [Online]. Available: https://gopro.com/en/us/shop/hero7-black/tech-specs?pid=CHDHX-701-master

[54] GoPro Support Hub. (2019) Sun reflection. [Online]. Available: https://community.gopro.com/t5/Cameras/Sun-reflection/td-p/377968

[55] Sony Middle East and Africa FZE. Dsc-rx0 specifications. [Online]. Available: https://www.sony-mea.com/en/electronics/support/compact-cameras-dsc-rx-series/dsc-rx0/specifications

[56] Crouzet, *Crouzet Miniature Electric Linear Actuator*, Datasheet. [Online]. Available: https://docs.rs-online.com/afb4/0900766b8053c02d.pdf

[57] Pololu, *Power HD Mini Servo*, Datasheet. [Online]. Available: https://www.pololu.com/file/0J318/HD-1160A.pdf

[58] Kipp & Zonen, *Instruction Manual SOLYS2 Sun Tracker*, User Manual, April 2017. [Online]. Available: https://www.kippzonen.com/Download/440/Manual-Sun-Tracker-SOLYS

[59] Cangzhou Haina Electronic Technology Co. Intelligence variable pan tilt mg-2022. [Online]. Available: https://www.alibaba.com/product-detail/Great-machine-Heavy-duty-22kg-pan_62150225425.html

[60] Raspberry Pi Foundation. Raspberry pi 3 model b+. [Online]. Available: https://static.raspberrypi.org/files/product-briefs/Raspberry-Pi-Model-Bplus-Product-Brief.pdf

[61] Maxim Integrated Products, Inc., Dallas Semiconductor Corporation, *DS1302 Trickle-Charge Timekeeping Chip*, Datasheet, 2004. [Online]. Available: https://www.waveshare.com/w/upload/0/0e/DS1302.pdf

[62] D-Link Corporation, *D-Link DSL-G225*, Datasheet. [Online]. Available: http://downloads.d-link.co.za/DSL/DSL-G225/Telkom/Datasheet/Datasheet%20G225.pdf

[63] Climatebiz. Average peak sun hours (south africa). [Online]. Available: https://climatebiz.com/average-peak-sun-hours-south-africa/

[64] Climate-Data.org. Climate stellenbosch (south africa). [Online]. Available: https://en.climate-data.org/africa/south-africa/western-cape/stellenbosch-6770/

[65] Rolls Battery Engineering. Temperature vs. capacity - flooded lead acid batteries. [Online]. Available: http://support.rollsbattery.com/en/support/solutions/articles/5860-temperature-vs-capacity-flooded-lead-acid-batteries

[66] Microcare Solar Components, *LCD MPPT User Documentation*, User Manual. [Online]. Available: http://gbsynergy.co.za/micro/wp-content/uploads/2014/10/LCD-MPPT-Charge-Controller-Manual.pdf

[67] Linear Technology Corporation, *LT8610 - 42V, 2.5A Synchronous Step-Down Regulator with 2.5 µA Quiescent Current*, Datasheet, 2012. [Online]. Available: https://www.analog.com/media/en/technical-documentation/data-sheets/8610fa.pdf

[68] ——, *LTC3115-1 - 40V, 2A Synchronous Buck-Boost DC/DC Converter*, Datasheet, 2019. [Online]. Available: https://www.analog.com/media/en/technical-documentation/data-sheets/LTC3115-1.pdf

[69] R. C. Hibbeler and K. B. Yap, *Mechanics for Engineers STATICS, 13th SI Edition*. 23/25 First Lok Yang Road, Jurong, Singapore: Pearson Education South Asia Pte Ltd, 2012.

[70] Modbus-IDA, *MODBUS over Serial Line Specification and Implementation Guide*, Specification and Implementation Guide, August 2006, v1.01. [Online]. Available: https://modbus.org/docs/Modbus_over_serial_line_V1_01.pdf

[71] Logic IO. Modbus commands. [Online]. Available: http://www.logicio.com/HTML/ioext-modbuscommands.htm

[72] E. Hamilton, *Pelco PTZ Protocols D Protocol*, Pelco, April 2008, v5.0.1.

[73] Spectrafy Inc., *User Manual: Solar Spectral Irradiance Meter SolarSIM-G*, User Manual, 2017. [Online]. Available: https://www.spectrafy.com/sites/default/files/2020-11/SolarSIM-G%20User%20Manual.pdf

[74] ——, *User Manual: Solar Spectral Irradiance Meter SolarSIM-D2*, User Manual, 2018. [Online]. Available: https://www.spectrafy.com/sites/default/files/2020-11/SolarSIM-D2%20User%20Manual.pdf

[75] J. J. Michalsky, "The astronomical almanac's algorithm for approximate solar position(1950-2050)," *Solar Energy*, vol. 40, no. 3, pp. 227–235, 1988.

[76] M. Blanco-Muriel, D. C. Alarcon-Padilla, T. Lopez-Moratalla, and M. Lara-Coira, "Computing the solar vector," *Solar Energy*, vol. 70, no. 5, pp. 431–441, 2001.

[77] I. Reda and A. Andreas, *Solar Position Algorithm for Solar Radiation Applications*, National Renewable Energy Laboratory, January 2008.

[78] M. J. Brooks, S. du Clou, J. L. van Niekerk, P. Gauche, C. Leonard, M. J. Mouzouris, A. J. Meyer, N. van der Westhuizen, E. E. van Dyk, and F. Vorster, "Sauran: A new resource for solar radiometric data in southern africa," *Journal of Energy in Southern Africa*, vol. 26, pp. 2–10, 2015.

[79] The Southern African Universities Radiometric Network (SAURAN). Southern african universities radiometric network solar radiometric data for the public. [Online]. Available: https://sauran.ac.za/